

---

# **Polarized Solid Ammonia Targets for the COMPASS Experiment at CERN**

---

von

ALEXANDER BERLIN

## **DISSERTATION**

zur

Erlangung des Grades eines Doktors  
der Naturwissenschaften in der Fakultät für  
Physik und Astronomie der Ruhr-Universität Bochum

INSTITUT FÜR EXPERIMENTALPHYSIK I  
PHYSIK DER HADRONEN UND KERNE

Bochum, September 2015

1. Gutachter: Prof. Dr. Werner Meyer
  2. Gutachter: PD Dr. Fritz-Herbert Heinsius
- (Lehrstuhl für experimentelle Hadronenphysik, Ruhr-Universität Bochum)

Tag der Disputation: 17.12.2015

# Abstract of the Dissertation

## Polarized Solid Ammonia Targets for the COMPASS Experiment at CERN

by

**Alexander Berlin**

Institute of Experimental Physics I / Physics of Hadrons and Nuclei

Faculty of Physics and Astronomy

Ruhr-University of Bochum, 2015

This thesis focuses on ammonia ( $\text{NH}_3$ ) as a target material – from the production process to the application in the international large-scale experiment COMPASS and beyond. Besides the production of the target material, the aim of this study is to find out, how a long-term storage at nitrogen temperatures influences the polarization properties. Furthermore, a new target cell is constructed, which should meet the requirements of a higher radiation exposure during the Drell-Yan measurements at COMPASS in 2015. In addition, the response of the temperature sensors to high radiation doses should be investigated, since they are in close vicinity to the particle beam of the experiment.

This thesis leads also briefly into the basic subjects of the 'polarized target' and gives an historical overview of the COMPASS experiment and its predecessors, as well as the development of ammonia as a polarizable target material.

The results support the observation, that the radical, which is used during the dynamic nuclear polarization, is quite stable during storage at 77 K, whereas other radicals may not survive. Within the 4 years after the irradiation, a major change in the polarization-properties of ammonia could not be observed. Only in the first year, a trend to longer build-up and relaxation times is visible.

The new target cell was finished in time for the Drell-Yan measurements and is completely made of chlorofluoropolymer (PCTFE), which has a high radiation resistance and is free of hydrogen (no background signal). The cells are designed in a modular system, which allows an easy replacement of defect sections and a high adaptability. Features like the filling-holes and distance-pieces could be directly integrated into the cell body.

Two sensor types for the temperatures were tested, up to a radiation dose of 20 kGy. As a result, the silicon diodes show a cumulative deviation at higher doses, which disqualifies them for an exact temperature measurement, whereas the ruthenium-oxide resistors had changed not at all.

## Acknowledgment/Danksagung

An dieser Stelle möchte ich mich bei Prof. Dr. Werner Meyer für die Ermöglichung dieser Arbeit bedanken, und für sein Verständnis, besonders in den letzten Zügen meiner Promotion. Weiterhin danke ich PD Dr. Fritz-Herbert Heinsius, der freundlicherweise das Zweitgutachten übernommen hat.

Besonders danke ich der gesamten Bochumer Target-Crew, für ihre Unterstützung während meiner gesamten Zeit am Lehrstuhl. Dr. Gerhard Reicherz und Jonas Herick, für ihre stete und uneingeschränkte Hilfsbereitschaft, bei allem was mit dem Target und der Uni zu tun hatte, sowie Dr. Christian Heß, der mir den Laboralltag näher gebracht hat.

Danke an das Sekretariat für die Übernahme sämtlicher bürokratischer Aufgaben, ohne die man sich nicht auf seine Arbeit hätte konzentrieren können. Auch vielen Dank an Mario Fink, der immer sehr hilfsbereit war wenn es um elektronische Angelegenheiten ging.

Danke an die Feinmechanik-Werkstatt, unter der Leitung von Holger Zemzycki, für ihre Unterstützung, nicht nur bei der Fertigung der Targetzelle.

Danke auch an die intensive Kollaboration mit Bonn, ohne die diese Arbeit nicht möglich gewesen wäre, insbesondere an Stefan Runkel und Scott Reeve.

I would also like to thank the COMPASS target group, for their support during my time at CERN and their assistance with the experimental results.

Einen ganz lieben Dank an Johanna, die mir Lebensfreude und das Gefühl gegeben hat, gebraucht zu werden. Viele glückliche Momente habe ich mit dir erlebt und ich hoffe, dass unsere Freundschaft noch lange bestehen bleibt.

Philipp, der mich durch das Studium begleitet hat und auch neben der Uni immer mal Zeit hatte etwas zu unternehmen. Vielen Dank für das Korrekturlesen.

Neben der Uni habe ich viel Unterstützung durch die Spielegruppe erfahren, im Besonderen dabei von Giny und Christina. Vielen Dank, dass ich mit euch befreundet sein darf.

Natürlich darf meine Familie nicht fehlen, die immer hinter meinen Entscheidungen bezüglich der Ausbildung gestanden und mich darin bestärkt haben. Danke!



# Contents

<b>1</b>	<b>Introduction</b>	<b>1</b>
<b>2</b>	<b>Concepts of Particle Magnetism</b>	<b>5</b>
2.1	Basic Principles . . . . .	5
2.1.1	The Idea of an Intrinsic Angular Momentum . . . . .	6
2.1.2	Interaction with Magnetic Fields . . . . .	7
2.2	Polarization . . . . .	9
2.2.1	Polarization at Thermal Equilibrium . . . . .	10
2.2.2	Dynamic Nuclear Polarization (DNP) . . . . .	11
2.3	Detection of Particle Magnetism . . . . .	17
2.3.1	Nuclear Magnetic Resonance (NMR) . . . . .	17
2.3.2	Electronic Paramagnetic Resonance (EPR) . . . . .	23
<b>3</b>	<b>Ammonia as a Polarizable Target Material</b>	<b>27</b>
3.1	Ammonia – a Portrait . . . . .	27
3.2	Ammonia Target – Pro vs. Contra . . . . .	29
3.3	Production of an Ammonia Target . . . . .	33
3.3.1	Preparation of Solid Ammonia . . . . .	33
3.3.2	DNP-Activation of Ammonia . . . . .	35
3.4	Radiation Hardness of Ammonia Targets . . . . .	40
<b>4</b>	<b>The COMPASS Experiment</b>	<b>43</b>
4.1	Intention of COMPASS . . . . .	43
4.2	COMPASS Target System . . . . .	44
4.3	Future of COMPASS – COMPASS II . . . . .	47
4.3.1	Drell-Yan Measurement . . . . .	48
4.3.2	Changes at COMPASS II . . . . .	49
4.4	Radiation Exposure during Drell-Yan . . . . .	51
<b>5</b>	<b>Behavior Studies of the Ammonia Target</b>	<b>55</b>
5.1	Paramagnetic Centers . . . . .	55
5.2	Polarization Measurements in Bochum . . . . .	59
5.2.1	Polarization and Relaxation Behavior . . . . .	60
5.2.2	Long-Term Behavior . . . . .	64
5.3	Polarization Measurements at COMPASS . . . . .	66
5.3.1	Shift of the Optimal Microwave Frequencies . . . . .	69

<b>6</b>	<b>PCTFE Target Cells for Drell-Yan</b>	<b>73</b>
6.1	Material Studies . . . . .	73
6.1.1	Test Irradiations . . . . .	74
6.1.2	Hydrogen Content . . . . .	76
6.1.3	Thermal Shrinkage of PCTFE . . . . .	78
6.2	Design of the PCTFE Target Cell . . . . .	79
6.2.1	Specifications . . . . .	79
6.2.2	Final Assembly . . . . .	83
<b>7</b>	<b>Radiation Hardness of the Temperature Sensors</b>	<b>85</b>
7.1	Temperature Sensors . . . . .	85
7.1.1	Setup . . . . .	86
7.1.2	Read-Out System . . . . .	86
7.2	Irradiation of the Sensors . . . . .	88
7.3	Comparison of the Sensors . . . . .	89
7.3.1	Construction of the Temperature Curves . . . . .	90
7.3.2	Behavior of the Resistors . . . . .	90
7.3.3	Behavior of the Diodes . . . . .	92
<b>8</b>	<b>Conclusion</b>	<b>95</b>
<b>Appendices</b>		
<b>A</b>	<b>Ammonia Behavior Studies</b>	<b>101</b>
<b>B</b>	<b>Target Cell</b>	<b>107</b>
<b>C</b>	<b>Temperature Sensors</b>	<b>119</b>
<b>Bibliography</b>		<b>123</b>
<b>List of Figures</b>		<b>127</b>

## List of Frequently Used Acronyms

<b>ADC</b>	Analog-to-Digital Converter
<b>CERN</b>	Conseil Européen pour la Recherche Nucléaire
<b>COMPASS</b>	Common Muon and Proton Apparatus for Structure and Spectroscopy
<b>cw</b>	Continuous Wave
<b>DNP</b>	Dynamic Nuclear Polarization
<b>DPPH</b>	2,2-Diphenyl-1-Picrylhydrazyl
<b>DSSE</b>	Differential Solid-State Effect
<b>DY</b>	Drell-Yan
<b>ELSA</b>	Elektronen-Stretcher-Anlage
<b>EMC</b>	European Muon Collaboration
<b>EPR</b>	Electronic Paramagnetic Resonance
<b>EST</b>	Equal-Spin-Temperature Theory
<b>F-center</b>	Color Center (Farbzentrum)
<b>FEP</b>	Fluorinated Ethylene Propylene
<b>FOM</b>	Figure of Merit
<b>LINAC</b>	Linear Accelerator
<b>NMR</b>	Nuclear Magnetic Resonance
<b>SLAC</b>	Stanford Linear Accelerator Center
<b>PCTFE</b>	Polychlorotrifluoroethene
<b>SIDIS</b>	Semi-Inclusive Deep Inelastic Scattering
<b>SMC</b>	Spin Muon Collaboration
<b>SPS</b>	Super Proton Synchrotron
<b>SSE</b>	Solid-State Effect
<b>TE</b>	Thermal Equilibrium
<b>TEMPO</b>	2,2,6,6-Tetramethylpiperidinyloxy
<b>THMP</b>	Temperature and Humidity Monitoring Board for PANDA



# Introduction

Since many centuries, the humankind is possessed to find answers to the questions about the origin of life and the structure of matter.

“That I may understand whatever  
Binds the worlds innermost core together.”

J.W. Goethe, Faust I, line 382f

It was this curiosity, which led to the four elements of nature and the chemical elements to the understanding, that matter is composed of only a few different fundamental and indivisible particles.

Early in history, the idea came up that matter is made out of smaller units, which cannot be further divided. These units were called *atoms* – the Greek word for indivisible. In fact, this approach was necessary from a theoretical and philosophical point of view, but not supported by any experiments. And it was not until the mid-17th century, that experiments gave first hints on such a structure. J. DALTON (\*1766; †1844) used the concept of atoms, to explain the fact, that chemical elements always react in integer ratios. This time was also the begin of the great success of the periodic table of chemical elements. More and more elements were found and even some predicted elements could be approved.

Gradually the idea came up, that atoms cannot be the smallest units and some other, more basic elements or particles must exist. Experiments of J.J. THOMSON (\*1856; †1940) with *electrons* in 1897 and the discovery of the radioactivity by H. BECQUEREL (\*1852; †1908) in 1896, led to an extended view of the structure of matter. Therefore, this time can be seen as the start of modern particle physics.

In 1911, E. RUTHERFORD (\*1871; †1937) proofed the existence of an atom substructure, with a positive charged nucleus (*protons*) and a negative charged cloud (electrons) [1]. In 1932, the *neutron* was discovered by J. CHADWICK (\*1920; †1998), a particle with no net electrical charge, which is essential to keep the positively charged nucleus together, through the nuclear strong force. Later in the 1960s, a substructure of these nuclear particles was predicted and proofed in the same decade through experiments at the SLAC<sup>1</sup> [2]. These substructure-particles are called *quarks* and count as fundamental particles, besides the electrons, muons and taus. A total number of six quarks are known and grouped into three families, see Fig. 1.1. The quarks are affected by the *strong interaction*, transmitted through the so-called *gluons*. *Hadrons* are particles, which are composed of quarks and

<sup>1</sup>Stanford Linear Accelerator Center, Menlo Park, California.

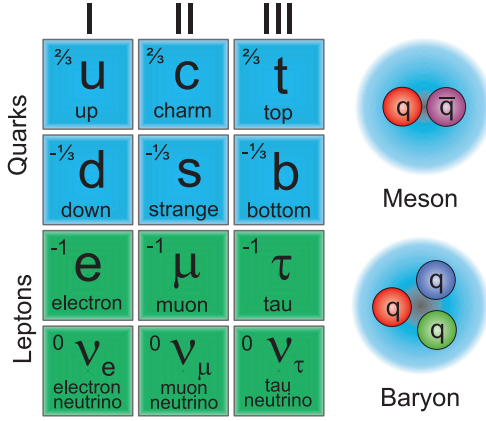


**Fig. 1.1** – Overview of quarks and leptons – each a fermion and thus, a spin-1/2 particle. The number in the upper left indicates the electrical charge. Hadrons are made-up particles of quarks and classified into mesons and baryons.

can be divided in two groups, *mesons* and *baryons*. Mesons are made of a quark/anti-quark pair, whereas baryons consists of either three quarks or anti-quarks. These two groups of particles can be distinguished by another characteristic, called the *spin*. The spin is an intrinsic property of particles, which follows the mathematics of the angular momentum. Mesons have an integer spin and thus, they are *bosons*, whereas baryons have a half-integer spin, making them *fermions*. At first, it seems to be clear, in which way the nuclear spin is composed of. Quarks are fermions and carry a spin of 1/2 and therefore, a simple combination of two or three quarks results either in an integer

or half-integer spin. For a particle like the proton, the spin can be naive expressed by

$$\frac{1}{2} = \frac{1}{2} \sum_q \Delta q \quad .$$

But in the late 1980s, scattering experiments at CERN<sup>2</sup> and SLAC reveal a total different situation. These measurements assumed, that the quarks contribute only about 30 % to the nuclear spin, at most. Figure 1.2 illustrates the situation artistically. An approach by R.L. JAFFE and A. MANOHAR includes the fraction of the gluons and the angular momentum of each component.

$$\frac{1}{2} = \frac{1}{2} \sum_q \Delta q + \sum_q L^q + \Delta G + L^g \quad (1.1)$$

For these measurements, special polarizable targets are necessary, in which most of the nuclear spins are orientated in the same 'direction'. The observable is the asymmetry  $A$ , which characterizes the variation in the count-rate for different target setups.

$$A = \frac{N_\downarrow - N_\uparrow}{N_\downarrow + N_\uparrow} \quad (1.2)$$

From the analysis, several spin-dependent parameters (form factors, structure functions) for different experimental setups are derived and then compared to theoretical models.

The development of such polarized targets is the main task of the Bochum polarized target group of Prof. W. MEYER. In this field, the appropriate choice of the target material depends on the experimental conditions. Nevertheless, there are certain parameters, which decide whether the material is a suitable polarized target or not. To reach a reasonable statistic in a double polarization experiment, the running time  $T$  is proportional to the following term

$$T \propto \frac{1}{P_B^2 P_T^2 f^2 \rho I \kappa (\Delta A)^2} \quad . \quad (1.3)$$

<sup>2</sup>Conseil Européen pour la Recherche Nucléaire, Geneve, Switzerland.

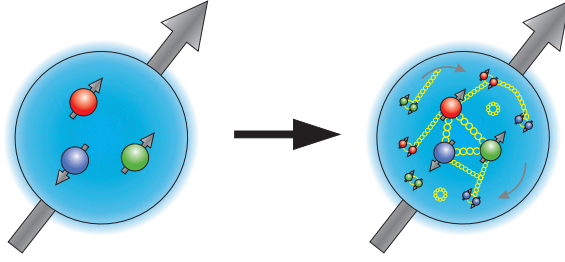


**Fig. 1.2** — Artistic illustration of the nuclear spin-decomposition. The left-hand side shows the concept of a full quark-content contribution, whereas the right-hand side gives a more complex outlook with contributions of gluons, orbital angular momenta and sea-quarks.

$f$  is the dilution factor, the fraction of polarizable nuclei in the material,  $P_T(P_B)$  the maximum target (beam) polarization,  $\rho$  the material density,  $\kappa$  the filling-factor,  $I$  the beam intensity and  $\Delta A$  represents the absolute error in the measured asymmetry. Concerning the target optimization, the dilution factor and the target polarization are the parameters with the largest influence. The dilution factor is fixed through the material, but the polarization degree is a parameter, which can be enhanced as an interplay of several techniques in the target business. Therefore, a high target polarization and dilution factor reduce the necessary time to achieve a chosen accuracy in the experiment. The target relating parameters are combined in the so-called *figure of merit*, which will be recalled in chapter 3, when ammonia is discussed as a polarized target material.

## Motivation and Outline

The motivation for this thesis arose from the request of a new fresh ammonia target for the COMPASS<sup>3</sup> experiment and the proposal of the Drell-Yan measurements, which is realized in the second stage of COMPASS, namely COMPASS II. Thereby, the focus lies on the application and development of ammonia as a polarizable target material and the changes in the target setup of COMPASS.

After the basic principles in chapter 2, a characterization of ammonia as a target material follows in chapter 3, in which the production and preparation, as well as an overview of the historical use of ammonia targets is given. Chapter 4 deals with the COMPASS experiment and its role in revealing the composition of the nuclear spin. This is followed by the prospects of COMPASS II and its consequences for the polarized target. In chapter 5, the relaxation behavior of ammonia over about 4 years is presented, as well as a comparison of the COMPASS results of 2007, 2010 and 2011. The next two chapters 6 and 7 are handling with more technical issues, such as the new design of the target cell for the Drell-Yan measurement and the radiation hardness of temperature sensors, which are located close to the particle beam of the experiment in the COMPASS refrigerator.

Since the 1980s, ammonia has evolved to a standard material in the target business and thus, several papers and theses are already published, dealing with this matter and this work should also be an attempt to combine those information with the measurements of the new produced ammonia of 2011.

<sup>3</sup>Common Muon and Proton Apparatus for Structure and Spectroscopy, a fixed-target particle physics experiment at CERN.





## Concepts of Particle Magnetism

To achieve the best possible polarization in a target, the properties of the particles must be known very well. These information are necessary to understand the behavior of the particle system and to find ways for an optimization of the target material.

In this chapter the angular momentum of a charged particle will be discussed and its interaction with a static magnetic field, as well as the idea of the magnetic moment and the spin. Afterward, the number of particles is increased, which leads right to the concept of the polarization. Next, an introduction to the basic ideas of manipulating the polarization over the *dynamic nuclear polarization* (DNP) will be given. Finally, methods for the detection of particle magnetism are briefly discussed.

These fundamental concepts can be found in several elementary books on quantum mechanics. A full theoretical description of the nuclear polarization is given in the work of A. ABRAGRAM and M. GOLDMAN [3, 4]. The theoretical and technical background of the *nuclear magnetic resonance* (NMR) is treated in detail in [5, 6, 7, 8].

### 2.1 Basic Principles

The angular momentum of a charged particle is always linked to a magnetic moment, which can be demonstrated best by the classical *orbital angular momentum*. In Bohr's atomic model, an electron travels around the nucleus in a circular orbit and can be expressed as

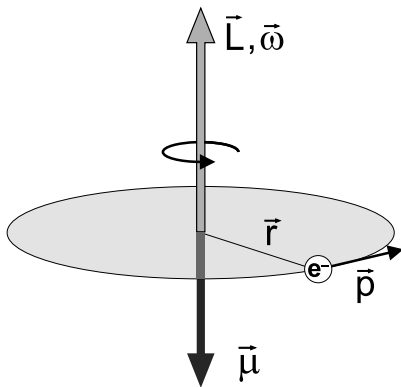


**Fig. 2.1** — Classical orbital angular momentum of an electron around a nucleus.

$$\vec{L} = \vec{r} \times \vec{p} \quad , \quad (2.1)$$

with  $\vec{r}$ , being the distance to the rotation axis (the proton) and  $\vec{p}$ , the momentum of the electron. The electron is negatively charged and generates a circular current  $I$ , as in

$$I = \frac{e}{t} = e \frac{\omega}{2\pi} \quad . \quad (2.2)$$

A moving charge is always connected to a magnetic field and on a macroscopic scale, the field appears like a magnetic dipole, whose moment is equal to the current multiplied by the enclosed area.

Therefore, the magnetic moment and the angular momentum are connected over

$$\vec{\mu}_L = -\frac{e}{2m_e}\vec{L} = -\gamma\vec{L} \quad , \quad (2.3)$$

which is illustrated in Fig. 2.1. The sign is a result of the negative charge and  $\gamma$  is called the *gyromagnetic ratio*. The magnetic moment in (2.3) can take any values, since  $\vec{L}$  is arbitrary. However, at these microscopic scale, we have to consider quantum mechanics, instead of a classical approach. In quantum mechanics, the observables can only appear in discrete values. The angular momentum can then be expressed with the following eigenvalue equation.

$$\hat{L}^2\psi_{lm} = l(l+1)\hbar^2\psi_{lm} \quad (2.4)$$

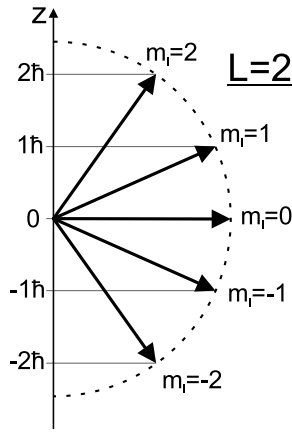


**Fig. 2.2** – Illustration of the quantum mechanical orbital angular momentum with  $L=2$ .

The quantum number  $l$  is an integer and  $\psi_{lm}$  represents the wave function of the particle. Therefore, the magnetic moment is also restricted to discrete values. In the presence of a magnetic field, the direction of the magnetic moment is also restricted and thus, the angular momentum. The field defines a preferred direction – typically the  $z$ -axis by convention – and the projection of the angular momentum to this direction is given by the equation

$$\hat{L}_z\psi_{lm} = m_L\hbar\psi_{lm} \quad . \quad (2.5)$$

The number  $m_L$  is called *magnetic quantum number* and represents possible adjustments of the spin, in relation to the static magnetic field, see Fig. 2.2. The magnetic quantum number is limited through its principal quantum number  $m_L = [-l, -l+1, \dots, 0, \dots, l-1, l]$  and can take up to  $(2l+1)$

different values. Particles have another physical property by nature, which can be described basically with the same formalism as the angular momentum – the spin.

### 2.1.1 The Idea of an Intrinsic Angular Momentum

Often, the spin is set equal to an intrinsic angular momentum, even though there is no classical equivalent for it. In our imagination, we associate the spin with a kind of an intrinsic rotation, such as the daily rotation of the earth around itself. The idea of the spin was first suggested by G. E. UHLENBECK and S. GOUDSMIT in 1926, to explain spectra of one-electron atoms [9]. The equations (2.4, 2.5) can still be used, but with a careful look on its notations. Instead of  $L$ , the spin is getting the letter  $S$ , which may be an integer or half-integer value, now. For a spin-1/2 particle like the electron, these equations transform to

$$\begin{aligned} \hat{S}^2 &= s(s+1)\hbar^2 = 3/4 \hbar^2 \quad , \quad \text{with } s = 1/2 \\ \hat{S}_z &= m_s\hbar \quad , \quad \text{with } m_s = \pm 1/2 \quad . \end{aligned} \quad (2.6)$$

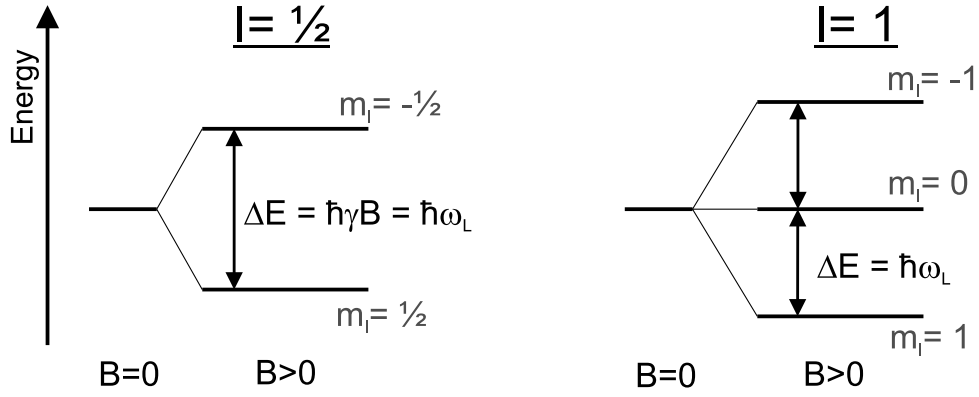


**Fig. 2.3** — Term diagram of a spin-1/2 and spin-1 nucleus. According to the Zeeman-effect, the energy splits into  $(2I+1)$  different levels, which are equidistant to each other and proportional to the static magnetic field.

But in the experiment, the magnetic moment shows a different behavior, as in the Einstein-de Haas experiment. In fact, (2.3) must be modified to comply with the experiments, which observe a slightly twice as large value as it would be classically expected for the electron. This modification is called *g-factor* and is a dimensionless number, which characterizes the relationship between the observed magnetic moment, the angular-momentum quantum number and the fundamental magnetons (Bohr-magneton  $\mu_B$  or the nuclear magneton  $\mu_N$ ).

$$\vec{\mu}_s = -g \frac{e}{2m_e} \vec{S} = -\frac{g\mu_B}{\hbar} \vec{S} = -\gamma_s \vec{S} \quad (2.7)$$

This modification is also valid for other particles or even for composed particle systems like the atomic nucleus, each with its own *g-factor*. Those systems carry a collective nuclear spin  $I$ , as a combination of the spins and angular momenta of its constituents.

### 2.1.2 Interaction with Magnetic Fields

In the presence of a magnetic field, the discrete energy state splits up, according to the magnetic quantum number, which is the basis for the polarizability of a target. The magnetic moment receives potential energy in a static magnetic field and thus, creates several different energy levels, known as the *Zeeman-effect*. The potential energy  $V$  is proportional to the applied magnetic field strength and for an electron, it can be expressed as

$$V_e = -\vec{\mu}_e \cdot \vec{B} = \frac{g\mu_B}{\hbar} \vec{S} \cdot \vec{B} = g\mu_B m_s B \quad . \quad (2.8)$$

The dot-product  $\vec{S} \cdot \vec{B} = m_s \hbar B$  represents the scalar projection of the spin into the direction of the static magnetic field. The potential energy for the nuclear spin  $I$  has the opposite sign and  $\mu_B$  must be replaced with the nuclear magneton  $\mu_N$ .

$$V_N = -\vec{\mu}_N \cdot \vec{B} = -g\mu_N m_I B \quad . \quad (2.9)$$

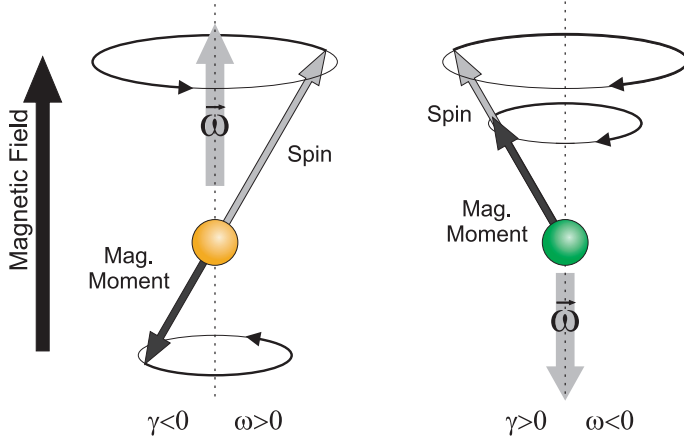


**Fig. 2.4** — Illustration of the Larmor-precession of the magnetic moments in a static magnetic field. The direction of  $\vec{\omega}$  and thus, the rotation depends on the gyromagnetic ratio  $\gamma$  and is positive for most of the particles, see Tab. 2.1.

The energy of the magnetic dipole can split up into  $(2I+1)$  different levels, as in Fig. 2.3, which are equidistant to each other with

$$\Delta E = g\mu_{B/N}B \quad . \quad (2.10)$$

The energy difference  $\Delta E$  is just the amount of energy, that is needed to elevate the particle into the next higher energy state ( $\Delta m = +1$ ).  $\Delta E$  is also the portion of energy that will be released, if the particle falls back to its next lower energy state ( $\Delta m = -1$ ). Besides mechanical collisions, this energy is generally exchanged through electromagnetic radiation, according to the relation  $\Delta E = \hbar\omega = h\nu$ .

The magnetic field creates also a torque  $\vec{T}$ ,

$$\vec{T} = \vec{\mu} \times \vec{B} \quad , \quad (2.11)$$

by the interaction of the magnetic field with the moment, which results in a precession about the field axis, with an angular frequency known as the Larmor-frequency  $\omega_L$ . By using the relationship between torque and angular momentum  $|\vec{T}| = |d\vec{L}|/dt$ , the precession frequency can be written as

$$\begin{aligned} |\vec{T}| = L \omega \sin \vartheta &= \mu B \sin \vartheta \\ \Leftrightarrow \omega &= \omega_L = \frac{\mu}{L} B \stackrel{(2.7)}{=} -\frac{g\mu_{B/N}}{\hbar} B = -\gamma_{e/N} B \quad . \end{aligned} \quad (2.12)$$

A comparison between (2.10, 2.12) reveals, that the Larmor-frequency  $\omega_L$  and the frequency in  $\Delta E = \hbar\omega$  are one and the same, with

$$\Delta E = \hbar|\omega_L| = g\mu_{B/N}B \quad (2.13)$$

and this leads to the resonance condition

$$\nu_L = \frac{|\omega_L|}{2\pi} = \frac{g\mu_{B/N}}{2\pi\hbar} B = \frac{|\gamma_{e/N}|}{2\pi} B \quad . \quad (2.14)$$

Figure 2.4 depicts the Larmor-precession of the magnetic moment and the corresponding spin.

**Tab. 2.1** — NMR properties of selected particles. The Larmor-frequency of the neutron is left empty, since no reasonable neutron target exists, except  $^2\text{H}$  [10].

Particle	Spin	g-Factor	Mag. Moment $\mu$ ( $\times 10^{-26}$ J/T)	Gyromag. Ratio $\gamma$ ( $\times 10^7$ rad/sT)	$\nu_L$ at 2.5 T $\nu_L =  \omega_L/2\pi $ (MHz)
$e^-$	1/2	-2.0023	-928.476	-1,760.86	70,062.38
n	1/2	-3.8261	-0.966	-18.32	—
$^1\text{H}$	1/2	5.5855	1.411	26.75	106.44
$^2\text{H}$ (D)	1	0.8574	0.433	4.11	16.34
$^6\text{Li}$	1	0.8218	0.415	3.94	15.66
$^7\text{Li}$	3/2	2.1707	1.645	10.40	41.37
$^{13}\text{C}$	1/2	1.4044	0.355	6.73	26.76
$^{14}\text{N}$	1	0.4036	0.204	1.93	7.69
$^{15}\text{N}$	1/2	-0.5662	-0.143	-2.71	10.79
$^{19}\text{F}$	1/2	5.2576	1.328	25.18	100.19

Table 2.1 summarizes several properties of selected particles, which are essential for the target business. Noticeable is the electron, that stands out among all the other particles. Due to its lower mass, the magnetic moment of the electron is almost 1,000 times higher than for all other nuclei, which plays a major role for the later explained DNP.

## 2.2 Polarization

The term polarization can simply be defined as a parameter, which characterizes the degree of alignment of objects in a system. In a spin-1/2 system, the state with  $m = +1/2$  may be more occupied, than the state with  $m = -1/2$  or the other way around. Therein, a distinction is made between positive and negative polarization. The vector polarization is defined as the expected value of the spin, given to a preferred direction (z-axis), normalized to the spin itself and goes over into a simple counting of states.

$$P_z := \frac{\langle I_z \rangle}{I} = \frac{\langle m \rangle}{I} = \frac{\sum_m m N_m}{I \sum_m N_m} \quad (2.15)$$

$N_m$  is the population number of the level with the corresponding magnetic quantum number  $m$ . For a spin-1/2 system, (2.15) transforms into

$$P_{z,1/2} = \frac{N_{+1/2} - N_{-1/2}}{N_{+1/2} + N_{-1/2}} \quad (2.16)$$

Therefore, zero polarization means, that the same amount of nuclei are in the state with *spin-up* as in *spin-down*, whereas at 100 % polarization, all spins have the same orientation. For a spin-1 ensemble, the vector polarization has the form

$$P_{z,1} = \frac{N_{+1} - N_{-1}}{N_{+1} + N_0 + N_{-1}} \quad (2.17)$$

By applying a static magnetic field, the system has already a non-zero polarization, depending on the field strength and temperature.

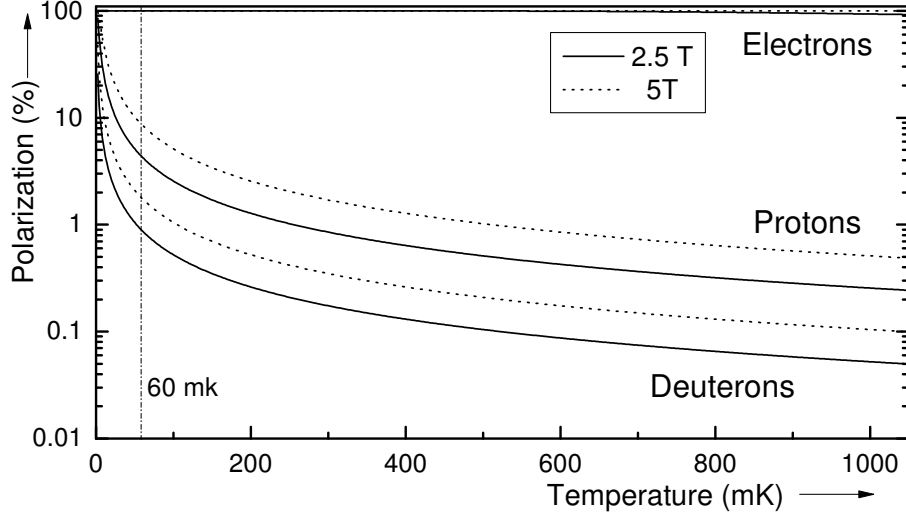


**Fig. 2.5** – TE-polarization of electrons, protons and deuterons at 2.5 T and 5 T. The mark at 60 mK refers to the typical temperature in the COMPASS refrigerator.

### 2.2.1 Polarization at Thermal Equilibrium

At *thermal equilibrium* (TE), the occupation of these energy levels can be described with Boltzmann-statistics. The occupation-number density is then given by

$$n_m = \frac{N_m}{\sum N} = \frac{1}{Z} \exp\left(-\frac{E_m}{k_B T}\right) = \frac{1}{Z} \exp\left(\frac{mg\mu_N B}{k_B T}\right) , \quad (2.18)$$

with  $Z$  as partition function and  $T$ , the temperature of the system. Together with (2.16) the TE nuclear polarization is calculable with

$$P_{z,1/2} = \frac{\exp\left(\frac{g\mu_N B}{2k_B T}\right) - \exp\left(-\frac{g\mu_N B}{2k_B T}\right)}{\exp\left(\frac{g\mu_N B}{2k_B T}\right) + \exp\left(-\frac{g\mu_N B}{2k_B T}\right)} = \tanh\left(\frac{g\mu_N B}{2k_B T}\right) . \quad (2.19)$$

Besides, the sign of the TE-polarization is fixed through the g-factor. With (2.15), the vector polarization can be generalized for any spin  $I$  to

$$P_z = \frac{\sum_m m \exp\left(\frac{mg\mu_N B}{k_B T}\right)}{I \sum_m \exp\left(\frac{mg\mu_N B}{k_B T}\right)} = \mathcal{B}_I\left(I \frac{g\mu_N B}{k_B T}\right) , \quad (2.20)$$

which corresponds to the Brillouin-function

$$\mathcal{B}_I(x) := \left(1 + \frac{1}{2I}\right) \coth\left[\left(1 + \frac{1}{2I}\right)x\right] - \frac{1}{2I} \coth\left(\frac{x}{2I}\right) . \quad (2.21)$$

The temperature and the magnetic field are the only two free parameters, over which the TE-polarization can be controlled. In order to maximize the nuclear polarization, the magnetic field must be high, whereas the temperature must be very low. This method is known as *brute-force* and reaches its technical limits quite early. Besides, the possible heat input of a beam and the magnetic deflection of the particles in a scattering experiment must be considered. Typical values are between 50 mK – 1 K and 2.5 T – 7 T for the

temperature and the magnetic field, respectively. Figure 2.5 shows the TE-polarization for electrons, protons and deuterons as a function of temperature and magnetic field. Again, the electrons take an exceptional position, due to their large magnetic moment. At typical target conditions, the electrons are practically completely polarized, while the nuclear polarization reaches only a few percent. This is not sufficient for conducting a scattering experiment, in order to obtain significant information about spin dependencies. But there is a way to increase the nuclear polarization, by using the particular characteristics of the electrons and transfer their polarization to the nuclei in a method, which is called *dynamic nuclear polarization* (DNP).

### 2.2.2 Dynamic Nuclear Polarization

The idea of exchanging spin information between two ensembles was first predicted by A. OVERHAUSER [11] and experimentally confirmed by C. P. SLICHTER and T. R. CARVER [12], both in 1953.

In order to obtain a significant improvement in nuclear polarization, a spin system is needed, which has already a high degree of polarization at typical target conditions. According to Fig. 2.5, the electrons could provide such a system. By applying microwaves to the sample with an appropriate frequency, it may happen, that the polarization of the electrons is transferred to the nuclei. These electrons must represent paramagnetic centers, whose spins are not compensated, such as unpaired electrons. The concentration (*spin density*) of these unpaired electrons plays an important role, because both, a too low and too high concentration cause a lower maximum polarization. The right amount differs from material to material, but lies in the order of  $10^{19}$  unpaired electrons per gram (spins/g). The combination of the two spin systems can be done either by adding a chemical radical to the target material or by producing the centers as a result of irradiation. The choice of the best method depends on the target material. For materials which are liquid at room temperature, it is easier to use a chemical radical, in order to dissolve it in the sample. Solid materials usually cannot be doped with chemical radicals and must then be irradiated. The latter point is described in detail in section 3.3, when it comes to the production of the ammonia target.

For the polarization mechanism, there exists more than just one theory. The Overhauser-effect describes mostly the transfer in metals and fluids, while for an insulator, the most successful models are the *solid-state effect* (SSE) and the *equal-spin-temperature theory* (EST). But which theory describes the process best depends on both, the target material and the paramagnetic centers, as well as the concentration of them.

#### Solid-State Effect

Only a few materials can be described sufficiently enough through the SSE. Nevertheless, this theory is the most accessible introduction into the polarization transfer. In the following, only spin-1/2 particles are discussed and generally, the term 'electron' refers to an unpaired electron in the meaning of a paramagnetic center.

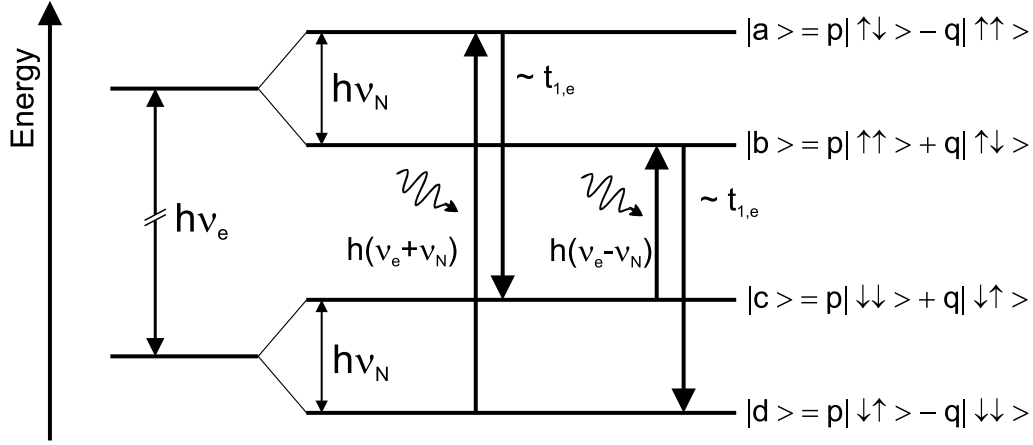


**Fig. 2.6** – Simplified scheme of the solid-state DNP process. The four states are no pure Zeeman-states, but mixed with a portion of the dipole interaction to the same electron spin. This allows both forbidden transition to happen, at a frequency  $\nu_e - \nu_N$  and at  $\nu_e + \nu_N$ , in order to create positive and negative polarization, respectively.

For electrons and nuclei, the energy levels split up in the presence of a magnetic field, according to (2.8)f, each with their own energy gap  $\Delta E = h\nu_{e/N}$ , where  $\nu_{e/N}$  is the corresponding Larmor-frequency. Due to hyperfine interaction, electrons and nuclei are coupled to each other and create four possible energy levels, as illustrated in Fig. 2.6. By inducing transitions, the selection rule  $\Delta m_s = \pm 1$  and  $\Delta m_I = 0$  must not be violated, if only the Zeeman-levels are considered. Due to the dipole character, the energy levels are not pure Zeeman-states, but mixed with a dipole term. The Hamiltonian for this situation can be expressed as

$$\mathcal{H} \simeq (\nu_e \hat{S}_z - \nu_N \hat{I}_z)_{\text{Zeeman}} + (c \hat{S}_z \hat{I}_+ + c^* \hat{S}_z \hat{I}_-)_{\text{dipole}} \simeq \mathcal{H}_Z + \mathcal{H}_D, \quad (2.22)$$

with  $c \sim \frac{\mu_B \mu_N}{r^3}$ . The result is a mixture of states to the same electron spin. The degree  $q$  of the mixture is approximately [13]

$$|q| = \frac{c}{h\nu_N} \simeq \frac{B_S}{B_0} \approx 10^{-4}. \quad (2.23)$$

Now, the mixed states allow the so-called 'forbidden transitions', in which both, the spin of the electron and the nucleus flip together. In order to induce a mutual spin-flip, the frequency of the microwaves must be either the electron Larmor-frequency plus, or minus the nuclear Larmor-frequency. The excited state has a lifetime in the range of milliseconds [14], in which the electron/nucleus-system falls back to a lower energy state. In the lower state, the electron spin has flipped back, whereas the nuclear spin still remains in the altered situation for minutes or even thousand of hours (*frozen-spin-mode*). This mechanism generates an overpopulation of one of the nuclear Zeeman-states, in which the nuclear spin has flipped compared to its initial state.

$$d : \downarrow_S \uparrow_I \xrightarrow{\text{microwave irradiation}} a : \uparrow_S \downarrow_I \xrightarrow{\text{electron relaxation}} c : \downarrow_S \downarrow_I$$



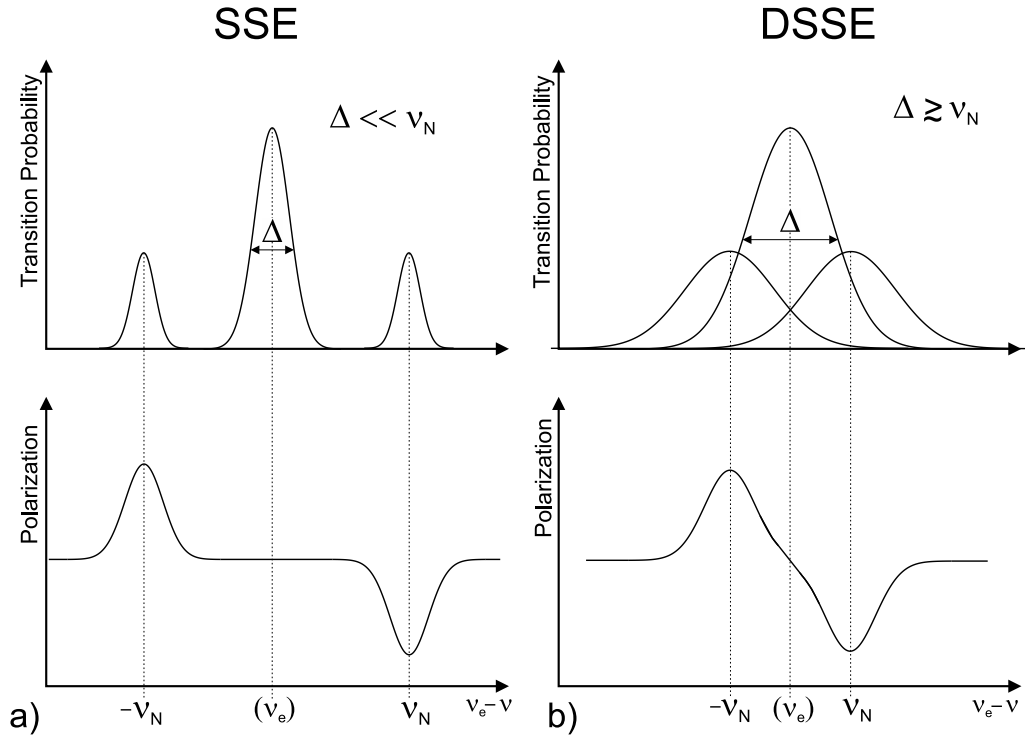


**Fig. 2.7** — Demonstration of the difference between solid-state (SSE) and differential solid-state effect (DSSE).

A microwave frequency of  $\nu_e - \nu_N$  increases the population of the low-energy nuclear Zeeman-level and the combination  $\nu_e + \nu_N$  enriches the higher Zeeman-state. The first case leads to a positive nuclear polarization, whereas the second case is referred to as negative polarization. After the relaxation, the electron is ready for a new spin-flip with another nucleon from its surrounding, since there are much less unpaired electrons as polarizable nuclei in the target material.

Theoretically, it would be possible to achieve a nuclear polarization as high as the electron polarization, but several factors limit the maximum polarization degree. Besides the relaxation times, the spin density is an important factor. The electrons may act not only as 'sources', but also as 'drains' for the polarization, meaning a relaxation channel for the nuclei. Impurities or crystalline imperfections provide other possible relaxation channels, a kind of 'polarization leakage'.

The SSE is a vivid description of the polarization mechanism, but not applicable for the most materials in his pure form. For a resolved SSE it is mandatory, that the width of the paramagnetic (electronic) resonance is smaller than the nuclear Larmor-frequency. However, usually the width of the paramagnetic resonance is in the same order of magnitude or even larger than the nuclear Larmor-frequency, especially for deuterons with their relatively small specific frequency, see Tab. 2.1. In this case, both 'forbidden' transitions may be driven simultaneously by the microwaves, which leads to a smaller maximum polarization. This behavior is referred to as the *differential solid-state effect* (DSSE), but even this approach fails in certain materials, such as alcohols and diols. A thermodynamic approach, however, in which the Zeeman-levels are considered as a kind of heat reservoir, can provide a remedy.

### Equal-Spin-Temperature and Thermal-Mixing

The *equal-spin-temperature theory* (EST) assumes, that in addition to the lattice temperature, each spin system and interaction have their own respective temperature, which reflects its occupation-number distribution. The experiments show, that the optimal polarization frequency is not  $\nu_e \pm \nu_N$ , and more than just one nuclear species can be polarized with the same microwave frequency. Even a polarization transfer between different nuclear species takes place [15]. Figure 2.8 demonstrates, that both nuclei in  $^7\text{LiH}$  polarize at the same microwave frequency, although the Larmor-frequency of hydrogen is more than twice as large as that of lithium, see Tab. 2.1.

The basis for this theory was established by A. G. REDFIELD in 1957 [16] and later used for the DNP by ABRAGAM and GOLDMAN. In the SSE, only a single electron and a nucleon is considered, but in the EST, the interaction of the electrons among themselves is taken into account. Through the dipole-dipole interaction, the discrete energy levels of the electrons change into continuous bands, in which the population density is characterized through the Boltzmann-statistic

$n(E) \propto \exp(-E/k_B T_{SS})$ . In the thermodynamic concept, the dipole-interaction is associated with an energy reservoir itself, having an own temperature  $T_{SS}$ . All other interactions, linked to the DNP, become also assigned to energy reservoirs, each with its own individual temperature. Thus, the Zeeman-reservoirs of the electrons and nuclei are assigned to  $T_{Ze}$  and  $T_{ZN}$ , respectively, which are connected to the polarization by (2.20). At TE, all temperatures are equal to the lattice temperature  $T_L$ , usually the temperature in the refrigerator.

The idea is, that only the electrons are affected by the microwave irradiation in the first place, which is pictured in Fig. 2.9. In simple terms, the energy reservoir of the electrons can be cooled or heated up. Microwaves in the range of the electron Larmor-frequency  $\nu_e$  induce transitions between the Zeeman-bands, and forcing an alignment between the corresponding parts of the population density. In Fig. 2.9b, the frequency is chosen to  $\nu_e - \delta$ , in which  $h\delta$  is exactly as big as the total width of a band  $\Delta$ . At saturating irradiation, the lower edge of the upper level and the upper edge of the lower level are balancing each other. Since the frequency does not exactly fulfill the Larmor-condition, the energy difference  $h\delta$  has to be taken out of the dipole-reservoir, which results in a rearrangement within the band. The new distribution is then characterized by a smaller temperature as before, which is interpreted as a cooling of the dipole-reservoir. Thus, the Zeeman- and dipole-reservoir are thermally connected through the microwaves and a collective temperature is established among them. The cooling effect works best, if  $h\delta$  is in the size of the energy band  $\Delta$  [13].

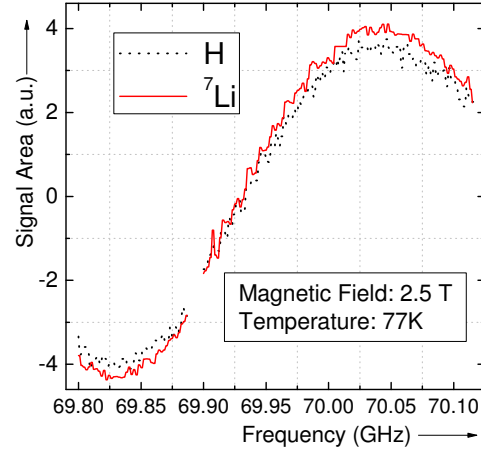


**Fig. 2.8** — Frequency curve of  $^7\text{LiH}$  at 2.5 T.

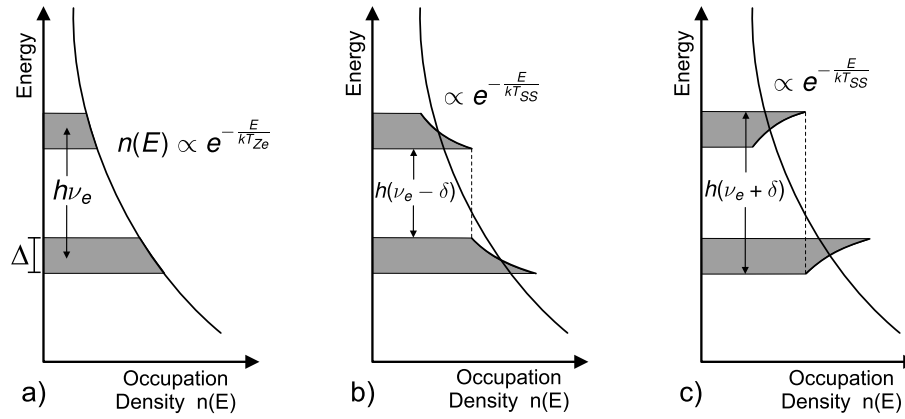


**Fig. 2.9** – Simplified representation of the occupation-number density of electrons in the spin-temperature concept. The electron-Zeeman-levels are expanded into continuous bands. At TE **a)**, the spin-temperatures  $T_{SS}$  and  $T_{Ze}$  correlate with the lattice temperature. **b)** ‘Cooling’ of non-Zeeman-reservoir ( $0 < T_{SS} < T_{Ze}$ ). **c)** ‘Heating’ of non-Zeeman-reservoir ( $0 < |T_{SS}| < T_{Ze}$ ,  $T_{SS} < 0$ ).

At a frequency of  $\nu_e + \delta$ , the opposite process takes place. Instead of taking the energy difference from the dipole-reservoir, the energy portion  $h\delta$  is added to it and leads to a heating, in which the sign of  $T_{SS}$  becomes negative, see Fig. 2.9c. As for the nuclear Zeeman- and electron dipole-reservoir, they are also in thermal contact with each other and may exchange energy. The thermodynamical analogy is the temperature adjustment between two bodies, but here, the nuclear Zeeman-reservoir can be cooled over the electronic dipole-dipole-reservoir. This process is known as *thermal mixing*.

In EST, the optimal microwave frequency is clearly dominated by the dipolar width of the electronic Zeeman-band and less by the nuclear Larmor-frequency. A scale for the dipolar width is the resonance of the paramagnetic content and depends on nature and method, of which these paramagnetic centers were brought to the target material. Several mechanisms within the material could also lead to a broadening of the spectrum, such as g-factor anisotropy and hyperfine interaction. The choice of the right paramagnetic centers depends strongly on the used target material and even external parameters may interfere with this choice, like the magnetic field [17].

### Spin-Diffusion

The spin-diffusion is a mechanism, that transports the polarization to the bulk nuclei, which may not be affected by the paramagnetic centers. The area of influence of such a center is limited and the ratio between paramagnetic centers and nuclei lies in the order of  $10^{-4}$ . The term spin-diffusion was first mentioned by N. BLOEMBERGEN in 1949, in order to explain an abnormal fast relaxation behavior in his measurements [18].

The interaction can be described as an energy conserved flip-flop-process, where adjacent nuclei execute a mutual spin-flip. One mandatory criterion for this process is the equality of the Larmor-frequencies, which corresponds to energy conservation. At this point the influence of the paramagnetic centers must be considered. The affection, which develops the DNP process, leads also to a quench of the spin-diffusion in the close range around the paramagnetic center. The dipole field of the electron causes a shift of the static magnetic

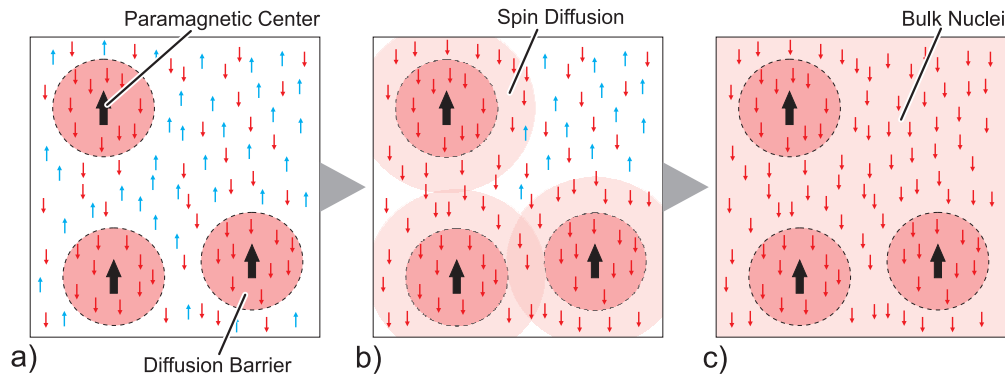


**Fig. 2.10** — Artistic illustration of the polarization process through spin-diffusion. **a)** The nuclei inside the diffusion barrier are directly polarized, but outside, the nuclei are not affected by the paramagnetic electrons. **b)** During the microwave irradiation, the surface of the barrier works as a 'polarization source'. The spin information between the nuclei is transported through dipole-dipole interaction. **c)** This process leads to a uniform polarization of the bulk nuclei.

field for adjacent nuclei, which results in a shift of their Larmor-frequencies. The circle of influence for such a paramagnetic center is limited, because the transition probability for the direct polarization process drops rapidly with  $r^{-6}$  [13]. Therefore, the region around the paramagnetic centers is called *diffusion-barrier*, which may have a size of about a few nanometers [19, 20]. Within this barrier, the nuclei are polarized directly through the interaction with the paramagnetic center, while outside, the nuclei are out of reach for the centers. Depending on the spin density, the majority of the nuclei are polarized via spin-diffusion. However, the nuclei at the edge of the diffusion barrier are still connected to the paramagnetic center as well as to the undisturbed neighbor nuclei of the bulk. In this way, the surfaces of these diffusion barriers act as 'sources' for the polarization, whereas the microwaves are turned off, the same surfaces work as polarization 'drains', just as BLOEMBERGEN had described.

One parameter stands out through the presented polarization mechanisms, and that is the concentration of the paramagnetic centers – or better, the distance of these centers to each other. In addition to the width of the electronic resonance, the distances of the centers might play a role. The SSE works best, if the paramagnetic centers are far enough from each other, so that the electron only interacts with its surrounding nuclei. At higher spin densities, the centers are getting closer together and affect each other. In EST, all centers together form an energy reservoir and the polarization process can be seen as a temperature alignment.

## 2.3 Detection of Particle Magnetism

Two basic methods are known in the target business, for the investigation of the properties of particle magnetism, which have much in common to each other. The *nuclear magnetic resonance* (NMR) is used to detect a specific nuclear species. In the end, the gathered information are used to calculate the nuclear polarization, in contrast to other common applications of the NMR, as in chemistry and medicine. The second method is dealing with the paramagnetic centers in a material, and is called *electronic paramagnetic resonance* (EPR). These paramagnetic centers are essential for the DNP process, in order to get a high nuclear polarization, as described in the previous section. Both methods induce transitions between the nuclear Zeeman-levels, but the technical background differs significantly.

In this section, only the basic ideas of NMR and EPR will be given as well as what the signal is telling us about the polarization and which additional information can be exhumed from it.

### 2.3.1 Nuclear Magnetic Resonance

The detection of nuclear resonances can be distinguished into two different kinds of NMR techniques, each with a different purpose. While in chemistry and medicine, the pulsed-NMR is used to measure position and  $T_2$  relaxation times of the resonances, in the target business, the *continuous wave NMR* (cwNMR) is still the best choice to estimate the polarization. Since in this thesis, only the cwNMR is used, a description of the pulsed-NMR is omitted. Nevertheless, the pulsed-NMR has already proofed its value to the target research, with the investigation of the electron  $T_1$  relaxation time [14], which will be continued in the doctoral thesis of J. HERICK [7].

The basic idea of the NMR is to enforce transitions in the nuclear spin system, which have an influence on the electronic measuring equipment. Therefore, a rapid-frequency magnetic field  $\vec{B}_{\text{rf}}$  is induced through a coil, perpendicularly to the static magnetic field. The frequency of the field is swept over a range around the according nuclear Larmor-frequency, in order to cover the whole resonance. The power of the rf-field is kept low, to avoid any saturating effects, which may disturb the polarization during the measurement. However, the term magnetization should be illustrated in the first place, which describes the collective behavior of the nuclear spin ensemble.

### Magnetization

In section 2.1.1, the spin of a particle is associated with a magnetic moment  $\vec{\mu}$ , which is either parallel or anti-parallel to the spin. Generally, in a static magnetic field, the Zeeman-states are not equally populated and the spins favor one direction over the other and therefore, the magnetic moments do the same. This disparity leads to a macroscopic

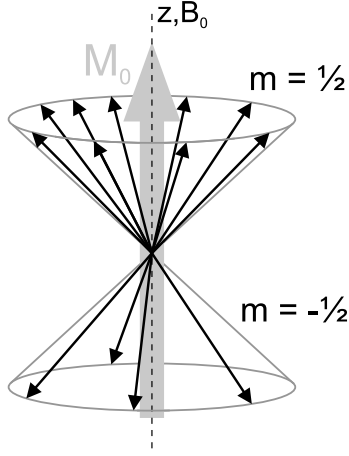


**Fig. 2.11** – Net magnetization as a result of superposition of non-canceling magnetic moments.

magnetization of the material, because all magnetic moments are summed up vectorial and a significant quantity is not compensated, see Fig. 2.11. Thus, the magnetization can be expressed as

$$\vec{M} = \sum_i^N \frac{\vec{\mu}_i}{V} \stackrel{(2.7)}{=} \gamma \sum_i^N \frac{\vec{I}_i}{V} . \quad (2.24)$$

$N$  is the total number of the respective nuclei in the volume  $V$ . At TE, the magnetization  $\vec{M}$  is aligned to the direction of the static magnetic field. For this reason, the magnetization can be rewritten with the expected value  $\langle \mu_z \rangle$  as follows

$$M_z = N \frac{\langle \mu_z \rangle}{V} = N \gamma \frac{\langle I_z \rangle}{V} \stackrel{(2.15)}{=} N \gamma P_z \frac{I}{V} \stackrel{\text{TE}}{=} M_0 . \quad (2.25)$$

In this equation, the magnetization appears as a suitable parameter, for getting information about the polarization in the first instance. Generally, the magnetization  $\vec{M}$  precesses around the direction of the static magnetic field and can take any orientation. F. BLOCH established a set of equations, which describe the movement of the magnetization vector.

### Bloch's Equations

The movement of a single magnetic moment in a static magnetic field is already given by (2.11). In combination with (2.7), the equation of motion can be written as

$$\frac{d\vec{I}}{dt} = \frac{1}{\gamma} \frac{d\vec{\mu}}{dt} \longrightarrow \frac{d\vec{\mu}}{dt} = \gamma(\vec{\mu} \times \vec{B}) . \quad (2.26)$$

By replacing the magnetic moment with its sum over all moments, the equation of motion of the magnetization can be obtained.

$$\frac{d\vec{M}}{dt} = \gamma(\vec{M} \times \vec{B}) \quad (2.27)$$

$\vec{B}$  consists not only the static magnetic field  $\vec{B}_{\text{stat}} = (0, 0, B_0)$ , but also the high-frequency field  $\vec{B}_{\text{rf}}$ , which is perpendicular to the static field and has the form

$$\vec{B}_{\text{rf}} = 2\vec{B}_1 \cos(\omega t) . \quad (2.28)$$

This oscillating field can be visualized as a composition of two counter-wise rotating magnetic fields, with the same angular frequency  $|\vec{\omega}|$ , see Fig. 2.12. But only the part with the same rotation direction as the nuclear Larmor-frequency is relevant for the resonance. The frequency of the counter-part, with the opposite direction, is out of the resonance frequency by  $|2\omega|$  and therefore, this part does not contribute to the resonance.

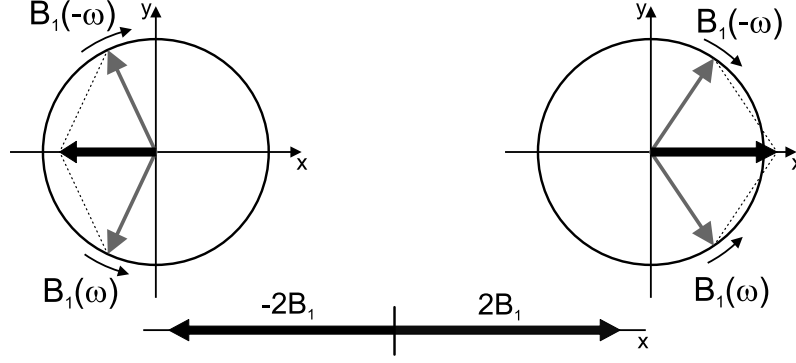


**Fig. 2.12** – Decomposition of the oscillating field in two contrarily rotating magnetic fields.

The effective magnetic field, seen by the nuclei can be written as

$$\vec{B} = B_1 \cos(\omega t) \vec{e}_x - B_1 \sin(\omega t) \vec{e}_y + B_0 \vec{e}_z \quad , \quad (2.29)$$

where  $\vec{B}_{\text{rf}}$  rotates effectively in the x-y-plane. Basically, the equations of motion are the result of the combination of (2.27, 2.29), but an important property has not been taken into account yet - the relaxation.

### Relaxation

The magnetization tends to be parallel to the applied magnetic field and if the vector is tilted away, the system returns to this state within two characteristic relaxation time constants,  $T_1$  and  $T_2$ . BLOCH used exponential functions as an approach for the relaxation. The time evolution for each magnetization vector component is given by

$$\frac{dM_x}{dt} = -\frac{M_x}{T_2} \quad , \quad \frac{dM_y}{dt} = -\frac{M_y}{T_2} \quad , \quad \frac{dM_z}{dt} = \frac{M_0 - M_z}{T_1} \quad . \quad (2.30)$$

$T_1$  corresponds to the *spin-lattice relaxation*, in which the magnetization  $M_z$  converges exponentially to its equilibrium value  $M_0$ . The energy is exchanged with the lattice, by absorbing or emitting phonons.  $T_1$  is also referred to as the *longitudinal relaxation time*, see Fig. 2.13a.

In contrast to that, the *transverse* or *spin-spin relaxation time*  $T_2$  characterizes the phase-coherence of the nuclear spins among each other. This means, the similarity in precession of all spins around the magnetic field, see Fig. 2.13b. Due to interactions between the magnetic moments or inhomogeneities in the magnetic field, the precession frequencies slightly differs, which leads to a disappearance of the transverse components of the magnetization,  $M_x$  and  $M_y$ . With the complete magnetic field and (2.27), the equations of motion are given for each component as

$$\frac{dM_x}{dt} = \gamma(M_y B_0 + M_z B_1 \sin \omega t) - \frac{M_x}{T_2} \quad , \quad (2.31a)$$

$$\frac{dM_y}{dt} = -\gamma(M_x B_0 - M_z B_1 \cos \omega t) - \frac{M_y}{T_2} \quad , \quad (2.31b)$$

$$\frac{dM_z}{dt} = -\gamma(M_x B_1 \sin \omega t + M_y B_1 \cos \omega t) + \frac{M_0 - M_z}{T_1} \quad . \quad (2.31c)$$

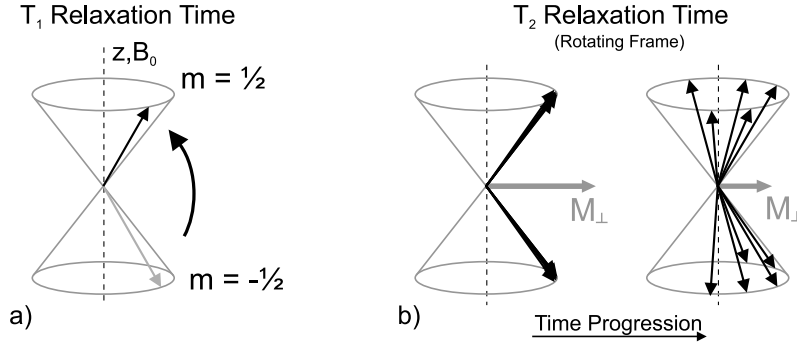


**Fig. 2.13** – Illustration of the  $T_1$  and  $T_2$  relaxation time. **a)** Longitudinal relaxation time – transition between nuclear Zeeman-levels and recovery of the equilibrium magnetization  $M_0$ . **b)** Transversal relaxation time – loss of the phase-coherence through spin-spin interaction and inhomogeneities of the local magnetic field and thus, a reduction of the transversal magnetization  $M_\perp$ .

These equations represent the links between the polarization and the measured values. In the next paragraphs, a general overview of the detection technique is given, as well as the determination of the polarization.

### Rotating Frame

To solve these equations, a transformation into the rotating frame of reference ( $x', y', z' = z$ ) is recommended, in which the x-y-plane rotates with the same frequency  $\omega$  as the oscillating magnetic field around the z-axis. The transformation can be performed with

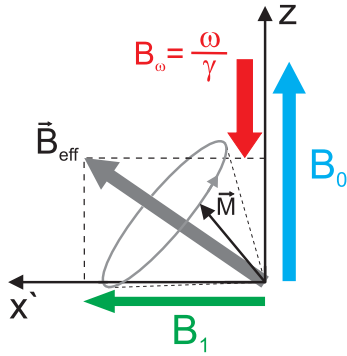


**Fig. 2.14** – Inclination of the effective magnetic field in the rotating frame of reference, depending on the frequency of the oscillating field  $B_\omega$ .

$$\left( \frac{d\vec{M}}{dt} \right)_{\text{rot}} = \gamma \left[ \vec{M} \times \left( \vec{B} + \frac{\vec{\omega}}{\gamma} \right) \right] \quad (2.32)$$

In analogy, the reduced field  $\vec{B} + \vec{\omega}/\gamma$  contributes to  $\vec{B}_{\text{eff}}$  in the same way, as the pseudo forces in non-inertial systems of classical mechanics. In this frame of reference, the effective field only consists of two components:

$$\vec{B}_{\text{eff}} = B_1 \vec{e}_{x'} + \left( B_0 - \frac{\omega}{\gamma} \right) \vec{e}_z \quad (2.33)$$

In general, the magnitude of  $B_1$  compared to  $B_0$  is so small, that only under specific circumstances, the effective field  $B_{\text{eff}}$  does not point into the direction of the static magnetic field. These circumstances are fulfilled, if the frequency of  $B_{\text{rf}}$  is close to the nuclear Larmor-frequency  $\omega_L = \gamma B_0$ . In this case, the effective magnetic field declines more and more to the  $x'$ -axis, if  $\omega$  comes closer to  $\omega_L$ . At the nuclear Larmor-frequency, the magnetization rotates around the effective field and oscillates between  $+z$  and  $-z$ , which induces transitions among the Zeeman-levels. With

$$\begin{aligned} M_{x'} &= M_x \cos(\omega t) - M_y \sin(\omega t) \\ M_{y'} &= M_x \sin(\omega t) + M_y \cos(\omega t) \end{aligned} \quad (2.34)$$



and  $\omega_1 = \gamma B_1$ , the Bloch-equations transform into

$$\frac{dM_{x'}}{dt} = (\omega_L - \omega)M_{y'} - \frac{M_{x'}}{T_2} \quad (2.35a)$$

$$\frac{dM_{y'}}{dt} = -(\omega_L - \omega)M_{x'} + \omega_1 M_z - \frac{M_{y'}}{T_2} \quad (2.35b)$$

$$\frac{dM_z}{dt} = -\omega_1 M_{y'} + \frac{M_0 - M_z}{T_1} \quad (2.35c)$$

### Continuous Wave NMR

In a cwNMR measurement, the frequency-sweep should be slow compared to the characteristic time  $T_2$ . With this argument, an approximation is made, in which the system can always be seen in a stationary state. In this approximation, the time derivation of (2.35)f vanish and lead to the following solutions.

$$M_{x'} = \frac{(\omega_L - \omega)\omega_1 T_2^2}{1 + T_2^2(\omega_L - \omega)^2 + \omega_1^2 T_1 T_2} M_0 \quad (2.36a)$$

$$M_{y'} = \frac{-\omega_1 T_2}{1 + T_2^2(\omega_L - \omega)^2 + \omega_1^2 T_1 T_2} M_0 \quad (2.36b)$$

$$M_z = \frac{1 + (\omega_L - \omega)^2 T_2^2}{1 + T_2^2(\omega_L - \omega)^2 + \omega_1^2 T_1 T_2} M_0 \quad (2.36c)$$

However, the measurement cannot distinguish between  $M_{x'}$  and  $M_{y'}$  in the first place, but detects a transverse magnetization  $M_\perp$  instead:

$$\vec{M}_\perp = M_\perp \cos(\phi) \vec{e}_{x'} + M_\perp \sin(\phi) \vec{e}_{y'} \quad (2.37)$$

with

$$M_\perp = \sqrt{M_{x'}^2 + M_{y'}^2} = \frac{\omega_1 T_2 M_0}{\sqrt{1 + T_2^2(\omega_L - \omega)^2}} \quad (2.38)$$

The transverse magnetization  $\vec{M}_\perp$  and the field  $\vec{B}_1$  are connected through the susceptibility  $\chi(\omega)$ , which depends on the frequency of  $\vec{B}_{rf}$  and has a complex nature:

$$\chi^*(\omega) = \chi'(\omega) + i\chi''(\omega) \quad (2.39)$$

Generally, the susceptibility is a proportionality factor between the applied magnetic field and the caused magnetization. It can be used to characterize the behavior of substances in the presence of a magnetic field. A distinction is made between a paramagnetic behavior, in which the field strength is enhanced within the substance ( $\chi > 1$ ), and diamagnetic, where the field is reduced in the material ( $\chi < 1$ ). However, the susceptibility is not restricted only to the magnetization, but reflects more the response of the physical system on a time-dependent excitation. With the assumption, that the magnetization has also a complex nature, the following two relations can be obtained.

$$M_{\perp}^* = M_x + iM_y \stackrel{(2.34)}{=} (M_{x'} + iM_{y'})e^{i\omega t}$$

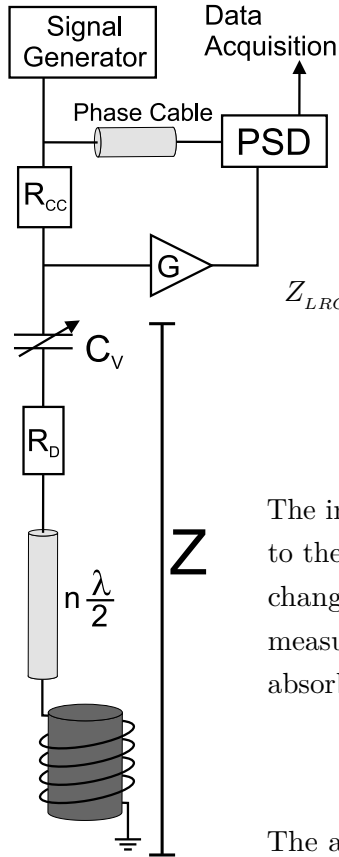
and

$$M_{\perp}^* = \frac{\chi'(\omega) - i\chi''(\omega)}{\mu_0} B_1 e^{i\omega t} \quad , \quad (2.40)$$

with the components

$$\chi'(\omega) = \mu_0 \frac{M_{x'}}{2B_1} \quad \text{and} \quad \chi''(\omega) = \mu_0 \frac{M_{y'}}{2B_1} \quad . \quad (2.41)$$

At this point, a connection can be made between the spins and the measuring system. Figure 2.15 shows a scheme of the NMR circuit, in which the coil is wrapped around the sample. The variable capacity  $C_v$ , the resistor  $R_D$  and the coil are forming the actual oscillating circuit, but only the coil is located inside the refrigerator. A coaxial-cable connects the coil with the measuring system, and its length should be a multiple<sup>1</sup> of  $\lambda/2$ , in order to reduce influences of an additional capacity or inductance at the resonance frequency. If this is the case, the impedance at the end of the  $\lambda/2$ -cable matches the impedance of the coil itself.



The coil and therefore, the inductance  $L^* = L_0(1 + 4\pi\kappa\chi^*)$  is affected by the material due to its susceptibility.  $\kappa$  represents the filling-factor of the target material in the coil. The total impedance of the resonance circuit can be formulated as follows.

$$\begin{aligned} Z_{LRC} &= R_D + \frac{1}{i\omega C} + i\omega L^* \\ &= R_D + \frac{1}{i\omega C} + i\omega L_0(1 + 4\pi\kappa\chi' - i4\pi\kappa\chi'') \\ &= R_D + \omega L_0 4\pi\kappa\chi'' + i \left( (1 + 4\pi\kappa\chi')\omega L_0 - \frac{1}{\omega C} \right) \end{aligned} \quad (2.42)$$

The imaginary part of (2.42) contains  $\chi'$ , whereas  $\chi''$  contributes only to the real part, which corresponds to the ohmic resistance. A quality change in the resonant circuit, caused by the ohmic losses can be measured through a change in the voltage, which correlates with the absorbed power of the nuclear spin system.

$$W = \Re \left( \frac{1}{2} I^2 Z \right) = \frac{I^2}{2} (R_D + \omega L_0 4\pi\kappa\chi'') \quad (2.43)$$

The absorbed energy changes the occupation of the Zeeman-states, which in turn is proportional to the occupation-number difference and thus, to the polarization.

**Fig. 2.15** – Schematic view of the cwNMR circuit.

<sup>1</sup>  $\lambda/2 = \frac{c}{2\nu}$ ,  $\nu$  is the tuning frequency of the oscillating circuit, usually the nuclear Larmor-frequency and  $c$  represents the velocity of propagation within the cable.

If all those information about the susceptibility, magnetization and the population numbers are connected, the polarization can be expressed as an integral over the frequency spectrum

$$P = k \int_0^\infty \chi''(\omega) d\omega \quad , \quad (2.44)$$

where  $k$  gathers all constants of the nuclear system and electronics.

For an experiment, the estimation of the polarization can be simplified into the following steps. First, the absorption signal at TE is measured at a known temperature and magnetic field. The area  $A_{\text{TE}}$  of the signal corresponds to the polarization  $P_{\text{TE}}$ , which has to be calculated, using (2.21). These two parameters provide a polarization-area gauge for the determination of the DNP-enhanced polarization, in which the area of the enhanced signal  $A_{\text{dyn}}$  is compared to that of the TE-state.

$$P_{\text{dyn}} = \frac{A_{\text{dyn}}}{A_{\text{TE}}} P_{\text{TE}} \quad (2.45)$$

This is the standard procedure for the polarization estimation and works only if the TE-signal is sufficiently observable, in order to calculate its area.

As for the NMR, the electrons are not directly accessible, but only through indirect processes, such as changes in the local field of the nuclei [14] or the bolometric EPR. In the latter case, the absorption of microwaves in carbon-resistors is used as an indicator for the absorbed energy of the electron spin system. Usually, these resistors have a resistance of about 70 k $\Omega$  at very low temperatures, but with microwaves, it drops rapidly to several hundred of ohms, depending on the power. For the measurement, the frequency is kept constant, while the magnetic field is changed slowly. At the resonance condition, more and more energy is absorbed by the spin system and less is deposited in the resistors, which returns then a higher resistance. But this method is very sensitive for errors and can be used only as a guidance. A similar and more accurate way is to use an EPR spectrometer.

### 2.3.2 Electronic Paramagnetic Resonance

In contrast to the NMR, the *electronic paramagnetic resonance* (EPR) is used to investigate the paramagnetic centers, which provide the ability for the DNP process. The EPR spectrometer is an important tool in the target business, since parameters such as spin densities, identification of centers and the structure of the electronic resonances can be studied. During the last decades, it was customary to use an X-band spectrometer with a microwave frequency of approximately 10 GHz. Therefore, the corresponding magnetic field lies in the range of 330 mT, in order to fulfill the electronic Larmor-condition. Obviously, this does not get along with the usual DNP experiments at higher magnetic fields, but the X-band spectra reveal much about the electronic spin system, which is very useful in the target optimization.

The physics behind the EPR is basically the same as for the nuclei. Again, transitions between the Zeeman-levels are induced, which are detected over the absorptive part of the susceptibility  $\chi''$ . A parameter is measured, which is proportional to the absorbed energy of the electronic spin system and this information can then be used to determine the amount of paramagnetic centers within the target material.

The setting of the used X-band spectrometer is described in detail in [21], therefore, only the basic principles are given in the following and a simplified structure of the apparatus is shown in Fig. 2.16.

### Operating Mode

In fact, there are two possibilities to fulfill the Larmor-condition, either by varying the frequency and keeping the magnetic field constant or the other way around. The first possibility is realized in the cwNMR method, but there are technical restrictions for the EPR spectrometer. The energy for the transitions is taken from a microwave field, therefore it is necessary to create a region with a high energy density. This can be achieved through a microwave resonator, which then operates only at a fixed frequency. For this reason, the frequency is kept constant, whereas the magnetic field is swept over the resonance. After the sample is loaded, the microwave frequency of the spectrometer is adjusted to the resonance frequency of the resonator. In this case, a stationary wave is formed and nothing is reflected from the resonator. If the Larmor-condition is fulfilled, microwaves are absorbed by the spin system, which changes  $\chi$  and thus, the impedance of the resonator. Therewith, the resonance frequency does not match anymore and a part of the microwaves

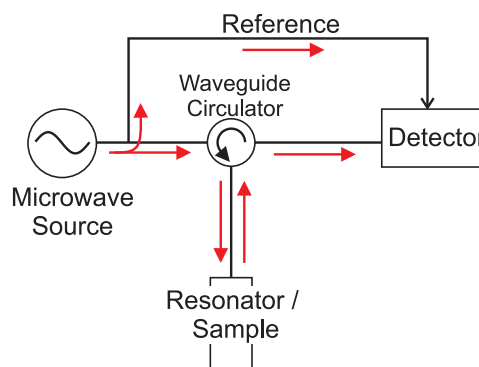


**Fig. 2.16** – Simplified scheme of an EPR spectrometer.

is reflected by the resonator. The power of the reflected microwaves is directly proportional to the absorbed energy of the electronic spin system. The spectrometer consists of two equal-length measuring-branches, supplied by the same microwave generator. One branch is used for the measurement of the sample, as describes before and the second branch is used as a reference. At the end of the spectrometer, Schottky-diodes are placed, detecting the incoming microwaves of both branches. The reflected signal contains the dispersive component  $\chi'$ , as well as the absorptive component  $\chi''$ , which are phase-shifted to each other by  $90^\circ$ . In order to observe only the absorption, the phasing in the reference branch can be tuned, to particularly suppress the dispersive part, as a result of superposition of waves.

To estimate the total spin density, first, a reference sample is needed, with a known concentration of paramagnetic centers. A mixture of butanol with the TEMPO radical<sup>2</sup> has been found to be very useful, since the radical is quite stable, dissolves well in butanol

<sup>2</sup>TEMPO stands for 2,2,6,6-Tetramethylpiperidinyloxy,  $C_9H_{18}NO$ , CAS 2564-83-2.

and has only one unpaired electron per molecule. After a sample is prepared with a known concentration<sup>3</sup>  $C_{\text{ref}}$ , its resonance signal is recorded, whose area is proportional to the number of unpaired electrons. From now on, it is the same way as in the determination of the dynamic polarization of the nuclei. Assuming, that the external conditions are consistent, such as temperature and magnetic field as well as all measuring parameters, the unknown spin density  $C_{\text{dest}}$  of another sample can be derived from the area of its resonance signal

$$C_{\text{dest}} = \frac{K_{\text{dest}}}{K_{\text{ref}}} C_{\text{ref}} \quad . \quad (2.46)$$

Since the resonance signal is proportional to the total number of unpaired electrons, the area  $A$  must be scaled by the weight  $M$  of the sample,  $K = A/M$ , to make it comparable. The dimension of the spin density is radicals or spins per gram.

### Summary

This chapter has shown, that the polarizability of a substance is the consequence of the magnetic properties of particles. A magnetic moment, linked to the spin of the particle, interacts with a magnetic field and can take one of the  $(2S+1)$  Zeeman-states. The magnetic moments precess around the direction of the applied magnetic field, with the so-called Larmor-frequency  $\nu_L$ . At the same time, the Larmor-frequency is also connected to the transition-energy between the Zeeman-states and this results in the resonance condition

$$\nu_L = \frac{|\gamma|}{2\pi} B \quad .$$

Once in an ensemble of particles, the energy levels are unequally occupied, the spin system is polarized. In a presence of a static magnetic field and at TE, a small fraction of the nuclei is already polarized. In order to enhance the polarization, a method called DNP is used, in which the high polarization of the electrons is transferred to the nuclei. Several models exist to describe the polarization transfer, each with different boundary conditions.

The polarization can be detected by the NMR spectroscopy, in which transitions between the nuclear Zeeman-states are induced, according to the resonance condition. The amount of the change of the occupation-numbers, and hence, the absorbed energy is directly proportional to the polarization degree. The resonance signal of the TE-polarization at a known magnetic field and temperature is used as a calibration for the enhanced signal, in order to calculate the dynamic polarization.

The properties of the paramagnetic centers can be investigated with an EPR spectrometer, which follows the same physics as the NMR, but differs in technical issues. With the EPR, parameters are studied, such as spin density and the line-width, which are important for the improvement of the target material.

---

<sup>3</sup>For example a fraction of 0.5 % in weight of the solvent.



## Ammonia as a Polarizable Target Material

*'Why of all things, would someone choose ammonia as a polarized target?'* This question should be pursued in the following paragraphs.

Naturally, ammonia only occurs in small fractions in nature, mostly in the putrefaction of animal excrements. But ammonia is also formed as an intermediate in the conversion process of amino acids and eliminated from the body as urea<sup>1</sup>. Since 1910, ammonia can be synthesized with the Haber-Bosch process by combining nitrogen and hydrogen gas directly, in the presence of a catalyst. Ammonia is one of the most produced chemical products in the world, with a world-wide production output of 143 million tons in 2013 [22]. The overall use of ammonia is the fertilizer business, with a quota of about 80 % of the global production. Other applications are mainly the production of nitric acid and thus, as an explosive, and as an intermediate product of plastics. Liquid ammonia can also be used as a coolant, due to its relatively high evaporation enthalpy at  $-33^{\circ}\text{C}$ .

Ammonia is a toxic and strongly corrosive gas with a pungent smell and can be dangerous even in very small concentrations of  $\sim 100$  ppm [23]. The handling of this substance is associated with strict safety procedures, such as the use of gas masks and air exhaust units. On the other hand, the advantages of ammonia for the target business justify the efforts and are found in the structure and other physical properties, such as a good radiation hardness. But first, a look on the characterization of ammonia is taken.

### 3.1 Ammonia – a Portrait

The ammonia molecule ( $\text{NH}_3$ ) consists of a nitrogen and three hydrogen atoms and has an almost tetrahedral shape, but with a bonding angle of  $106.7^{\circ}$  between two adjacent hydrogen atoms ( $\text{H-N-H}$ ), see Fig. 3.1 [10]. At room temperature and normal pressure, ammonia occurs as a gas and has a boiling point of  $-33.3^{\circ}\text{C}/239.8\text{ K}$ , which is relatively high compared to other molecules with a similar structure. This anomaly is caused by hydrogen bonds, which are also responsible for the high evapora-

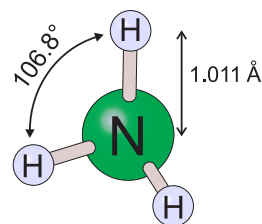


**Fig. 3.1** – Artistic view of an Ammonia molecule.

<sup>1</sup>Molecular formula of urea:  $(\text{NH}_2)_2\text{CO}$ .

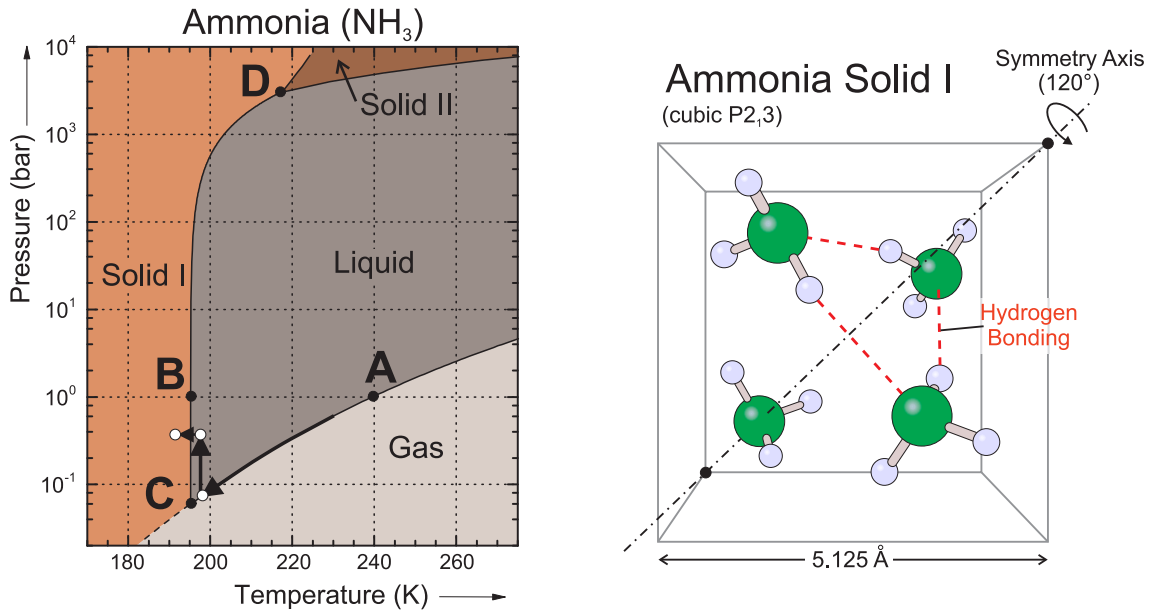


**Fig. 3.2 — Phase diagram of ammonia (left):** The filled points **A** and **B** indicate the boiling and melting point at normal pressure, whereas **C** marks the triple point of ammonia. Furthermore, **D** represents the triple point between the solid I/solid II/liquid phase. The open dots are the different working points for the ammonia solidification. Vapor/liquid line after [26], solid/liquid lines redrawn after [27], solid/gas line extrapolated. **Crystalline structure of the solid I phase (right):** A symmetry line goes diagonal through the unit cell. Only the hydrogen bonds within the unit cell are displayed. Redrawn after [25].

tion enthalpy. If the temperature falls slowly below  $-77.7^{\circ}\text{C}/195.4\text{ K}$ , ammonia turns into a transparent solid and has a crystalline structure. Ammonia has different solid phases, each distinguished by another crystal structure [24]. At pressures below 0.3 GPa, ammonia changes into a phase called *solid I*, see Fig. 3.2. In this phase ammonia crystallizes in a cubic unit cell, containing four molecules with an edge length of  $5.125\text{ \AA}$ . Each molecule is capable of establishing six bonds to other NH<sub>3</sub> molecules, both by accepting and donating three hydrogen bonds [25]. Since the nitrogen atom has only one available lone-pair of electrons, it has to be shared between the three nearest neighbors. As a consequence, the hydrogen bonds in solid ammonia are very weak, compared to that of water. X-ray studies have yielded a symmetry, which is best described with the space group P2<sub>1</sub>3 [28].

Thus, the crystal has a symmetry axis along its diagonal of the unit cell and by a rotation of  $120^{\circ}$ , the same situation is reached again, see Fig. 3.2. Ammonia can appear in different isotopic compositions, whereas nitrogen or hydrogen or both are replaced by its isotopes. Combinations like  $^{15}\text{NH}_3$ ,  $\text{ND}_3$ ,  $^{15}\text{ND}_3$  or even a mixture of hydrogen and deuterium are possible and some were already used in polarized target experiments [30]. In Tab. 3.1 some basic information about ammonia and its deuterated version are presented.

**Tab. 3.1 — Physical properties of ammonia and its deuterated version [29].**

Phys. Parameters	NH <sub>3</sub>	ND <sub>3</sub>
Molar Mass (g / mol)	17.03	20.50
Boiling Point (K)	239.8	242.3
Melting Point (K)	195.4	199.2
Density (g / cm <sup>3</sup> )		
– Gaseous at 298 K	0.00077	0.00081
– Liquid at 239.8 K	0.681	n/a
– Solid at 77 K	0.817	1.020
Dilution Factor	0.176	0.300



### 3.2 Ammonia Target – Pro vs. Contra

For a polarized target, it depends on the optimal interplay of many parameters. Some of these parameters are not predictable and therefore, they require a certain amount of experience and extensive series of experiments. Other parameters, however, are fixed by the choice of material. A selection of parameters is summarized below, of which one should be aware of [31].

- Dilution factor  $\rightarrow$  total nuclear content
- Density of the paramagnetic centers
- EPR line-width and origin of the paramagnetic centers
- $T_{1,e}$  relaxation rates of the electrons
- Nuclear relaxation rates and DNP mechanism
- Spin background via spectator nuclei
- Radiation hardness
- Thermal conductivity of the material  $\rightarrow$  filling-factor

In first place, the hydrogen content makes ammonia most interesting for the target business. Due to a hydrogen overage of 3:1 against nitrogen, the dilution factor of ammonia is one of the highest among the polarized solid targets for protons. The dilution factor represents the ratio of polarizable nuclei to the total number of nuclei in the molecule, for a specific nuclear species. In case of ammonia and the polarizability of protons, the factor is given by three polarizable protons in hydrogen, whereas the 14 nuclei in nitrogen are not available for the proton polarization. Therefore, the dilution factor of ammonia has a value of

$$f_{\text{NH}_3} = \frac{3}{14 + 3} = 0.176 \quad . \quad (3.1)$$

As a comparison, butanol has a dilution factor of only 0.135, which is another standard material for 'proton'-targets. In Tab. 3.2, dilution factors of several common used target materials are presented. It should be noted, that if a chemical radical is added to the material, the effective dilution factor becomes smaller, depending of the nuclear content of the radical.

However, the importance of the dilution factor only becomes apparent, if the material is used in a scattering experiment. In the introduction, the *figure of merit* (FOM) was already mentioned in (1.3), which combines several parameters to a characteristic value, in order to verify the benefit for an experiment. The FOM for a polarizable solid target can be expressed as

$$FOM = P_T^2 \cdot f^2 \cdot \rho \cdot \kappa \quad . \quad (3.2)$$

Due to the quadratic contribution, the dilution factor and the target polarization have the largest impact on the FOM and therefore, the quality and economical efficiency of the scattering experiment. The filling factor  $\kappa$  is linked to the thermal conductivity and the shape of the target material. Especially in experiments with a high intensity beam, the dumped heat of the particle beam must be removed quickly, so that a loss of the nuclear polarization can be prevented [33].

**Tab. 3.2** – Compilation of dilution factors and critical doses of typical used target materials [32].

	Material and Structural Formula	Doping	Dilution Factor	Critical Radiation $\phi_0$ ( $\times 10^{14}$ Particles/cm <sup>2</sup> )
LMN	$\text{La}_2\text{Mg}_3(\text{NO}_3)_{12} \cdot 24\text{H}_2\text{O}$	chemical	0.031	$\sim 0.01$
1,2 Propanediol	$\text{C}_3\text{H}_6(\text{OH})_2$	chemical	0.108	$\sim 1$
1,2 Ethanediol	$\text{C}_2\text{H}_4(\text{OH})_2$	chemical	0.097	$\sim 2$
Butanol	$\text{C}_4\text{H}_9\text{OH}$	chemical	0.135	3–4
	$\text{C}_4\text{D}_9\text{OH}$	chemical	0.238	n/a
EABA	$\text{C}_2\text{NH}_7\text{BH}_3\text{NH}_3$	chemical	0.165	7
Ammonia	$\text{NH}_3$	irradiation	0.175	40; 300 <sup>a</sup>
	$\text{ND}_3$	irradiation	0.300	130
Lithium Deuteride	${}^6\text{LiD}$	irradiation	0.500	400

<sup>a</sup>Ammonia has multiple distinct regions of decay, see Fig. 3.9.

As for the dilution factor  $f$  and the density  $\rho$ , the values are merely fixed through the choice of material, whereas the maximal target polarization  $P_T$  and the filling factor  $\kappa$  are variable and improvable through the way of production, which is discussed in section 3.3.

The density of the paramagnetic centers is an important parameter to optimize, either by the amount of the additive or by the duration time of the irradiation. A consequence of a low concentration is a long build-up time, whereas a too high concentration results in a decrease of the achievable maximum polarization, because these centers act also as relaxation channels. As a guideline, concentrations of the order of  $2 \times 10^{19}$  spins/g were found to be suitable for most of the materials. The nature and origin of these centers are essential for the polarization efficiency. For target materials like butanol, the advantage lies in choosing between several different radicals, whereas the only way to adequately dope ammonia is by irradiation. Thus, there is no control over the radical types and other side products (lattice defects). This matters, because the width of the EPR-line has a significant influence on the efficiency of the polarization transfer and should be as small as possible, especially in combination with deuterated materials. Also the dominant broadening mechanism should be considered, which forms the EPR-structure as well as its behavior at various magnetic fields. It may happen, that a certain radical works best for 2.5 T, but fails at higher magnetic fields like 3.5 T or 5 T [17].

During the irradiation, the radicals and thus, the width of its resonance cannot be chosen, but this drawback turns into an advantage as soon as the target is used in an experiment with a high beam intensity. First, the dilution factor is not diminished by additives and with that, the radiation hardness of ammonia is improved by several orders of magnitude, see section 3.4.

For an efficient polarization transfer and a high maximum polarization, the relaxation rates of the electrons and the nuclei are important. Considering, that an electron can only polarize nuclei directly within the diffusion barrier, only around 300-600 nuclei are in their range<sup>2</sup>. If the relaxation times of the electrons  $T_{1,e}$  are too long, the polarization build-up is significantly slowed down. For shorter relaxation times, the transition rates rise, but also

<sup>2</sup>Only 10-20 % of the nuclei are in the sphere of influence of a paramagnetic electron.

the needed microwave power, which then leads to a heating of the sample. In the doctoral thesis of C. HESS [14], the correlation between  $T_{1,e}$ -time and the polarization build-up time could be well demonstrated.

With the knowledge of the DNP process, not only a prediction of the best polarization frequencies can be made, but also information about the polarization of other nuclei in the material might be obtained, which carry a spin. In ammonia, nitrogen can be polarized too, whereas in hydrocarbons and alcohols the carbon and oxygen nuclei are spinless and thus, cannot be polarized<sup>3</sup>. Experiments like COMPASS

cannot distinguish the scattering of protons between hydrogen and nitrogen. Therefore, the polarization of all other nuclei species must be known. The measurement of the nitrogen polarization in ammonia is a difficult task, due to a large quadrupole moment of  $^{14}\text{N}$  (spin-1 particle), the width of the resonance signal is so big, that it cannot be recorded in a single shot<sup>4</sup>. Systematic studies have shown, that the nitrogen polarization can be calculated with the knowledge of the hydrogen polarization [35]. This is possible, because the polarization process in ammonia is dominated by the EST, in which the Zeeman-reservoirs of hydrogen and nitrogen are in contact with each other and have the same spin-temperature. Figure 3.3 compares the measurement of the relation between the nitrogen and proton polarization to the theoretical prediction. In EST, the relation is only determined through the magnetic moments and the g-factors of the different nuclei. However, with improved measuring methods, small deviations from the pure EST behavior could be revealed for proton polarization above 50 % [34]. In deuterated ammonia it could even be shown, that there is no exchange between the deuterons and the non-substituted hydrogen and thus, the EST cannot be used to describe the transfer process in this case [36].

As soon as some of the basic knowledge is clarified, the target has to be tested in an experiment, whether it is suitable or not.

### Experiments with Ammonia Targets

Ammonia replaced the previously used standard materials for protons, like *lanthan magnesium nitrate* (LMN) or ethylene glycol. First studies were approached at the end of the 1960s and in 1970, the protons in ammonia were dynamically polarized for the first time at CERN. By adding a chrom(V)-complex, proton polarizations up to 40 % were achieved at 1 K and 2.5 T [37]. With an ethandiol-Cr(V)-complex, even 70 % were achieved,

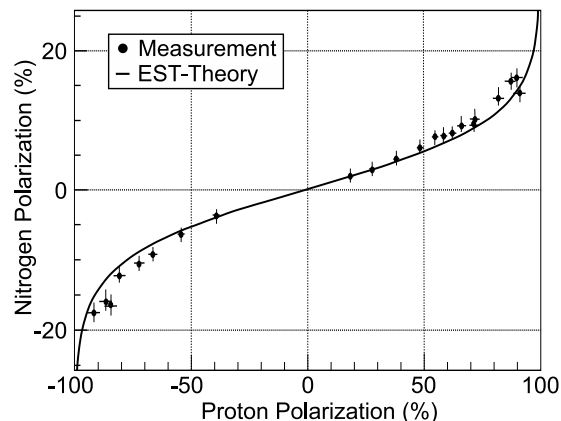


**Fig. 3.3** — Study of EST in ammonia  $^{14}\text{NH}_3$ . The solid line represents the pure EST behavior, in which the proton-reservoir has always the same spin-temperature as the nitrogen-reservoir, redrawn after [34].

<sup>3</sup>But some of their isotopes are polarizable, such as  $^{13}\text{C}$ , which has a spin of 1/2.

<sup>4</sup>The resonance signal of the isotope  $^{15}\text{N}$  is smaller, because it has a spin of 1/2 and thus, no quadrupole moment.

but not reproducible. Further attempts, to introduce paramagnetic centers by adding chemical radicals, gave no satisfactory results and the development of an ammonia target was temporally set down.

In the late 1970s, it could be demonstrated, that an irradiation of solid ammonia produces paramagnetic centers, which are suitable for the DNP. Already, after a dose of  $0.95 \times 10^{15}$  protons/cm<sup>2</sup>, using a 580 MeV proton beam, polarizations of 90.5 % and -93.6 % were reached at 0.5 K and 2.5 T [38], but with a long polarization build-up time, probably caused due to a low concentration of paramagnetic centers. After this discovery, intense studies were performed at the linear accelerator in Bonn and at the SLAC on ammonia as a target material. In this time, especially the preparation method of ammonia has been optimized and the behavior of the polarization at high beam intensities was investigated. In Bonn, solid ammonia was irradiated with 20 MeV electrons up to an accumulated dose of  $10^{17}$  electrons/cm<sup>2</sup>. With this dose, a proton polarization of 60 % at 0.5 K and 2.5 T were available in only 30 min ( $\tau_{0.7} = 9$  min) after the microwaves turned on [39]. Polarizations above 90 % could be routinely achieved at 5 T/1 K or 2.5 T/0.3 K. The pre-irradiation was done at the temperature of liquid argon (-186 °C/87 K) and the  $\dot{\text{N}}\text{H}_2$  radical could be identified as the DNP-relevant center through EPR-studies, see Fig. 3.4.

With this investigation, further studies on irradiated ammonia have been triggered in other research institutes such as Brookhaven, Liverpool and Kharkow. Thereby, it could be demonstrated, that it should be distinguished between irradiation at high ( $\sim 87$  K) and low ( $\sim 1$  K) temperatures. At higher temperatures, around 100 K, some of the produced defects are not stable anymore, whereas the  $\dot{\text{N}}\text{H}_2$  radical still remains. These additional defects may have either positive or negative consequences for the polarization during the experiment. The influence on the polarization and a method, called *annealing*, are described in section 3.4, in which the polarization can be restored to its initial value – strongly connected to the radiation hardness.

In 1982, ammonia was used in a particle experiment at Brookhaven<sup>5</sup> for the first time, which studied p–p elastic scattering and profits from the good radiation hardness of the material [40]. One year later, experiments with deuterated ammonia were performed at the accelerator in Bonn, with the intention to measure the photodisintegration on  $\gamma D \rightarrow pn$ , as well as the tensor polarization of the deuteron [41]. In 1988, a collaboration between Bonn, CERN and Liverpool produced the largest irradiated ammonia target<sup>6</sup> until then, with a total volume of 2 liters. With this target the so-called ‘spin crisis’ began and triggered several follow-up experiments, see chapter 4. In several deep inelastic polarized proton/deuteron scattering experiments at SLAC, also measurements with the ammonia derivatives  $^{15}\text{NH}_3$  and  $^{15}\text{ND}_3$  were performed [30]. Nowadays, deuterated ammonia is substituted by deuterated lithium, as a standard material for deuterons, due to a larger dilution factor and even a better radiation hardness.

<sup>5</sup>The *Alternating Gradient Synchrotron* (AGS) was completed in 1960.

<sup>6</sup>Contrary to later productions, this target material was produced in little spheres, as a result of dropping liquid ammonia into nitrogen.

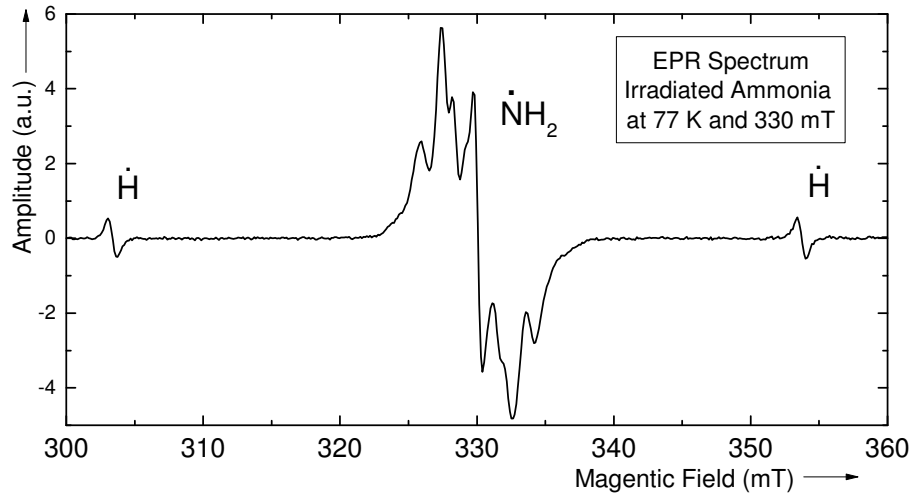


**Fig. 3.4** — Extended X-band EPR-spectrum of irradiated Ammonia. The satellite peaks next to the  $\dot{\text{N}}\text{H}_2$ -resonance are caused by atomic hydrogen, still trapped in the target material.

Nevertheless, ammonia has demonstrated its value to the polarized target business through its outstanding properties. Without ammonia as a polarizable target, certain experiments could not have happened, which raised fundamental questions about the structure of matter until today. The efforts behind the production of polarizable solid ammonia, are pointed out in the next section, in which the way from a gas cylinder to a highly polarizable solid target is presented.

### 3.3 Production of an Ammonia Target

The production of an ammonia target is a time-consuming procedure. Not only working with strict safety regulations, but special equipments are required, in addition to a strong radiation source, in order to activate the material for the DNP. As a result of the collaboration between the target groups of Bonn and Bochum, the production can be divided into the preparation of solid ammonia and the irradiation. Both processes were the topics of the theses of S. KUNKEL [42] and S. RUNKEL [43], with the intention to produce a new and fresh ammonia target for the COMPASS experiment in 2011. Therefore, the following is a roundup of all steps, which are necessary to obtain a highly polarizable solid ammonia target.

#### 3.3.1 Preparation of Solid Ammonia

The usual and well-established way to produce an alcohol target like butanol, is adding a chemical radical and dropping the mixture into a bath of liquid nitrogen. As a result, small amorphous spheres of 1-2 mm in diameter can be produced in a reliable way on a large scale. But ammonia is a gas at room temperature and cannot be doped with radicals. A liquefaction in the first place and dropping liquid ammonia into a nitrogen bath was tried, but as a result, the ammonia spheres were very fragile and had gas pockets in it, which led to a non-uniformity of the material and even a destruction during irradiation [29].

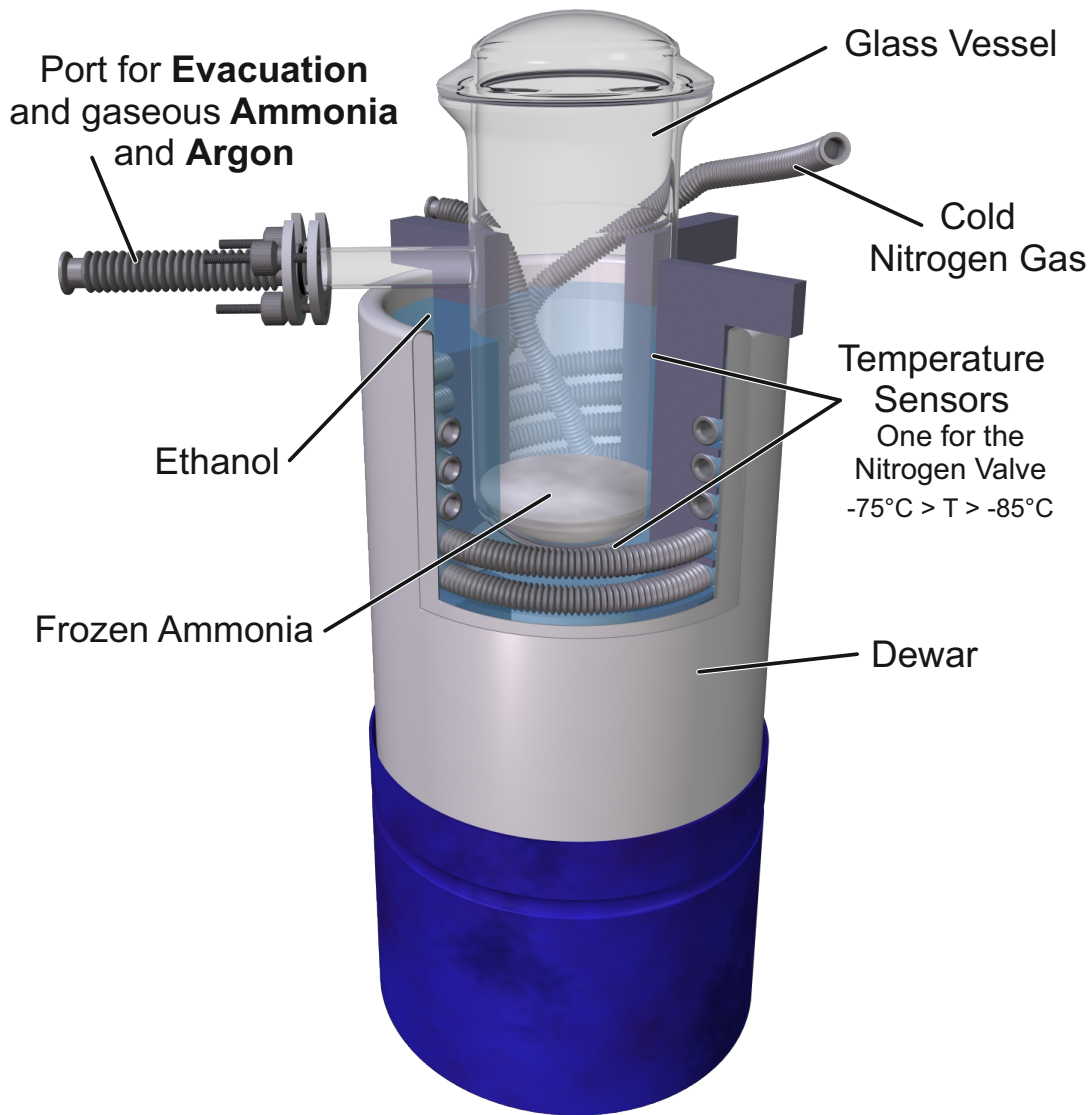


**Fig. 3.5** — Illustration of the solidification device for ammonia. The lower part of the glass vessel is emerged in ethanol, which is cooled by liquid and cold nitrogen gas, through a pipe within the bath. A valve regulates the nitrogen flow, controlled by a temperature sensor. A single port is used for the ammonia and argon gas, as well as for the evacuation at the beginning.

The solution is to freeze ammonia slowly to a solid block and then to crush it, afterward. Using this method, no radicals should be added, otherwise they would cluster during the slow freezing process and are not evenly distributed in the material. Nevertheless, ammonia would lose its benefit of having one of the best radiation hardness among the target materials, see section 3.4. Since it is not practical to introduce the paramagnetic centers into ammonia by adding a chemical radical, another method has to be found in order to place these centers. The most efficient way is to create radicals by ionizing radiation, which is the main subject of the next section.

First, ammonia has to become solid, but under controlled conditions. A picture of the used device for the solidification is shown in Fig. 3.5. The main component is a glass vessel, in which the ammonia gas condenses and is then solidified. The glass has one port for both, gas supply and evacuation, to remove unwanted residual gas. The vessel is embedded

in an ethanol bath, whose temperature can be adjusted as needed. The temperature is regulated by liquid or cold nitrogen gas, which flows through a flexible tube sunk-in in the ethanol bath. Two platinum thermoresistors are used to measure the temperature of the ethanol bath, one at the bottom of the glass vessel and a second a little bit above. These information are used to trigger a valve of the nitrogen supply, which is part of a control loop and keeps the temperature in a pre-set range.

A freezing session starts by filling the dewar with ethanol and the evacuation of the glass vessel. The temperature of the ethanol bath is pre-cooled by liquid nitrogen piped through the tube, just above the melting point of ammonia. From then on, only cold nitrogen gas is used to hold the temperature. Ammonia gas is fed into the vessel and starts to condense. Once, enough liquid ammonia is collected at the bottom of the glass, the set-points of the control loop are changed below the melting point of ammonia ( $-77^{\circ}\text{C}$ ). In consequence of liquefying, the pressure within the vessel decreases to 100-150 mbar. By adding a second gas and raising the pressure up to 500 mbar, the entire ammonia within the vessel remains in the liquid state before the freezing process starts, see Fig. 3.2. As a second gas, argon was chosen, with a boiling point of  $-186^{\circ}\text{C}/87\text{ K}$ , far away from the minimum temperature reached in this process. Under these conditions, ammonia can freeze out slowly at a temperature of  $\sim -81^{\circ}\text{C}$ . After ammonia has turned into a homogenous solid block, the vessel is opened and filled with liquid nitrogen. This ensures that ammonia does not melt during the shearing. Afterward, the shredded ammonia is sieved into small beads with a final size of 2-3 mm. The average amount of solid ammonia, produced this way was around 30 g per session and took about 8 h, whereat the freezing has taken most of the time – about 6 h.

In 2011, the three target cells at COMPASS had a total volume of about 1.5 liters. Taking into account the density of solid ammonia and the filling factor of the beads  $\kappa \sim 0.6$  [44], a total amount of at least 735 g ammonia beads were needed. But in this condition, the hydrogen in ammonia can only be polarized up to its natural value at TE, according to (2.19). The next step is the creation of the paramagnetic centers, literally through electron bombardment.

### 3.3.2 DNP-Activation of Ammonia

Since it is not possible to introduce paramagnetic centers into ammonia simply by adding a radical, the centers must be produced through radiation. For the irradiation, the frozen ammonia was shipped to the *Elektron-Stretcher Anlage* (ELSA), an accelerator facility in Bonn. The facility consists of an injector, a booster synchrotron and a stretcher ring, with a maximum energy of 3.5 GeV for polarized or non-polarized electrons. However, only the injector line<sup>7</sup> LINAC-1 was used for the irradiation, which provides an electron beam of 20 MeV. At any time, ammonia has to be sufficiently cooled, in order to keep the beads solid ( $< -77^{\circ}\text{C}/196\text{ K}$ ) and preserve the produced centers in the material ( $< -160^{\circ}\text{C}/113\text{ K}$ ). For the time during the irradiation, a special refrigerator was used, which allows a reasonable

---

<sup>7</sup>LINAC stands for Linear Accelerator.

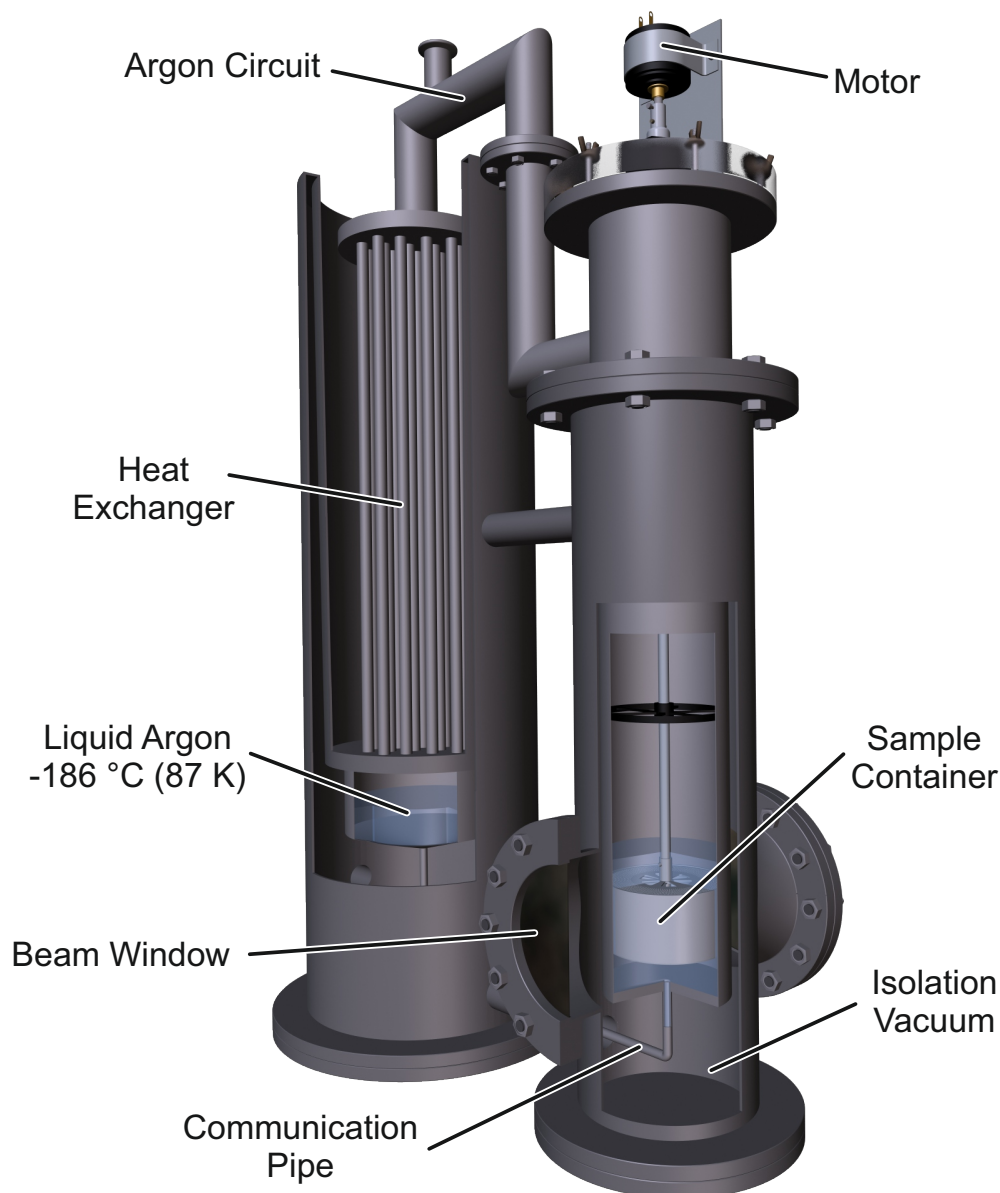


**Fig. 3.6** — Illustration of the irradiation refrigerator. The closed argon circuit is divided into an irradiation part and a liquefaction part. The latter part is triggered by the argon pressure within the circuit and regulates the argon level. In the irradiation part, the sample container is located behind the beam window and is rotated by a motor, which sits on top of the refrigerator. This should lead to a uniform irradiation of the material.

irradiation intensity and keep the temperature low enough. The first idea would simply be, to keep the ammonia under liquid nitrogen ( $-196^{\circ}\text{C}/77\text{ K}$ ) all the time, but this could be dangerous, since the electron irradiation of liquid nitrogen produces compounds, which are highly explosive<sup>8</sup>. To avoid this risk, argon is used instead of nitrogen as a cryogenic fluid, which has a slightly higher evaporation temperature of  $-186^{\circ}\text{C}/87\text{ K}$ . This temperature is sufficient to keep the  $\dot{\text{N}}\text{H}_2$  radical stable, but this is still called high-temperature irradiation, due to the fact, that the material can also be irradiated at much lower temperatures, later in the experiment.

<sup>8</sup>These explosions are caused by very rapid decomposition of ozone, formed of oxygen, which are dissolved in liquid nitrogen [45].



Due to the higher evaporation temperature, argon can easily be liquified with liquid nitrogen, which is in fact used, later during the irradiation. A first assumption would simply be, to fill an open container with liquid argon and place it in the electron beam, which works<sup>9</sup> and only needs to be refilled, if the argon level drops to a critical value. But this method has a high consumption of liquid argon and is questionable concerning radiation safety, due to activation of the volatile matter through the beam. Figure 3.6 shows the alternative, a refrigerator in which the argon is kept in a closed environment and is re-used.

The refrigerator consists of two units, which together form the circuit and both are protected by an isolation vacuum. One unit contains the actual sample and is prepared for the particle beam, whereas the other unit handles the liquefaction of argon, placed outside the beam. In the first unit, the sample is retained in a rotatable cage and directly exposed to the beam, but only separated by a 50  $\mu\text{m}$  thin titanium layer and a 2 mm thick aluminum wall. The titanium layer separates the isolation vacuum from the outside world and the aluminum wall is the boundary between the vacuum and the inner circuit. The second unit is build up of several pipes, located in a tub, which is filled with liquid nitrogen as needed. Due to their larger surface, the high number of pipes increases the efficiency of the heat exchanger. The argon reservoir in the second unit is connected over a communication pipe to the first unit and provides the needed argon level to cover the sample.

In the beginning, the circuit is filled with argon gas, which will be liquified in the heat exchanger. Once, enough argon is liquified and the sample is loaded, the circuit is closed till the end of the irradiation. The argon level within the refrigerator is regulated by a control circuit, which uses the pressure as an indicator. If the pressure exceeds a maximum value, the valve to the nitrogen reservoir opens and fills the tub of the heat exchanger. This boosts the liquefaction of argon and the pressure drops. If the pressure undergoes another set-point, the valve closes again<sup>10</sup> and the pressure rises, afterward. These set-points for high and low pressure are freely adjustable in this automatic regulation. In order to get a homogeneous irradiation, a motor on top of the refrigerator rotates the cage with roughly 30-60 rpm, but the beam spot size was too small to cover the full height of the cage. This issue was compensated by a vertical movement of the beam. A special pattern was realized, by giving a saw tooth voltage, with additional stops of 7 s at their maximum amplitudes, on the beam bending magnets of the LINAC, and this resulted in a nearly uniform intensity distribution over the height.

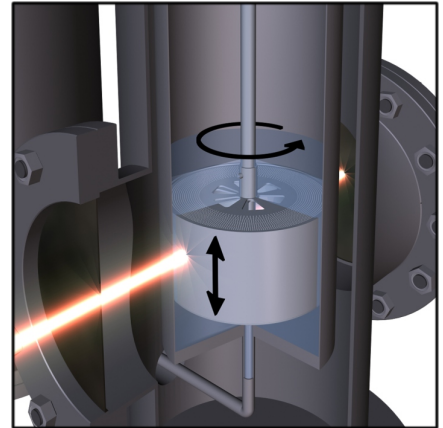


**Fig. 3.7** — Close-up view of the sample container. For a homogeneous irradiation, the container rotates and the electron beam moves up and down.

<sup>9</sup>Private communication with D. CRABB (University Of Virginia) on the PSTP2011 conference in St. Petersburg.

<sup>10</sup>To avoid a solidification of argon, the pressure must not drop below 690 mbar.

#### Irradiation Sessions at ELSA in 2011

The last time before 2011, an ammonia target for the COMPASS experiment was produced in 1995 at ELSA. This target material was used in the SMC<sup>11</sup> and then in the COMPASS experiment until 2010, which are picked up in the next chapter. For the fresh ammonia material, the target radiation dose was set to  $10^{17} e^- / \text{cm}^2$ , which is related to the dose in 1995, in order to reproduce the target material as good as possible. The LINAC emits electron packets – so-called bunches – with a repetition rate of 50 Hz and a charge of 200 nC to 300 nC per bunch. A Bergoz-monitor behind the refrigerator is used to measure the charge of these bunches, which fly through the setup<sup>12</sup>. The accumulated charge can be used as a guideline for the applied radiation dose. Based on the setup, the needed accumulated charge was estimated to be  $5.13 \times 10^8 \text{ nC}$ . Therefore, to catch up with the total charge, an irradiation time of 9 h to 14 h must be considered. All in all, nine successful irradiation sessions were done between January and March 2011 and in total 1.5 liters of irradiated ammonia beads were produced, with a work load of 150 – 170 cm<sup>3</sup> per session. This amount meets the requirements for the COMPASS target cells.

A conspicuous sign for the irradiation is a color change of ammonia into an intense purple, see the pictures in Fig. 3.8. This color can also be used to evaluate a uniform irradiation of the material. In contrast, deuterated ammonia turns into blue after the irradiation, thus the color depends on the chemical structure. Apparently, the color is a result of the irradiation, but it is not a guarantee for the ability of dynamic polarization. In fact, the color is caused by defects in the crystal structure of ammonia, but these defects are not the only ones.

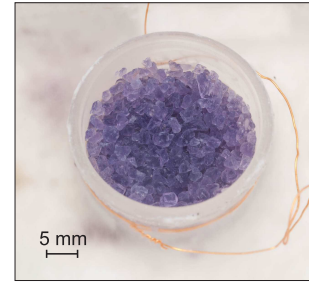


**Fig. 3.8** – The purple color of fresh irradiated ammonia.

#### Lattice and Radiation Defects

Basically in every crystal, defects occur of any kinds, which are often caused by glitches in the growth process and even the surface can be seen as a defect of an ideal crystal. Each deviation in a perfect structure is classified as a defect. Besides these 'fixed' (intrinsic) imperfections, several point defects exist, which depend upon external conditions like temperature and pressure. Thermal vibrations constantly cause changes in the local structure and thus, point defects can wander within the crystal. At TE, always a certain concentration of defects arise, and with falling temperature, the concentration decreases too<sup>13</sup>.

The point defects can be categorized into vacancies (Schottky-defects), interstitials and substitutes of impurities. The so-called F-centers<sup>14</sup> are the best studied defects, in which an electron is trapped in a vacancy, usually pictured in an ionic lattice. This kind of defects

<sup>11</sup>SMC stand for Spin Muon Collaboration.

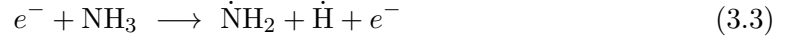
<sup>12</sup>In 1995, the shaft between cage and motor was used to measure the charge.

<sup>13</sup>It is possible to keep a higher concentration of defects at TE, by cooling the crystal very quickly. In this way, the defects are practically 'frozen'.

<sup>14</sup>From the German word *Farb-Zentrum*, meaning color center.

are able to absorb electromagnetic radiation, which may then lead to a discoloration of the crystal. In this case, the F-centers represent the simplest version of a whole class of similar defects. Other variants are called M-, R- or V-centers, however, discussing these phenomena is beyond the scope of this work [46].

In this work, the important external factor is the applied radiation dose, caused by the irradiation with high-energy electrons. In this case, the defects can be seen as a result of classical collisions, between the incoming electrons and the resting lattice. Besides the 'punch out' off its atomic place, the irradiation raises generally the lattice-energy, which increases the probability of defects in the crystal. For this reason, a concentration of defects far from its equilibrium state is possible. The defects and in particular the F-centers, may have a paramagnetic character and thus, could be candidates for the DNP process. For irradiated ammonia, EPR-studies have shown, that the  $\dot{\text{N}}\text{H}_2$  radical represents the dominant paramagnetic center, which is used later in the DNP process [47]. The origin of this radical is a separation of a hydrogen atom, caused by the interaction with an electron. This process can be pictured in the following reaction.



A look at the EPR-spectrum of irradiated ammonia (Fig. 3.4) reveals the resonances of the atomic hydrogen on both sides of the  $\dot{\text{N}}\text{H}_2$  radical, which are still trapped in the ammonia matrix. However, the strong hyperfine interaction of the electrons with the hydrogen nuclei (protons) result in a large shift of its  $g$ -factor, so that their Larmor-frequencies do not match anymore with the usually applied microwave frequency. Therefore, the  $\dot{\text{H}}$  radicals do not contribute to the enhancement of the dynamic polarization. But this does not mean that the atomic hydrogen and other defects may have no effect on the polarization at all. They may take part in the relaxation process and as a result, they could reduce the achievable maximum polarization. In general, the radical density is a parameter which has to be optimized, with a compromise between build-up time and maximum polarization, since the radicals act also as relaxation channels.

### Radical Density of Irradiated Ammonia 2011

For all nine irradiation sessions, the radical density of randomly chosen ammonia crystals were measured with the EPR spectrometer, as described in section 2.3.2. The average density was measured to

$$\bar{C}_{\text{NH}_3,2011} = (4.24 \pm 0.2) \times 10^{19} \frac{\text{spins}}{\text{g}} \quad . \quad (3.4)$$

With the same method, the radical density of the previous used ammonia at CERN was determined to

$$\bar{C}_{\text{NH}_3,1995} = (3.96 \pm 0.6) \times 10^{19} \frac{\text{spins}}{\text{g}} \quad , \quad (3.5)$$

which was produced in 1995 and 16 years old, at the point of the EPR measurement. With this result and the assumption that they were produced in the same way, the stability

of the  $\dot{\text{N}}\text{H}_2$  radical at the temperature of liquid nitrogen may be confirmed. In previous publications, much higher radical densities are given for fresh produced material, which partly exceed  $10^{20}$  spins/g [47]<sup>15</sup>, but these numbers are arguable, since the method of determination differs significantly from that of today. Before using the EPR for calculation, the radical density of ammonia was evaluated by a comparison with the relaxation time of a material (propanediol) with a known radical concentration, using the relation  $T_p \sim T_e N_e^{-1}$ , once for the ammonia and once again for the gauge sample.  $T_{p(e)}$  is the relaxation time for the protons (electrons) and  $N_e$  the radical density [36]. But this comparison is very prone to errors, not only because the electron relaxation times were quite unknown, also the type and variety of different radicals may affect the relaxation time of the nuclei.

However, the stability does not apply for all defects, which were produced during the irradiation. Figure 3.8 shows ammonia at four different time stages after the irradiation and a fading of the intense purple color is already visible after 2 weeks. Almost after a year, the ammonia beads have completely lost their color and are as transparent as before. Whether the color loss may have an influence on the polarization behavior or not, is studied in chapter 5. But, if the ammonia beads exceed a temperature of 113 K, the  $\dot{\text{N}}\text{H}_2$  radical loses its stability too and the concentration decreases significantly [21]. The temperature does not only play an important role in the conservation of the radicals during storage, but also in their production, like mentioned before. Irradiations at lower temperatures than that of liquid argon may create defects, which are only stable at these very temperatures and therefore, must be produced directly before or during the actual experiment. What happens exactly under these conditions, is still unclear and requires further investigations. But irradiation at low-temperatures could either be positive or negative for the nuclear polarization. This subject is strongly related to the radiation hardness of a target material, which is picked up in the next section.

## 3.4 Radiation Hardness of Ammonia Targets

It has been shown that for ammonia, only an intensive treatment with ionizing radiation results in a sufficiently high nuclear polarization later in the experiment, whereas the type of radiation is a matter of secondary importance in the first place. The main purpose of these targets is of course the application in a particle scattering experiment, in which they are again exposed to ionizing radiation, even if the intensity is several orders less, compared to the pre-irradiation. This means, that the polarization properties may change during the experiment, up to a major loss of its dynamic polarizability. Comparative measurements to chemical doped butanol have shown, that just the absence of added radicals are essential for the good radiation hardness of ammonia. In Fig. 3.9, the evolution of the polarization of ammonia and butanol are shown, as a function of the accumulated particles per  $\text{cm}^2$  and thus effectively a radiation dose. Notable is the fast break-in of the butanol polarization even at very low doses, whereas the polarization of ammonia also drops, but stops quickly

---

<sup>15</sup>In older publications the radical density is written in the unit spins/ml, which does not include the density of the material.

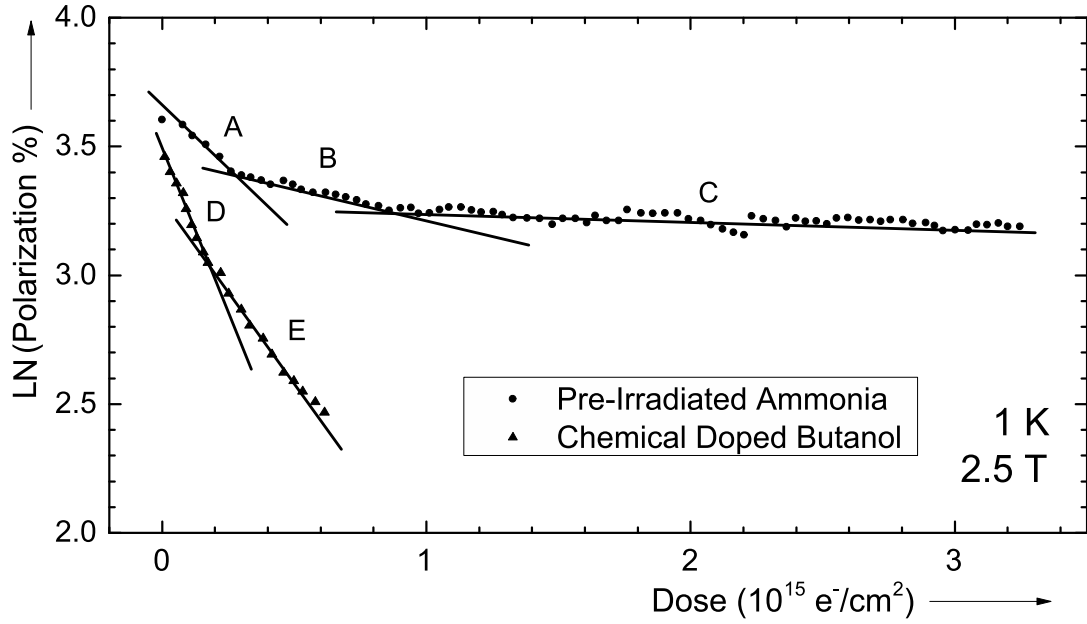


**Fig. 3.9** – Radiation damage of pre-irradiated  $\text{NH}_3$  and chemical doped butanol. Due to the logarithmic scale, several critical doses can be distinguished, for ammonia: **A** 1.0, **B** 4.1, **C** 30 and for butanol: **D** 0.38, **E** 0.66 in units of  $\times 10^{15} \text{ e}^-/\text{cm}^2$ . Redrawn after [48].

at a certain degree. The polarization loss can be described, using several exponential functions, extracting a sort of critical dose, which characterizes the radiation hardness.

$$P(\phi) = P_0 \exp(-\phi/\phi_0) \quad , \quad (3.6)$$

with  $\phi_0$  as the critical dose. In Tab. 3.2, some critical doses of target materials are collected.

Due to the ionizing radiation during the experiment, additional defects and radicals are produced, which may or may not be useful in the DNP process, but still provide relaxation channels and reducing the maximum polarization. Even material, which was not pre-irradiated becomes polarizable during the exposure, and the annealing-method works too, which speaks for a production of the high-temperature stable  $\dot{\text{N}}\text{H}_2$  radicals besides other defects, which vanish at the annealing-temperature. In Fig. 3.10 both, ammonia with and without a pre-irradiation is presented, with the interesting result, that both curves end on the same maximum polarization degree, after a certain radiation dose was applied. The annealing can be repeated many times for ammonia, having the advantage of not replacing the target material after a particular dose. With chemical doped targets, the annealing does not work very well, because not only defects and radicals are produced, but also the added radical is being irreparably damaged and cannot be used for the DNP anymore. The benefit of ammonia is also its small molecule structure, which reduces the number of different ammonia radicals. For longer molecules like butanol, the probability of creating many different radicals through fragmentation is much higher [15]. However, irradiation at low temperatures is generally not negative in the first place, for each material. Deuterated ammonia  $\text{ND}_3$  for instance, is getting a reasonable high polarization, only after an additional irradiation at low temperatures [48]. But it is still unclear, which mechanism or defects trigger this behavior.

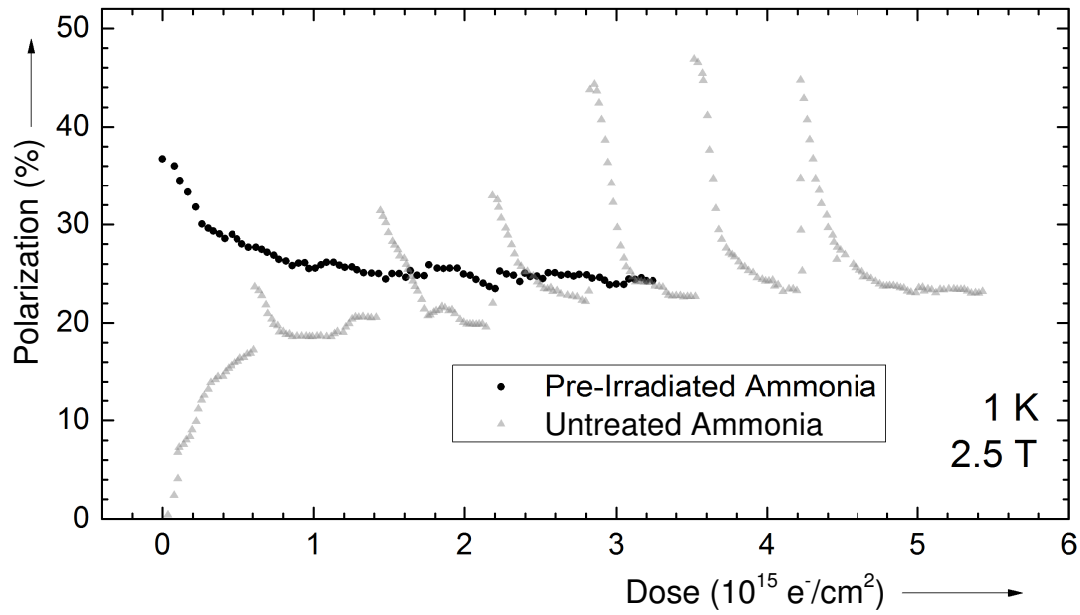


**Fig. 3.10** — Evolution of the maximum polarization of pre-irradiated and untreated ammonia. Both samples end on the same polarization degree after a certain radiation dose. The deflections of the untreated ammonia are caused by annealings. Redrawn after [48].

### Summary

This chapter should demonstrate the importance of ammonia in the target business and highlight its role, taken in past experiments. The disadvantages of ammonia, like the polarization background through spectator nuclei and the elaborate production, stand against the outstanding advantages of a high dilution factor, a high polarization ( $\sim 80\%$ ) within a relative short time (14 h, see section 5.3) and especially the good radiation hardness. By making use of the annealing-process in ammonia, the lifetime of the target material is considerably extended and does not need to be replaced after a certain dose of radiation. Already, the last point is a strong argument for ammonia as a proton target and together with the better FOM, valuable time for the experiment can be saved.

## The COMPASS Experiment

The *Common Muon and Proton Apparatus for Structure and Spectroscopy* (COMPASS) is a fixed-target experiment at the muon beam line of the *Super Proton Synchrotron* (SPS), a part of the CERN facility. It was founded in 1996 and the data acquisition began in 2002, still with the super conducting magnet of the *Spin Muon Collaboration* (SMC) experiment, which was gradually upgraded till 2005. The data acquisition continued until phase-II of COMPASS started in 2012. Almost 220 physicists from 13 countries contribute to the COMPASS collaboration [49]. The COMPASS experiment belongs to a series of pioneering experiments, not only at CERN, but also in the rest of the world, which investigate the fundamentals of the hadron structure.

In this chapter, the motivation of the COMPASS experiment is briefly discussed, but with the absence of a detailed explanation of the detector components as well as a full theoretical description of the physics program [50]. Nevertheless, an attempt is made to provide an easy-to-understand overview, mainly about the Drell-Yan program and with more emphasis given to the necessary changes of the experiment and its consequences, such as a higher ambient radiation.

### 4.1 Intention of COMPASS

COMPASS is a follow-up experiment of the *European Muon Collaboration* (EMC) and the SMC, which continues and extends the research on hadron structure and spectroscopy [51, 52].

In order to reveal the spin structure of the nucleon, measurements of single- and double-spin asymmetries in *deep inelastic scattering* (DIS) or *Drell-Yan* (DY) are preferred. First studies on the spin-dependent structure functions of the proton were done at the *Stanford Linear Accelerator Center* (SLAC) and were in agreement with the Ellis-Jaffe sum-rule, until the EMC experiment reported a violation of this sum-rule, in 1988 [53]. Instead of a polarized electron beam, the EMC experiment used a polarized  $\mu^+$ -beam, which could achieve momenta up to 200 GeV/c. The muon beam evolves from the interaction between a 400 GeV proton beam and a beryllium-target, at an extraction line of the SPS. First, pions  $\pi^+$  are produced, which then decay into muons. The muon polarization of about 80 % is naturally caused, through the parity violation of the pion decay. Due to the high energy muon beam, the lower  $x$ -region (according to the Bjorken scaling) was

observable and led to the result, that the quarks contribute only a small fraction to the spin of the nucleon.

After this unexpected discovery, several experiments tried to confirm the results and were pushed for more precise measurements, including the followed SMC experiment, from 1992 to 1996. SMC extended the  $x$ -region down to 0.004 and confirmed the violation of the Ellis-Jaffe sum-rule for the neutron in a deuterated butanol target, also with a polarized muon beam. Together with the information about the neutron, another fundamental sum-rule, the Bjorken sum-rule, could be checked and proofed of validity. The next in lineage is the COMPASS experiment, which was active between 2002 and 2012. During this period, the longitudinal spin structure functions  $g_1$  for protons and deuterons were measured with high statistics, so that the quark contribution to the nucleon spin is well known as  $\Delta\Sigma = 0.30 \pm 0.01(stat.) \pm 0.02(syst.)$ . Instead, the contribution of the gluons  $\Delta G$  was found to be very small and almost comparable with zero [54].

The basis for this kind of research is a flexible and a highly polarizable target. Therefore, **the target system can be understood as the heart of the experiment**, figuratively spoken.

### 4.2 COMPASS Target System

The COMPASS polarized target consists not only of the target material itself, but is a composition of several systems such as a dilution refrigerator, two superconducting magnet systems, microwave supply, a target containment and multiple NMR detection systems, in order to monitor the polarization of the large target.

As target materials, ammonia ( $\text{NH}_3$ ) and deuterated lithium ( $^6\text{LiD}$ ) are used to probe the proton and the neutron, respectively. Especially the radiation hardness and the high dilution factor favor ammonia among others as a proton target for COMPASS. During data-taking, a maximum polarization of 80-90 % for protons and higher than 50 % for deuterons<sup>1</sup> were achieved [56]. To get a reasonable luminosity at a beam flux of  $\sim 10^7 \mu^+/\text{s}$ , the target has to be extraordinarily large. A volume from  $850 \text{ cm}^3$  up to  $1,508 \text{ cm}^3$  was used at COMPASS during the action time, distributed over two or three cells, which could be differently polarized at the same time. This strategy is used to measure the spin asymmetry at once, with the same beam. In total, 10 cwNMR circuits monitor the polarization along the large target. The target cells are further discussed in chapter 6.

At the beginning of COMPASS, the magnet system of the SMC target system was still used, until it was replaced in 2005. With this upgrade, the opening angle of the superconducting magnet was improved from  $\pm 69 \text{ mrad}$  to  $\pm 180 \text{ mrad}$ . The large-acceptance magnet system consists of a solenoid and a dipole magnet with 2.5 T and 0.62 T, respectively and underwent a refurbishment in 2013. The solenoid magnet is used for longitudinal<sup>2</sup> polarizations, as well as to supply the magnetic field during the DNP and in general to hold the polarization. Several trim-coils along the solenoid are installed to ensure a

<sup>1</sup>Since free neutrons are not stable, the deuteron ( $^2\text{H}$  or  $\text{D}$ ) is used for probing the neutron [55].

<sup>2</sup>The terms longitudinal and transversal are used in relation to the beam direction.



field homogeneity of about  $\Delta B/B \approx 10^{-5}$  in the target region, over a distance of about  $\sim 130$  cm. The dipole magnet is used for transverse polarization and the rotation of the target polarization. After the refrigerator is operating in the so-called *frozen-spin-mode*<sup>3</sup>, the direction of the polarization can be rotated without a major loss. While the field of the solenoid is decreasing slowly, the field of the dipole is ramped up. The direction of the polarization follows the superposition of both fields, either for the transverse mode or for a complete reversal. Usually, the latter procedure is done at regular intervals to reduce systematic errors, but only during longitudinal target polarizations<sup>4</sup>. Together with the magnet system in 2005, the microwave cavity was renewed in order to match the improved opening angle and to fulfill the need of three separate target cells. The up- and downstream cell<sup>5</sup> have the same polarization direction, whereas the central cell has the opposite orientation. Two EIO microwave tubes<sup>6</sup> are used to accomplish this task, in which the up- and downstream cells are fed by the same microwave tube and the central cell with the other EIO. To reduce the influence of the microwaves at the neighbor cells, microwave stopper between the cells are used, made from a combination of a carbon-honeycomb-grid, copper-foil and -mesh. Each EIO tube has an output power of 20 W, whereat only a few watts reach the entrance of the microwave cavity, in which the electron spins absorb a power of about 40 – 400 mW during the polarization build-up [57].

An ultra-low temperature system with a high cooling power is essential to get a high nuclear polarization. The COMPASS <sup>3</sup>He/<sup>4</sup>He-dilution refrigerator is able to maintain temperatures between 100 – 300 mK during the DNP and approximately 60 mK within the data acquisition period, with the muon-beam as an additional heat source. A scheme of the refrigerator is shown in Fig. 4.1. The COMPASS refrigerator is designed as a horizontal target, which is in alignment with the particle beam. The target material can be accessed by removing the whole target holder unit, which fits exactly into the dilution refrigerator, joint with a tight indium seal. In order to minimize unwanted material in the beam line, the target holder is practically a vacuum chamber at the very upstream end. Only two 0.1 mm stainless steel windows and a bunch of aluminium foils are between the beam and the target – for the beam entrance and as thermal shielding, respectively. The mixing chamber is made of glass fiber reinforced epoxy, 70 mm in diameter and 0.6 mm wall thickness. At the the bottom of the target cells, a long CuNi tube is attached, with 40 holes, feeding <sup>3</sup>He equally into the mixing chamber. The basic principle of a dilution refrigerator can be looked up in [58].

The <sup>3</sup>He/<sup>4</sup>He-circuit is connected to eight root blowers in series, with a total pumping rate of 13,500 m<sup>3</sup>/h, which removes the <sup>3</sup>He from the diluted phased and feeding it back to the mixing chamber. A separate cooling circle (only <sup>4</sup>He) supplies the superconducting magnets and serves as a heat exchanger for the <sup>3</sup>He liquefaction. Multiple temperature sensors are installed in the vicinity of the target material as well as at critical points along

<sup>3</sup>At ultra-low temperatures ( $\sim 100$  mK), the nuclei have relaxation times of several thousand hours.

<sup>4</sup>Field rotation during transverse mode would cause more systematic errors due to changes of the beam path.

<sup>5</sup>Upstream is the first cell facing the beam, whereas downstream has a contrary meaning.

<sup>6</sup>EIO stands for Extended Interaction Oscillator.

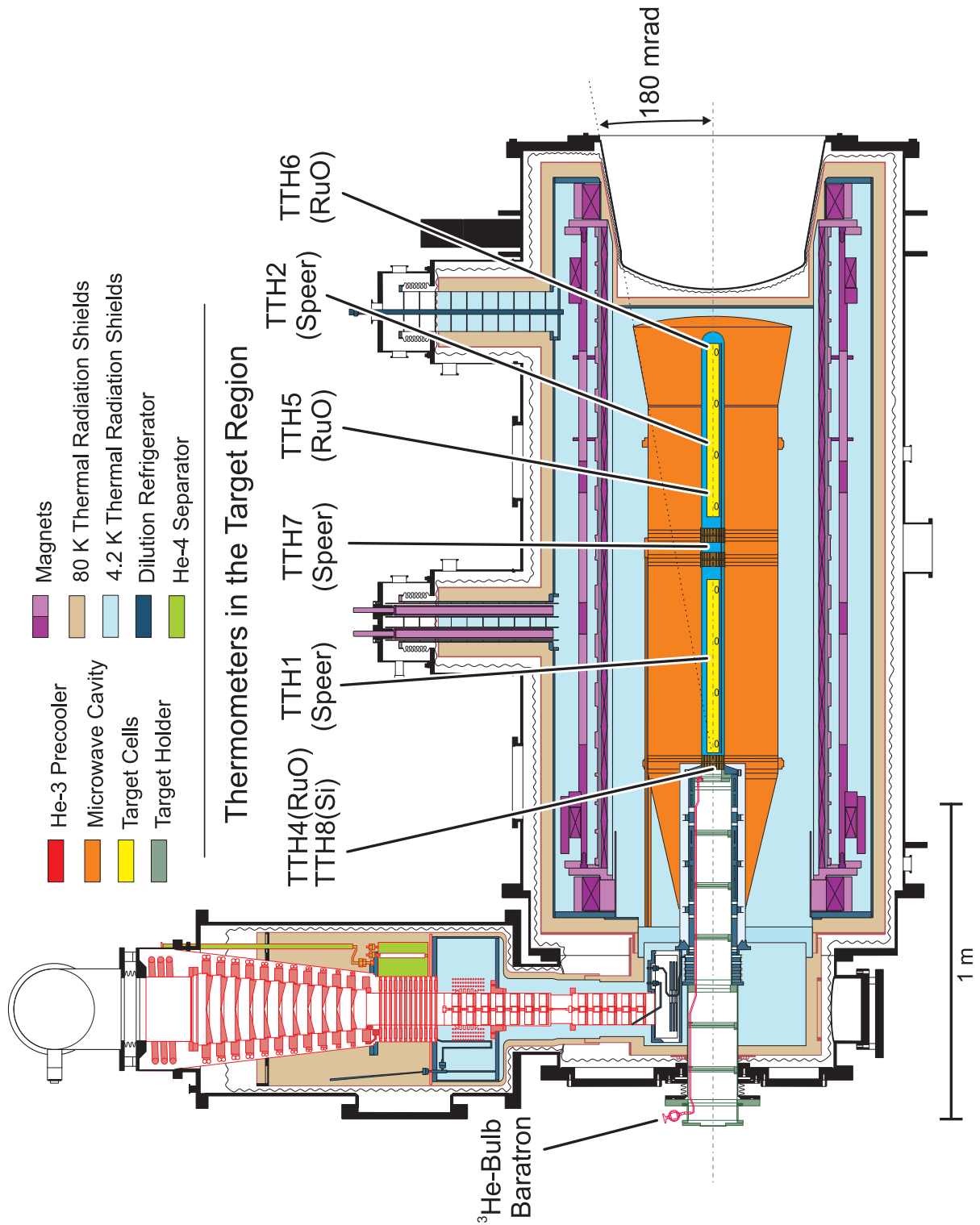


**Fig. 4.1** — Side view of the COMPASS refrigerator. This scheme shows the main parts of the COMPASS target system, the refrigerator units, the microwave cavity, magnets (dipole and solenoid) and the target holder. The horizontal broken line represents the way of the particle beam. In addition, the important temperature sensors for the target material are specified above. There are several more sensors at critical control points throughout the target system. The ruthenium-oxide resistors (RuO) are for the temperature range below 1 K, whereas the silicon-diodes (Si) are sensitive for temperatures between 1.4 K-500 K. Carbon film resistors of the company KOA Speer Electronics (Speer) are not used for thermometry, but for the estimation of the microwave absorption of the target material. The sensors TTH4 and TTH8 are located beneath the connection to the  $^3\text{He}$ -bulb (Baratron), which determines the temperature from the  $^3\text{He}$  vapor pressure [59].

**Tab. 4.1** – An overview of the COMPASS data-taking periods. Status: February 2015. The gray rows indicate shutdowns and the absence of a polarized target [52, 60].

	Period	Beam	Target	Polarization
– COMPASS –	2002-2004	$\mu^+$	neutron ( $^6\text{LiD}$ )	long. and transv.
	2005		CERN accelerator shutdown, upgrade target system	
	2006	$\mu^+$	neutron ( $^6\text{LiD}$ )	long.
	2007	$\mu^+$	proton ( $\text{NH}_3$ )*	long. and transv.
	2008-2009	hadron	hydrogen / DY beam test	
	2010	$\mu^+$	proton ( $\text{NH}_3$ )*	transv.
	2011	$\mu^+$	proton ( $\text{NH}_3$ )**	long.
– COMPASS-II –	2012	$\pi^-$	Nickel-target	–
	2013		CERN accelerator shutdown, modification for DY	
	2014	$\pi^-$	proton ( $\text{NH}_3$ )**, DY pilot run	
	2015	$\pi^-$	proton ( $\text{NH}_3$ )**	transv.
	2016-2018	$\mu^+, \mu^-$	hydrogen	–
	2019-2020		CERN accelerator shutdown	

year of production \* 1995, \*\* 2011

the cooling circuit. Most of the sensors are electronic elements, such as diodes and resistors, but there is also the option to measure the temperature over the helium vapor pressure. The pre-cooling period is mostly monitored by silicon diodes, whereas the ultra-low temperatures in the mixing chamber are best measured with ruthenium-oxide resistors. These resistors, and the method of using the vapor pressure, are also used during the TE-calibration, which is a crucial point to calculate the correct nuclear polarization, later in the experiment. During the DNP, so-called speer resistors (carbon) are used as an estimation of the absorbed microwave power (bolometric) for each cell.

In addition to the refurbishment of the magnet system, the major modifications for the target systems are limited to the close vicinity of the target material.

### 4.3 Future of COMPASS – COMPASS II

The second phase of COMPASS was approved by the CERN Research Board in December 2010 [50], which required some major modifications in the experimental setup. The physics program focuses on DY-measurements in a transversal polarized proton target, *generalized parton distributions* (GPD) in a large liquid hydrogen target and on *semi-inclusive deep inelastic scattering* (SIDIS), in parallel to the GPD-program. The polarized target will only be used during the DY-measurements and therefore, the following concentrates just on this topic.

In fall of 2014, a first pilot run for DY was performed and for 2015, a full period of 140 days is scheduled with a transversely polarized ammonia target. In the subsequent years, the GPD-program will take place and after 2018, several secondary programs are in prospect. Such as an additional run with transversely polarized protons as well as transversely polarized deuterons, unpolarized targets and with nuclear targets. Also a second period of the GPD-program with the transversely polarized ammonia target is part of the addendum.

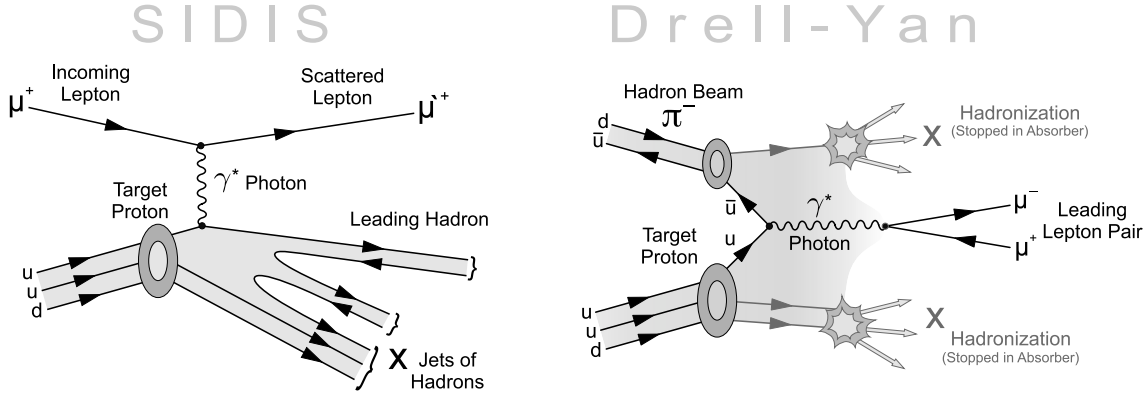


**Fig. 4.2** — Graph of the reaction processes in SIDIS and Drell-Yan. The essential difference between these two are the particles in the initial and final states. **SIDIS (left)**: In SIDIS, the initial particles are a lepton and a hadron. In the final state, a leading hadron is detected in coincidence with the scattered lepton. **Drell-Yan (right)**: Here, two hadrons are in the initial state and only the outgoing lepton/anti-lepton pair is detected. Produced particles of the hadronization are of no interest and stopped in the hadron absorber at COMPASS II.

### 4.3.1 Drell-Yan Measurement

In the DY-process, a quark  $q$  and anti-quark  $\bar{q}$  from two different hadrons, are interacting with each other, annihilate into a virtual photon, which creates then a lepton/anti-lepton pair  $L^+/L^-$ . This reaction may be simplified as

$$H_{q(\text{Target})} + H_{\bar{q}(\text{Beam})} \longrightarrow L^+ + L^- + \text{anything} \quad . \quad (4.1)$$

This process is illustrated in Fig. 4.2, in which the relevant hadrons are in the initial state, whereas in the final state, only the produced leptons become important. In the meantime, the remaining quarks are forming other hadrons. At COMPASS, the parent hadron of the anti-quark is the pion and its counterpart is coming from the target nucleon. The outgoing leptons are muons, which are detected in the COMPASS spectrometer. By measuring asymmetries at different orientations of the target polarization, information about the nucleon structure can be obtained.

In leading order, the inner structure (transverse momentum independent) of a nucleon may be represented by three so-called *parton distribution functions* (PDF),  $f_1(x)$ ,  $g_1(x)$  and  $h_1(x)$ . The *number density function*  $f_1(x)$  represents the probability distribution of finding a specific parton (quark, antiquark, gluon) with a momentum fraction  $x$  in the nucleon. The *helicity function*  $g_1(x)$  relates to the difference in probability of finding a parton with momentum fraction  $x$ , with spin parallel and anti-parallel to the parent nucleon in longitudinal polarization, whereas the *transversity*  $h_1(x)$  refers to transversal polarized nuclei. Taking into account the intrinsic transverse momentum  $\vec{k}_T$  of a parton, all in all eight *transverse momentum dependent* PDFs (TMD) describe the relation between the spin and momentum of partons to the spin of the parent nucleon, see Fig. 4.3. In the DY-program, the transversity  $h_1(x, k_T^2)$  as well as the Boer-Mulders function  $h_1^\perp(x, k_T^2)$  and the Sivers function  $f_{1T}^\perp(x, k_T^2)$  will be the focus of interest. These functions can be measured both in SIDIS and DY and should show an opposite behavior, because

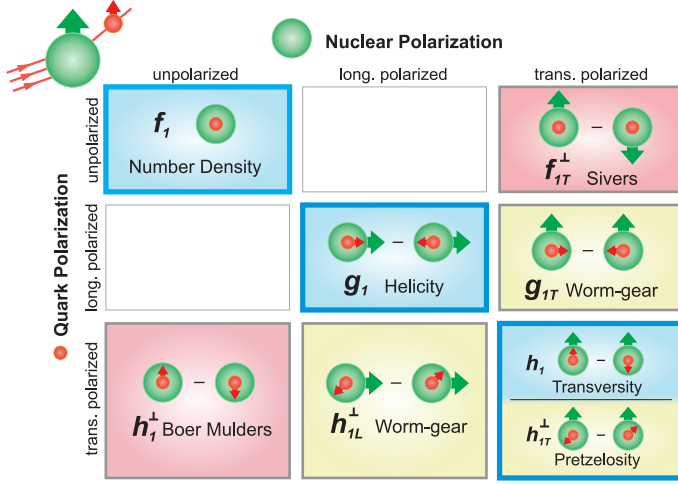


**Fig. 4.3** – Illustrated overview of the different parton distribution functions, sorted by the polarization of the nucleus and the interacting quark within. Redrawn after [61].

they are 'time-reversal odd' and the approach in the processes is contrary.

$$f_{1T}^\perp(DY) = -f_{1T}^\perp(SIDIS) \quad h_1^\perp(DY) = -h_1^\perp(SIDIS) \quad (4.2)$$

The transversity  $h_1(x)$  has a chiral-odd character and therefore, this function is only accessible in processes like SIDIS and DY, in which the chirality is flipped twice. Both processes are illustrated in Fig. 4.2 and share the fact that two hadrons and leptons are involved. In SIDIS, one hadron is in the initial as well as in the final state, whereas in DY, both hadrons are in the initial state. For this reason, DY has the advantage that fragmentation functions do not have to be considered, since only the lepton pair must be detected. The goal of these measurements is to confirm the universality of the TMD approach and in general, a test of the quantum chromodynamics [50]. This project demands some changes in the setup of the COMPASS experiment.

#### 4.3.2 Changes at COMPASS II

To fulfill the needs for the DY-measurements, several changes have to be made for both, the spectrometer and the target system. In Fig. 4.4, the absorber is pictured, which is placed between the target and the spectrometer to stop the unwanted hadrons, whereas the muons are able to pass almost unhindered. This procedure is necessary to reduce the high secondary particle flux and thus preventing the tracking detector from data saturation. The absorber is 236 cm long and consists of an aluminium-oxide body, surrounded by stainless steel and having a 140 cm long core of tungsten in the center, for stopping the primary non-interacting beam [62]. Therefore, the target-platform needs to be moved upstream by approximately 2.3 m, with all its pumping and supply lines. Due to multiple scattering within the absorber, the resolution of the tracking reconstruction is lower compared to SIDIS-measurements. This drawback is compensated by an additional vertex detector between the target and the absorber and by increasing the space between the target cells, for a better separation. In conjunction with this step, the number of target cells has changed back from three to two, with the consequence that the microwave cavity had to be readjusted. The target material is then packed into two cells, each 55 cm long and 4 cm

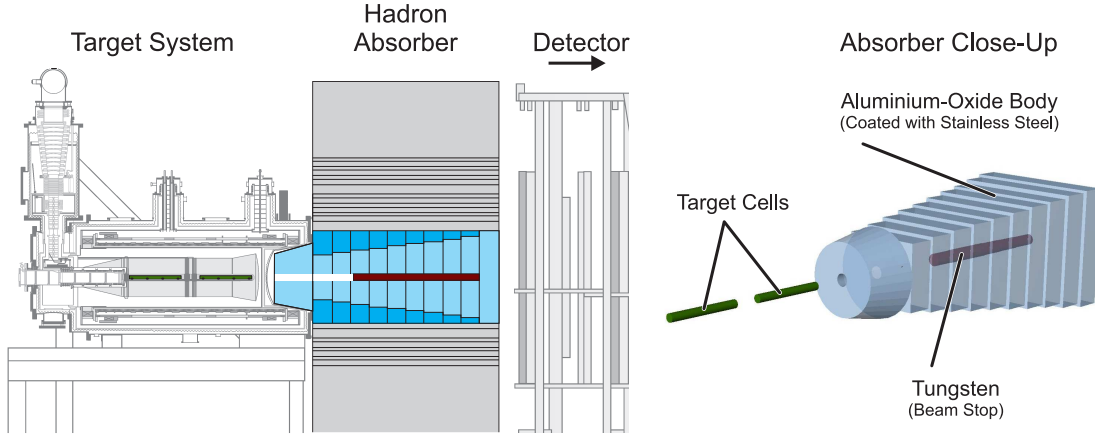


**Fig. 4.4** — Scheme of the hadron absorber for the DY-measurement at COMPASS II. The **left** figure shows the position of the absorber in respect to the target system and detector elements. In the **right**, the main part of the absorber is laid out, with the beam-stop plug and the aluminium-oxide body, together with the respective position of the target cells [49].

in diameter, separated by a 20 cm gap. The target cells itself were reconsidered, since the polyamid-net/Stycast<sup>7</sup> compound should be replaced through a rigid hydrogen-free material called PCTFE<sup>8</sup>, which is the topic of chapter 6. PCTFE should also have a higher radiation hardness, compared to the polyamid-net, which is important, since the beam is changed from leptons ( $\mu^+$ ) to hadrons ( $\pi^-$ ).

Due to a small cross section of the DY-process and a moderate beam intensity, a reasonable luminosity is only given with a thick target, in terms of interaction lengths. The pion beam flux is expected to be  $6 \times 10^8 \pi^-$  per spill<sup>9</sup>, whereas the previous muon-beam had only a maximum flux of  $4 \times 10^7 \mu^-$  per spill. More 'hadronizations' take place in DY and the secondarily produced particles lead to higher radiation within the immediate surrounding. For this reason, a number of precautions have to be applied in advance, technically and for safety, which will be discussed in the next section.

By changing the particle beam, further consequences are directly related to the polarized target, such as a local heating of the material through the beam as well as the total heat input in the dilution refrigerator. While the local heating can be controlled sufficiently by the beam focus and the bead size of the target material, a total heat input of 5 mW to 9 mW must be cooled away at beam rates of  $6 \times 10^7 \pi^-/s$  to  $10^8 \pi^-/s$ , respectively [57]. As a comparison, the muon beam caused a thermal load of 1 mW [63]. In Fig. 4.5, the temperature in the mixing chamber is plotted against the  $^3\text{He}$  flow rate, corresponding

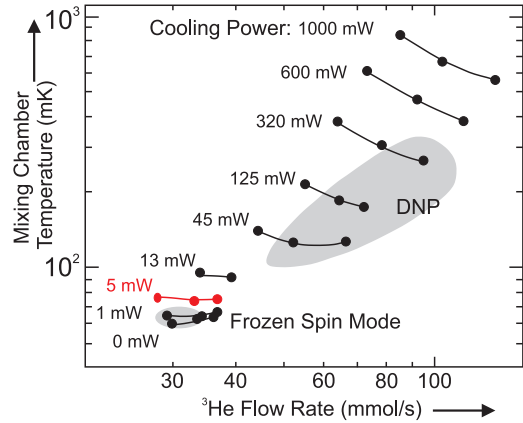


**Fig. 4.5** — Cooling power and mixing chamber temperature of the COMPASS refrigerator for different  $^3\text{He}$  flow-rates. The same amount of cooling power is at least needed for a specific heat load [63].

<sup>7</sup>Stycast is a two component epoxy glue, suitable for low temperatures and used for stiffening the net.

<sup>8</sup>PCTFE stands for Polychlorotrifluoroethene, CAS 9002-83-9.

<sup>9</sup>A spill is the effective extraction time of particles at the SPS, during a complete super-cycle. The spill-duration is 9.6 s, whereas the SPS super-cycle varied between 30-50 s, during the last years.

**Tab. 4.2** – Approved limitations by the CERN Radiation Protection Committee for COMPASS and the proposed beam properties for DY at COMPASS II [50].

	max. Particles at 190 GeV/c per Spill/SPS Super-Cycle		max. Nuclear Interaction Length
COMPASS	2 x 10 <sup>8</sup> Muons	9.6 s/16.8 s	–
	1 x 10 <sup>8</sup> Hadrons	9.6 s/16.8 s	5 %
<b>Proposed for the DY-Measurements:</b>			
COMPASS II	6 x 10 <sup>8</sup> Hadrons	9.6 s/48 s	considerable longer

to different cooling powers. In order to ensure a sufficient cooling, the flow rate must be raised, which then leads to a higher temperature within the mixing chamber. However the expected temperature to a heat load of 5 mW to 9 mW is still acceptable to maintain high nuclear polarization.

Also the radiation damage within the material has to be considered, which is produced through the pion beam. As it was already discussed in section 3.4, the maximum polarization degree suffers from a high radiation. In the past, it was not necessary to 'reset' the maximum polarization of the ammonia target through annealings, due to the muons as projectiles and a relative low intensity. Now with the high-intensity hadron beam, the radiation damage is expected to be much severe and a annealing during the experiment could be possible. However, all these effects may have a negative influence, whether on the maximum target polarization or the relaxation time.

## 4.4 Radiation Exposure during Drell-Yan

In 1999, the CERN Radiation Protection Committee set limitations for the beam operation with muons and hadrons, which are shown in Tab. 4.2. Another restriction is set for the nuclear interaction length of the hadron beam, which limits the amount of material in the beam line. But the proposal of COMPASS II provides a higher hadron flux with a longer duration time within the SPS and a 110 cm long target plus the additional hadron absorber right behind the target. Therefore, this setup requires a reconsideration to fulfill the specification of the Radiation Protection Committee. The group of A. MAGGIORA at CERN performed FLUKA-simulations<sup>10</sup> for the estimation of the radiation exposure during the DY-period [64, 65]. Simulations are done for both, the environment around the experiment and the immediate vicinity around the target material.

The main source of the ambient radiation will be the hadron absorber, right behind the polarized target, which stops the pion-beam completely. In order to reduce the radiation, the tungsten core and alumina body of the absorber is surrounded by 20 cm stainless steel as well as 40 cm thick concrete blocks. To lower the radiation in the DAQ<sup>11</sup>-barracks and

<sup>10</sup>FLUKA (FLUKtuierende KAskade) – a Monte Carlo simulation software for interactions of particles in matter.

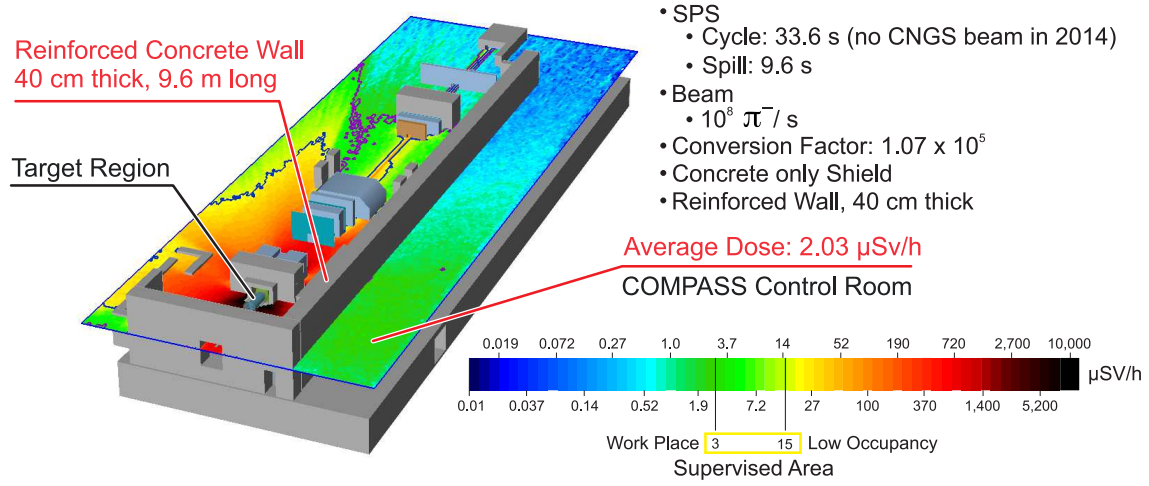


**Fig. 4.6** — Simulation of the ambient radiation dose of the COMPASS experimental hall, building 888. The simulation was done in the height of the COMPASS control center, in which the staff members usually work. In this area is also the location of the data acquisition system of the target system [64].

control room, the wall in-between is reinforced by an additional concrete wall, 9.6 m long and 40 cm thick. In Fig. 4.6, the simulation predicts an average dose of  $2.03 \mu\text{Sv/h}$  in the area of the DAQ-barracks and is in agreement with the safety limits of the CERN Radiation Protection Committee, of maximal  $3 \mu\text{Sv/h}$  for a supervised area and permanently work place [66]. Nevertheless, the decision was made to move the DAQ and the control room to another building<sup>12</sup> and establish a remote control interface, also for the target DAQ system [67]. But some electronics may be affected by the radiation, such as the NMR system [7] and the temperature sensors, since they cannot be outsourced.

Another issue is the radiation exposition of the target cells, which are directly hit by the beam. Figure 4.7 shows a close view of the accumulated dose for the target, with 180 days of data acquisition, a flux of  $10^8 \pi^- / \text{s}$  and a beam spot size with  $\sigma \leq 1 \text{ cm}$ . Also, significant positions of the target are plotted next to the simulation result. Noticeable is, that the highest radiation dose will appear very downstream of the target, due to the secondarily produced particles along the target. A maximum dose of 16 kGy is expected at a radius of 2 cm around the beam, whereas in the center the dose may reach 40 kGy.

On the target cell surface at  $r = 2 \text{ cm}$ , several temperature sensors are mounted for monitoring and they are directly exposed to the high radiation. An investigation of the radiation hardness of the sensors was done in collaboration with the group at the Jülich proton cyclotron and is discussed in chapter 7. So far, the cells were made out of a polyamid-net covered with a glue for the stiffening. The net ensures a minimal amount of matter for a sufficient cooling and prevents interference with scattered particles, but has also some drawbacks, which are discussed in chapter 6. It is not clear, whether the net with Styacast can withstand the radiation or not over the whole experimental period.

<sup>11</sup>DAQ stands for Data Acquisition.

<sup>12</sup>From the experimental hall 888 to building 892 (<https://maps.cern.ch/>).



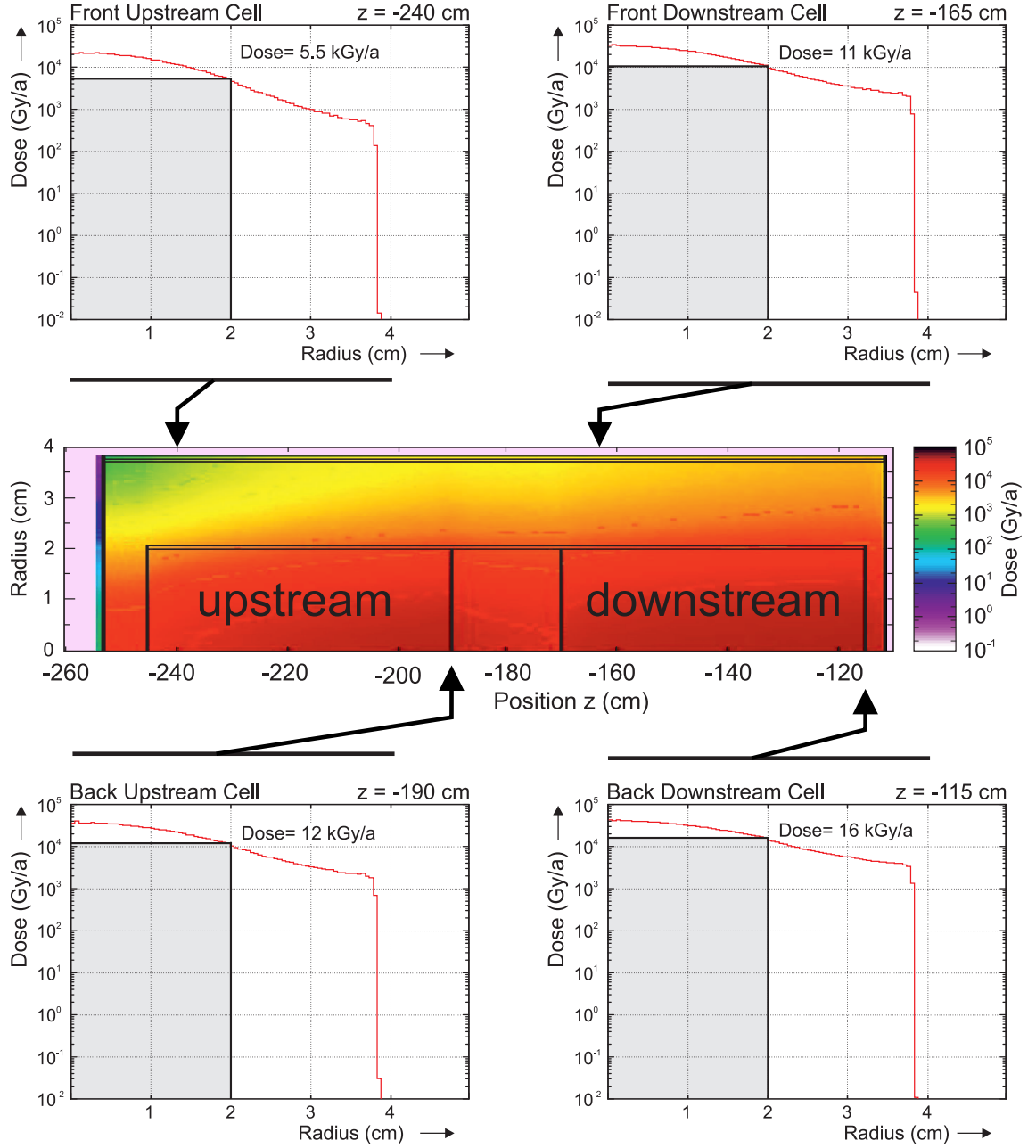


**Fig. 4.7** — Simulation of the expected radiation exposure in the immediate target region for the DY-measurement. The center picture illustrates the radiation dose over one half of the concentric target cells (4 cm in diameter). The pion beam comes from the left side. The four graphs around, are sectional views along the radius at the respective position. The wall of the cell is indicated at 2 cm, together with the expected radiation dose at this position [65].

Therefore, three other materials were considered as substitutes, which should tolerate ultra-low temperatures as well as having a high radiation resistance – FEP, PCTFE and Torlon<sup>13</sup>. Irradiation tests were performed at ELSA in Bonn and at the proton cyclotron in Jülich, in order to check the integrity of the material. In the end, PCTFE was chosen to replace the net and the assets and drawbacks are discussed in chapter 6, together with the new design of the target cells.

<sup>13</sup>FEP – Fluorinated Ethylene Propylene, Torlon – trademark name of Polyamide-imides.

### Summary

This chapter dealt with the past and future of the COMPASS experiment and motivates the subjects of this thesis. COMPASS and its predecessors were cutting-edge experiments on the question about the nucleon structure and kept its actuality through continual improvements and lastly by the approval of the of COMPASS II. To comply with the requirements for COMPASS II and the DY-measurements, changes in the detector setup and the target system had to be done, such as the integration of a hadron absorber and the reduction to two target cells. In the DY-process, the incident particle must be a hadron and as a consequence, the radiation level as well as the heat input in the refrigerator rises. The radiation may not only affect the target material and the containment, but also the electronics in the local environment, especially the temperature sensors.

## Behavior Studies of the Ammonia Target

This chapter deals with the characteristics of the new produced ammonia target, the build-up and the relaxation behavior. For 2011, a new ammonia target was needed, because the degree of polarization and the build-up time were not as good as before. In the experimental run of 2010, it took approximately 25 h to reach a polarization of 80 %. The material of this run was produced in 1995 and has already lost its purple color completely. In early publications, the intense color was associated not only with the irradiation itself, but also with the amount of the DNP-relevant radicals [47]. Instead, polarization and EPR measurements with pale ammonia have shown, that the color is not a guarantee for the dynamic polarizability of the ammonia target. The first section is going about the paramagnetic centers, with the main focus on the  $\dot{\text{N}}\text{H}_2$  and  $\dot{\text{H}}$  radicals and their concentrations. In the following paragraphs, the polarization behavior of the new ammonia is reviewed over a time span of about 4 years, at a magnetic field of 2.5 T and a temperature of 1 K. At this temperature and due to the drawback of a low power microwave source, a maximum polarization of only 4-6 % could be achieved, but nevertheless, relaxation and build-up curves were measurable. At lower temperatures and a reasonable higher microwave power, polarizations up to 90 % were reached at COMPASS in 2011, even in a shorter time than in 2010. A higher FOM-factor and a faster polarization build-up reduce the necessary time for an experiment at a given accuracy and thus, more attention can be paid to higher statistics.

### 5.1 Paramagnetic Centers

Since no chemical radical is added to ammonia, there is only a limited control over the produced defects during the irradiation. Not all defects have a paramagnetic character and are detectable in an EPR spectrometer. In a polarization experiment, only the paramagnetic electrons of the  $\dot{\text{N}}\text{H}_2$  radical are used in the DNP and thus, the magnetic field and the microwave frequency have to fulfill the resonance condition (2.14) for these electrons. Thereby, a typical magnetic field of 2.5 T corresponds to a microwave frequency of 70 GHz. However, the working point of a typical EPR spectrometer is around 330 mT and therefore, the microwave frequency has to be in the range of 10 GHz.

For this reason, the paramagnetic resonance is not taken at real DNP conditions. The resonance structure can be different from that at 2.5 T or higher, depending on the broadening mechanism [17]. Nevertheless, some useful information such as the signal width and the radical concentration can be obtained from these spectra, as described in section 2.3.2. The shape of the electronic resonance is mostly dominated by the structure of the radical and the setting of the unpaired electron within. For agents like DPPH<sup>1</sup> and trityl<sup>2</sup>, in which the unpaired electrons are well shielded, the resonance has almost the shape of the resonance of a free electron, see Fig. 5.1. On the contrary, TEMPO has an asymmetric shape, due to a coupling of the unpaired electron to the nitrogen atom (spin-1), a strong g-factor anisotropy and the fact, that all orientation of the radical are equally distributed [68], which is a result of the fast freezing process of the host material. The origin of the variable shape of the  $\dot{\text{N}}\text{H}_2$  resonance is mostly caused by the crystalline structure of solid ammonia. The unpaired electron in the ammonia radical  $\dot{\text{N}}\text{H}_2$  is also coupled to nitrogen and forms, all in all, nine possible transitions, which are all visible in the EPR-spectrum [69]. However, the resonance peaks are so close to each other, that they cannot be resolved and that is why the resonance of the  $\dot{\text{N}}\text{H}_2$  radicals looks so tangled, see Fig. 5.1. In contrast to TEMPO, the  $\dot{\text{N}}\text{H}_2$  radicals are embedded in a crystalline host structure and have a strong g-factor anisotropy. For this reason, the specific shape of the resonance depends on the orientation of the crystal within the magnetic field.

The purple color of ammonia started to fade out already after a few weeks, which can be seen in Fig. 5.2. After almost a year, the ammonia has lost its color completely and appears as transparent as before the irradiation. Nonetheless, the ability for DNP still remains, just like the material of 1995 demonstrated.

In the context of a advanced lab course in Bonn, a single crystal of the new produced ammonia target was frequently measured, supervised by S. RUNKEL over a time span of approximately 1 year and 8 month<sup>3</sup>, in order to track any property changes concerning the radicals. The crystal was sealed in a glass pipette and only fetched for the practical course, but with the precaution of keeping the crystal cooled at anytime. All EPR measurements

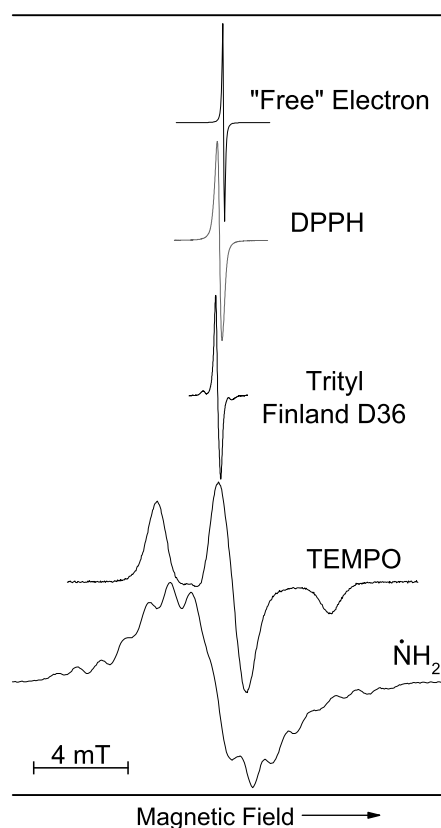


**Fig. 5.1** — Comparison of different X-band EPR-spectra. DPPH, Finland D36 and TEMPO are chemical additives, whereas  $\dot{\text{N}}\text{H}_2$  is a result of ionizing radiation. The 'free' electron serves only as a reference.

<sup>1</sup>DPPH is the short form of 2,2-Diphenyl-1-Picrylhydrazyl, CAS 1898-66-4.

<sup>2</sup>For example Finland D36 of the company GE Healthcare Bio-Science, with the structure formula  $\text{C}_{40}\text{H}_3\text{D}_{36}\text{O}_6\text{S}_{12}$ .

<sup>3</sup>The test series had ended, because the ammonia crystal was accidentally destroyed.

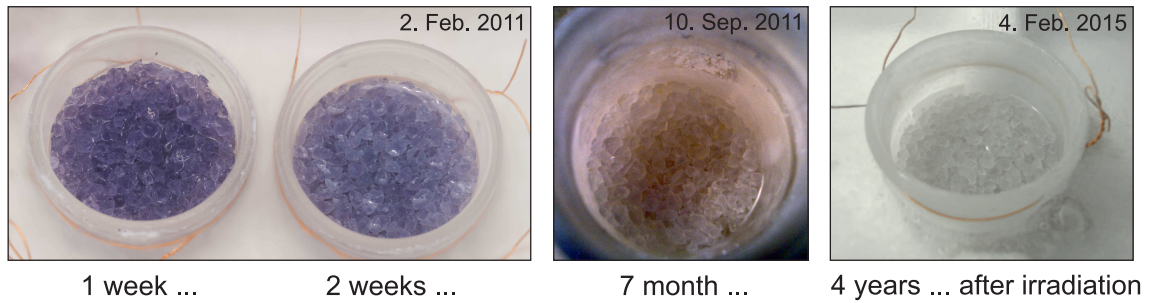


**Fig. 5.2** – Color decay of irradiated ammonia. Already 2 weeks after the irradiation, a slight fading of the purple color is visible.

were performed using the same parameters, but with different Dewar vessels<sup>4</sup>, which had an influence on the quality-factor of the measurement and thus, the resonance signals are not comparable to each other. To solve this issue, the resonance signal of DPPH is used, which was also measured in the lab course, in order to calibrate the magnetic field. Because DPPH is stable at room temperature, the intensity of the absorption signal should always be the same and does not change between the measurements, if the measuring parameters stay the same. In order to eliminate the influence of the Dewar vessels, correction factors were calculated for each ammonia measurement by normalizing the DPPH signals. In Fig. 5.3, the changes in the concentration of the paramagnetic centers are shown, as well as the ratio between the area of the  $\dot{\text{H}}$  and  $\dot{\text{N}}\text{H}_2$  resonance.

Figure 5.3a shows the area of the integrated absorption signal of the  $\dot{\text{N}}\text{H}_2$  resonance against the time after the irradiation. The area is proportional to the concentration of the respective paramagnetic centers, as explained before in section 2.3.2. Already a few weeks after the irradiation, the area under the  $\dot{\text{N}}\text{H}_2$  resonance decreases significantly, but stabilizes in the later measurements. This behavior corresponds to the previously mentioned color decay of ammonia and thus, the F-centers (section 3.3.2). The resonance of this F-center electrons should be at the position of an almost 'free' electron, but the signal of the  $\dot{\text{N}}\text{H}_2$  radicals is at this very same position and covers the F-centers. An extraction of the F-center resonance is difficult to realize, because the crystalline structure, in combination with the g-factor anisotropy, is creating different signal shapes, depending on the orientation of the crystal in the magnetic field. This parameter cannot be adjusted in the measurement. In the thesis of J. HARMSSEN [15], such an extraction succeeded, but with irradiated deuterated butanol, which has an amorphous structure and all molecule orientations are equally distributed. So, the shape of the resonance signal is independent of the position of the sample in the magnetic field. However, the loss in Fig. 5.3a could be caused by the F-center decay, whereas the concentration of the  $\dot{\text{N}}\text{H}_2$  radicals is more or less stable. At least the material of 1995 has shown, that the  $\dot{\text{N}}\text{H}_2$  is stable over a long time.

The situation for the atomic hydrogen in ammonia is quite different, see Fig. 5.3b. Here, the concentration shows a clear tendency to fall. The position of the  $\dot{\text{H}}$  resonances is dominated by the hyperfine interaction between electron and proton of the hydrogen atom and for this reason, the resonances appear aside from the position of a 'free' electron.

<sup>4</sup>The Dewar vessels are used to keep the samples at a temperature of 77 K, using liquid nitrogen.

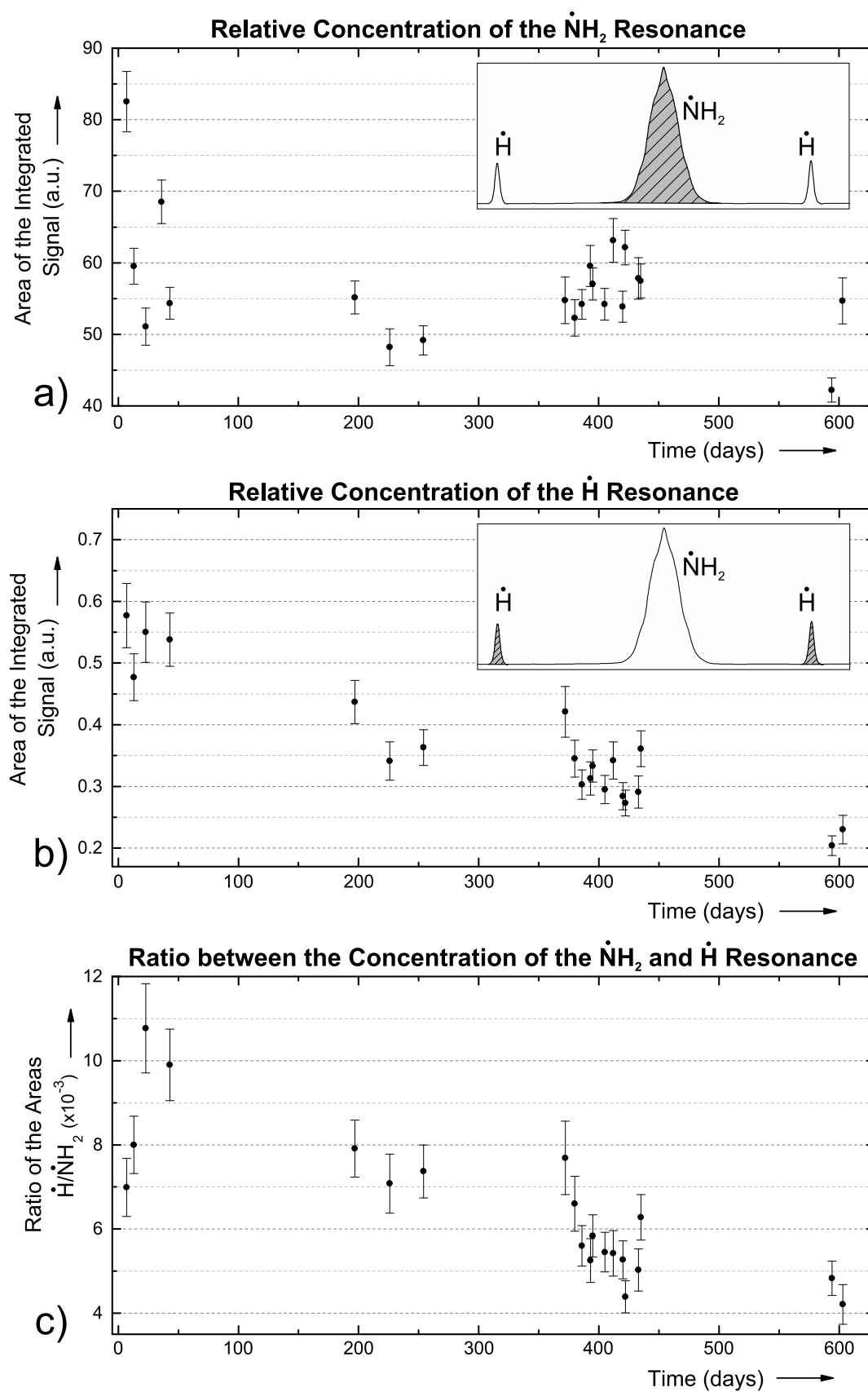


**Fig. 5.3** — Changes of the paramagnetic properties of irradiated ammonia against the time after the irradiation. **a)** The area under the  $\dot{\text{N}}\text{H}_2$  resonance, which is proportional to its concentration. **b)** The area of the  $\dot{\text{H}}$  resonances next to the ammonia radical. **c)** The ratio of the both quantities  $\dot{\text{H}}/\dot{\text{N}}\text{H}_2$ . The intensities of the  $\dot{\text{H}}$  resonances in the overview layers are amplified, just for visualization.

Therefore, the g-factor and hence, the Larmor-frequency is shifted so much, that these centers do not actively participate in the DNP process. But, which role the  $\dot{\text{H}}$  radicals may play in the target polarization anyhow, is discussed in the next section.

In Fig. 5.3c, the ratio between the  $\dot{\text{H}}$  concentration and  $\dot{\text{N}}\text{H}_2$  increases in the first moment, due to the fast drop of the assumed  $\dot{\text{N}}\text{H}_2$  concentration, but falls like the  $\dot{\text{H}}$  concentration, afterward. This behavior shows, that the paramagnetic hydrogen does not recombine with the  $\dot{\text{N}}\text{H}_2$  radicals. Otherwise, both concentrations would be equally decrease and the ratio would remain constant. Therefore, the paramagnetic hydrogen is eliminated either through recombination into molecular hydrogen  $\text{H}_2$  or it diffuses out of the material. At least, a lower  $\dot{\text{H}}$  concentration should minimize the probability, that the  $\dot{\text{N}}\text{H}_2$  radicals can recombine.

Figure 5.4 shows the absolute radical concentration versus the time after the irradiation. To estimate the concentration of the paramagnetic centers in ammonia, first a calibration sample of butanol with the TEMPO radical had to be prepared (section 2.3.2). Despite the few data points, a major drop to about half of its initial value can be seen in the first year after the irradiation. Of course, this behavior is related to Fig. 5.3a, but it cannot be said exactly, how much the F-centers are involved in the decrease of the concentration of the  $\dot{\text{N}}\text{H}_2$  resonance. It can also be seen, that after the fall, the concentration remains

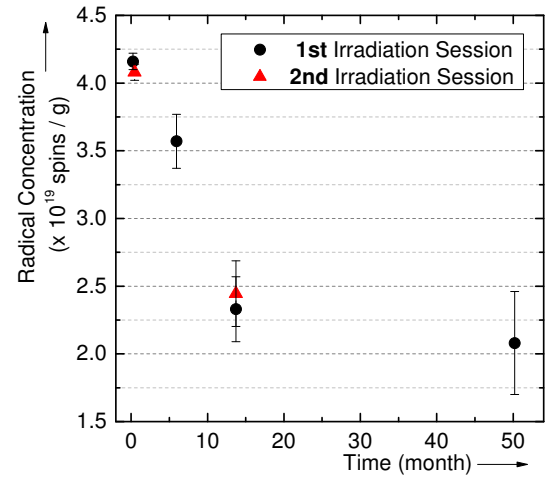


**Fig. 5.4** — Absolute radical concentration versus time after irradiation for the fresh material of 2011.

fairly constant, considering the last two points. The material for the estimation of the radical concentration was taken from the first of nine irradiation sessions (section 3.3.2), the same reservoir as for the following polarization measurements. This material was frequently taken from the storage Dewar and thus, there was always a risk of overheating the material, accidentally. In Fig. 5.4, there is also a concentration measurement of the second irradiation session, which was held in storage until then. The estimated value is very close to that of the first irradiation session and so, a variation due to a brief overheating can almost be ruled out.

In which way the changes in the electronic paramagnetic regime affects the polarization behavior is studied in the next section.

## 5.2 Polarization Measurements in Bochum

The following polarization measurements were performed at the Bochum target laboratory, which provides magnetic fields up to 7 T and temperatures down to 120 mK. Due to the extremely long relaxation times of several thousand hours in ammonia, at ultra-low temperatures, all measurements were done at 1 K and 2.5 T. For this reason and the fact that the maximum output of the microwave power does not exceed 100 mW, nuclear

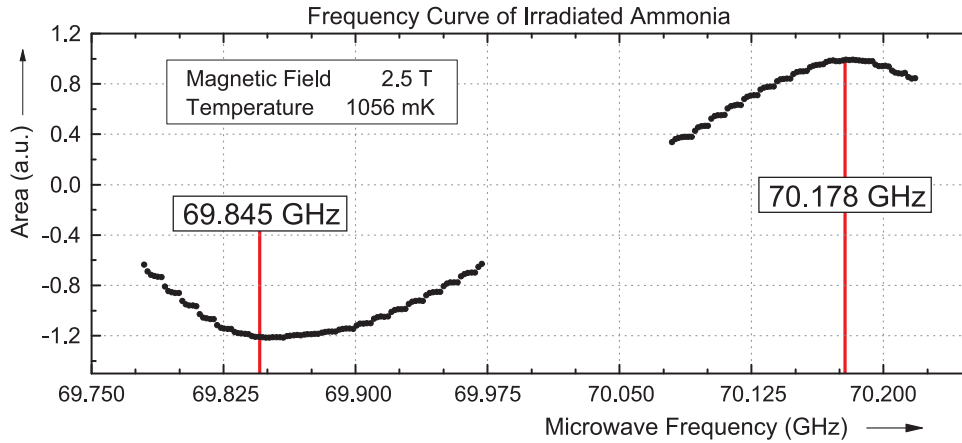


**Fig. 5.5** — Frequency curve of irradiated ammonia at 2.5 T and 1056 mK. The best polarization frequencies can be read off the extreme points of the curve. At the lower frequency, the target become positive polarized, whereas the higher frequency provides negative polarization. The y-axis shows the integrated area, not the polarization.

polarizations of only 4-6 % could be achieved. For each measurement, approximately  $1.7 \text{ cm}^3$  of the target material was removed from the storage Dewar and returned after the measurement was done. Attention was required during the loading, that the ammonia beads were sufficiently cooled over the whole time. Nevertheless, there is no absolute assurance, since no sensor logs the temperature of the ammonia during loading. Critical situations are the removal out of the storage Dewar and the soldering of the NMR coil, while the material is already filled in the sample holder. Previous measurements have shown, that a heating up to 113 K is without consequences for the  $\dot{\text{N}}\text{H}_2$  radicals [21]. However, this may be hastened up the decay of the F-centers.

The following sections describe the polarization and relaxation behavior of the fresh ammonia target and they are compared to that of the previous produced material of 1995.

### 5.2.1 Polarization and Relaxation Behavior

At first the optimal microwave frequencies have to be found, for positive and negative polarization. To do this, a frequency curve is measured, in which the microwave frequency is swept in defined steps over the interesting range. Figure 5.5 shows such a frequency curve, with the optimal frequencies at its extreme points. These numbers are good as starting points and only small corrections to higher or lower frequencies are necessary for an optimization. These frequencies were found to be

$$\nu_+ = 69.845 \text{ GHz} \quad \nu_- = 70.178 \text{ GHz} \quad (5.1)$$

for positive and negative polarization at 2.5 T, with a gap of 333 MHz. These values strongly depend on the precise magnetic field strength.

In section 2.2.2, two polarization mechanisms are compared to each other, with their consequences for the polarization frequencies. A comparison of the measured frequency curve with Fig. 2.7, reveals more similarity to the DSSE and less to a pure SSE. Like mentioned in section 3.2, the polarization mechanism can be described best through the EST, but at high nuclear polarizations, the measured nitrogen-to-hydrogen polarization



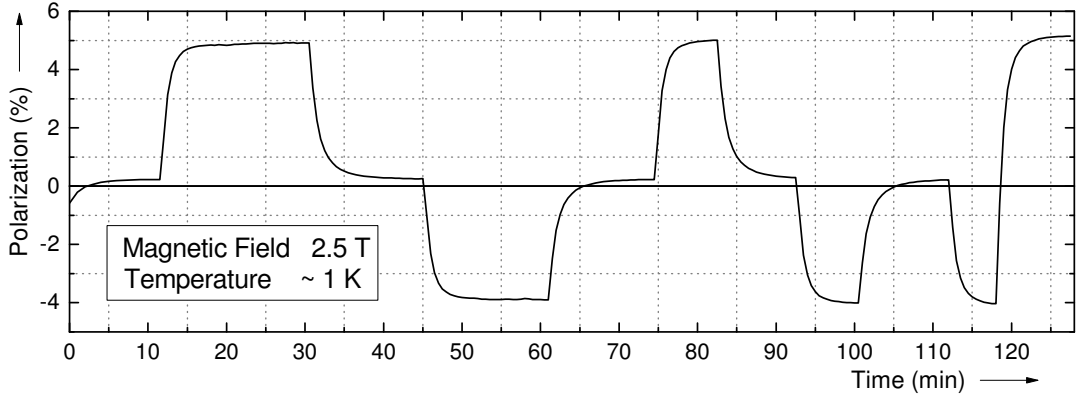
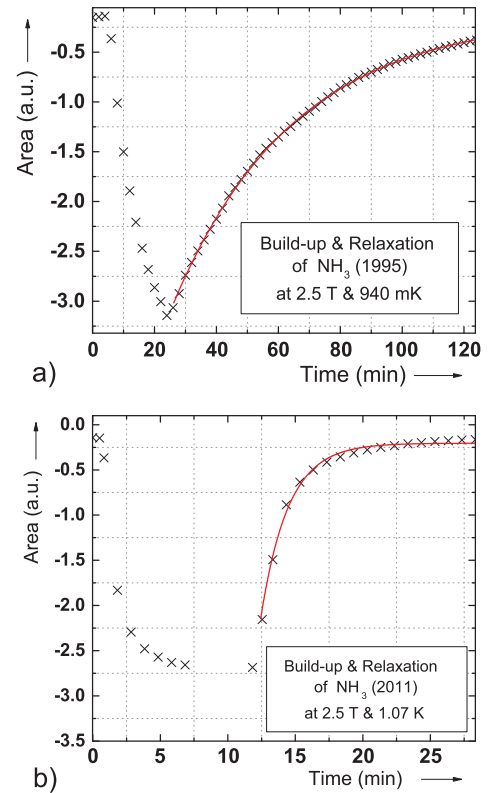


**Fig. 5.6** — A typical cycle of a relaxation measurement.

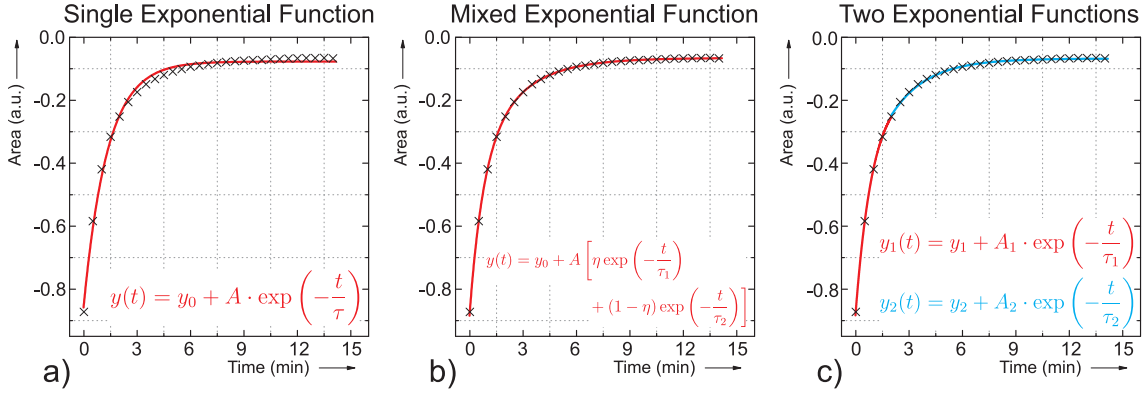
differs slightly from the EST prediction (Fig. 3.3). For these deviations, an influence of the DSSE is held responsible, at higher polarization [39].

Figure 5.6 shows a typical measurement cycle of several consecutive polarization build-ups and relaxations and at first glance, it is noticeable that the material reacts very fast. Only a few days after the irradiation, the measurements yielded relaxation times, which are less than one minute, see Fig. 5.7b, and build-up times of approximately 10 minutes at 2.5 T and 1 K. In 1983, the measurements of fresh ammonia showed relaxation times, which were considerably longer, 8 min to 25 min at the same external conditions and for radical concentrations of  $1.5 \times 10^{20}$  spins/g and  $5.1 \times 10^{19}$  spins/g, respectively [47]. But these concentrations resulted from a comparison to the relaxation time of a gauge sample, with a known radical concentration, like it is described at the end of section 3.3.2. Therefore, these values must be treated with caution. Figure 5.7a shows the polarization build-up and relaxation of the 1995 material, which was polarized 16 years after its irradiation. Although, the EPR measurements have shown similar radical concentrations (3.4, 3.5), considerable longer relaxation times of 17 min to 50 min between a temperature of 1170 mK to 870 mK were observed.

In earlier measurements of the 1980s [47], a peculiar shape of the hydrogen relaxation was already noticed and this behavior also occurs with the new material of 2011. While the build-up curve can be fitted very well with a single exponential function, this possibility fails by describing the relaxation, see Fig. 5.7b. As a solution, two exponential functions are used, one for a fast and another for a slow relaxation. This behavior is even visible



**Fig. 5.7** — Build-up and relaxation of the 'old' and 'new' ammonia. Both measured in 2010 and 2011. The red curve represents an exponential fit. The ordinate values between a) and b) are not related to each other.



**Fig. 5.8** — Comparison between the relaxation fit functions. The same relaxation curve is fitted by three different approaches, a single exponential function, a mixed exponential function with a mixing parameter  $\eta$  and two separate exponential functions.

at the relaxation of the 1995 material, but much weaker. So the relaxation of the older material can be described sufficiently enough through a single exponential fit.

Here, the attempt is made to describe the relaxation behavior in three different ways, but each with exponential functions. At first with a single function, then with two separated and with a mixture of two exponential functions. The latter way comes with a mixing parameter  $\eta$  and the whole function can be parametrized as.

$$y(t) = y_0 + A \left[ \eta \exp\left(-\frac{t-t_0}{\tau_1}\right) + (1-\eta) \exp\left(-\frac{t-t_0}{\tau_2}\right) \right] \quad (5.2)$$

Whereat, the mixing parameter  $\eta$  can take values between 0 and 1 and thus, one exponential function may be weighted over the other. For a quick analysis, a LabView program was written (Fig. A.1), in which the polarization trend of a complete measurement cycle can be imported. Afterward, each relaxation curve is extracted and then analyzed with all three methods, one after another. In Fig. 5.8, the same relaxation curve is plotted with all three fitting methods and the best result is yielded by the mixed function of (5.2).

For the fitting method with two separate functions, the point is crucial, at which the data-set is split between the two exponential functions. Usually, only a few data points are left, to describe the fast relaxation. The cause for this relaxation behavior is not clear yet, but apparently, more than just one relaxation process takes place and an overlap of these processes is leading to the observed behavior. How many of these relaxation channels are existing is unknown, but the fit with two mixed exponential function works very well. Therefore, at least two processes should exist, which are dominating the nuclear relaxation of hydrogen.

First of all, the hydrogen in irradiated ammonia can be distinguished into three sorts, which mainly differ in their bonds and surroundings. The hydrogen of the ammonia molecule  $\text{NH}_3$ , the ammonia radical  $\dot{\text{N}}\text{H}_2$  and the trapped atomic hydrogen  $\dot{\text{H}}$ . Two of these cases have a paramagnetic character, due to their unpaired electron, which is already known from section 5.1. In the EPR-spectrum of irradiated ammonia, the resonance of atomic hydrogen is clearly visible on both sides next to the  $\dot{\text{N}}\text{H}_2$  resonance (Fig. 3.4). Due to hyperfine interaction, the g-factor of these electrons is shifted so far, that their

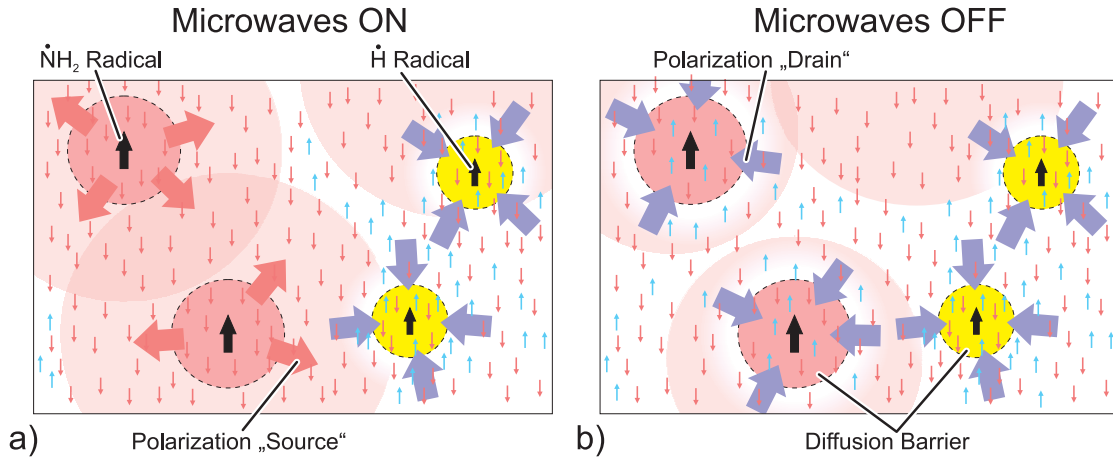


**Fig. 5.9** — Artistic illustration of the polarization behavior in irradiated ammonia, with two different paramagnetic centers. **a)** If the microwaves are on ( $\sim 70$  GHz), the  $\dot{\text{N}}\text{H}_2$  radicals work as polarization sources, whereas the  $\dot{\text{H}}$  radicals as polarization drains. **b)** If the microwaves are off, both centers work as polarization drains.

Larmor-frequencies are not close to the usual frequency of 70 GHz, at a magnetic field of 2.5 T. Nevertheless, the unpaired electrons of  $\dot{\text{H}}$  are also almost completely polarized, as those of the  $\dot{\text{N}}\text{H}_2$  radical. Now, all these paramagnetic electrons shift the Larmor-frequencies of the nuclei in their close vicinity, caused through the local field of the electrons. For this reason, the hydrogen atoms of these radicals are not measurable, since they appear out of range of the typical NMR-window. Like already mentioned in section 2.2.2 concerning spin-diffusion, a diffusion barrier is established around each paramagnetic electron. With that, two different diffusion barriers can be identified, which may behave differently. The barrier of the  $\dot{\text{N}}\text{H}_2$  radical acts as a source for polarization during the microwave irradiation, but as a polarization drain, if the microwaves are turned off. In contrast to that, the hydrogen radical  $\dot{\text{H}}$  works as a polarization drain, regardless whether the microwave irradiation is on or off. With different relaxation rates of these drains, the observed behavior could be explained. Figure 5.9 tries to illustrate both of these cases. A possible explanation why the material of 1995 is less affected, would be the lower concentration of the  $\dot{\text{H}}$  radicals, see Fig. 5.10, and also in the EPR long-term measurement (Fig. 5.3b), the trend is visible. The assumption can be made, that the relaxation behavior is described better by a single exponential function, if the material becomes older and thus, contains less  $\dot{\text{H}}$  radicals. This fact is being investigated along with the long-term relaxation in the next section. One paramagnetic center was still left out so far and these are the F-centers. The resonance

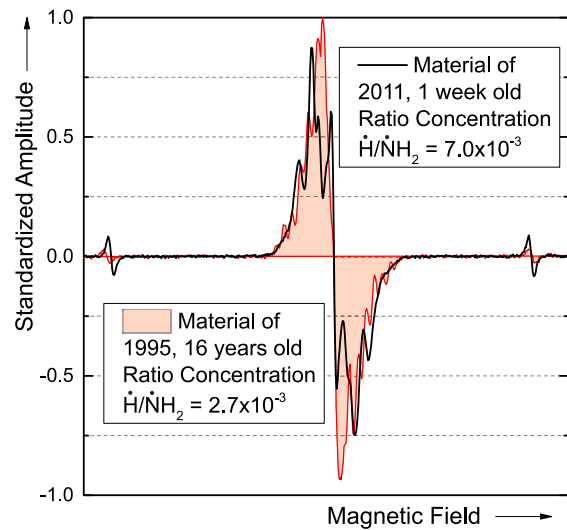


**Fig. 5.10** — Comparison of the EPR-spectra between 1995 and 2011. The area under the  $\dot{\text{N}}\text{H}_2$  resonance of both spectra was normalized, so that the difference in the ratio between the  $\dot{\text{H}}$  and  $\dot{\text{N}}\text{H}_2$  concentration can be seen.

of this electron should be at the position of an almost 'free' electron and thus, could also be used in the DNP process. But, due to the relative fast fading of the purple color in one year, these centers are playing a role, only shortly after the irradiation or if the experiment beam produces new radicals.

### 5.2.2 Long-Term Behavior

The polarization and relaxation behavior of ammonia was observed during the 4 years after its irradiation and analyzed through methods, which are described in the previous section. All measurements were performed at the same external conditions of 2.5 T and  $(1.0 \pm 0.1)$  K. The long-term evolution of the polarization build-up shows the evidence of an increasing build-up time, see Fig. 5.11. Most of the changes happen shortly after the irradiation and after 12-15 month, the spreading of the data points becomes too grave, as to give any clear statement of its progression. This first period corresponds to the color fading of the material, which has almost lost its purple color after the first year (Fig. 5.2). Besides, the timeline of this behavior goes along with the observation of the radicals in section 5.1. With the F-centers, more DNP-active centers are available, shortly after the irradiation, however, they seem not to be stable when stored under liquid nitrogen.

As for the relaxation, all three methods are tending to longer relaxation times, with increasing time after the irradiation, see Fig. 5.12. Unfortunately, the data points are scattered over a large scale and therefore, an exact prediction of the behavior cannot be given. For the relaxation, either a global preference in positive or negative direction could be found and for this reason, each data point represents the average relaxation time of the corresponding measurement.

Figure 5.12a shows the changes of the relaxation, described by a single exponential function. Only a few days after the irradiation, a relaxation time of approximately 1 min could be measured. Almost 4 years after the irradiation, the relaxation time has doubled to  $\sim 2$  min. However, the extension of the relaxation time is only visible in the first year, from then on, no tendency can be seen anymore.

In Fig. 5.12b, the same relaxation curves are plotted against the time after irradiation, but now fitted with two mixed exponential functions, as given in (5.2). Even though this function reproduces the polarization decay very well, the mixing parameter  $\eta$  shows no clear pattern of behavior, and varies between 0.4 and 0.8, see Fig. 5.13. The expectation would have been a steady shift to higher or lower values, which would illustrate an overcome of one relaxation channel over the other. For instance, the decrease of the  $\dot{H}$  radicals

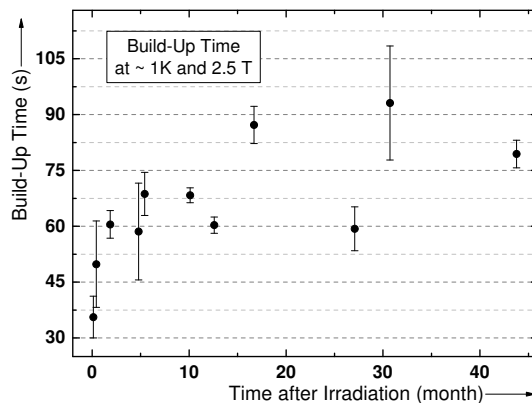
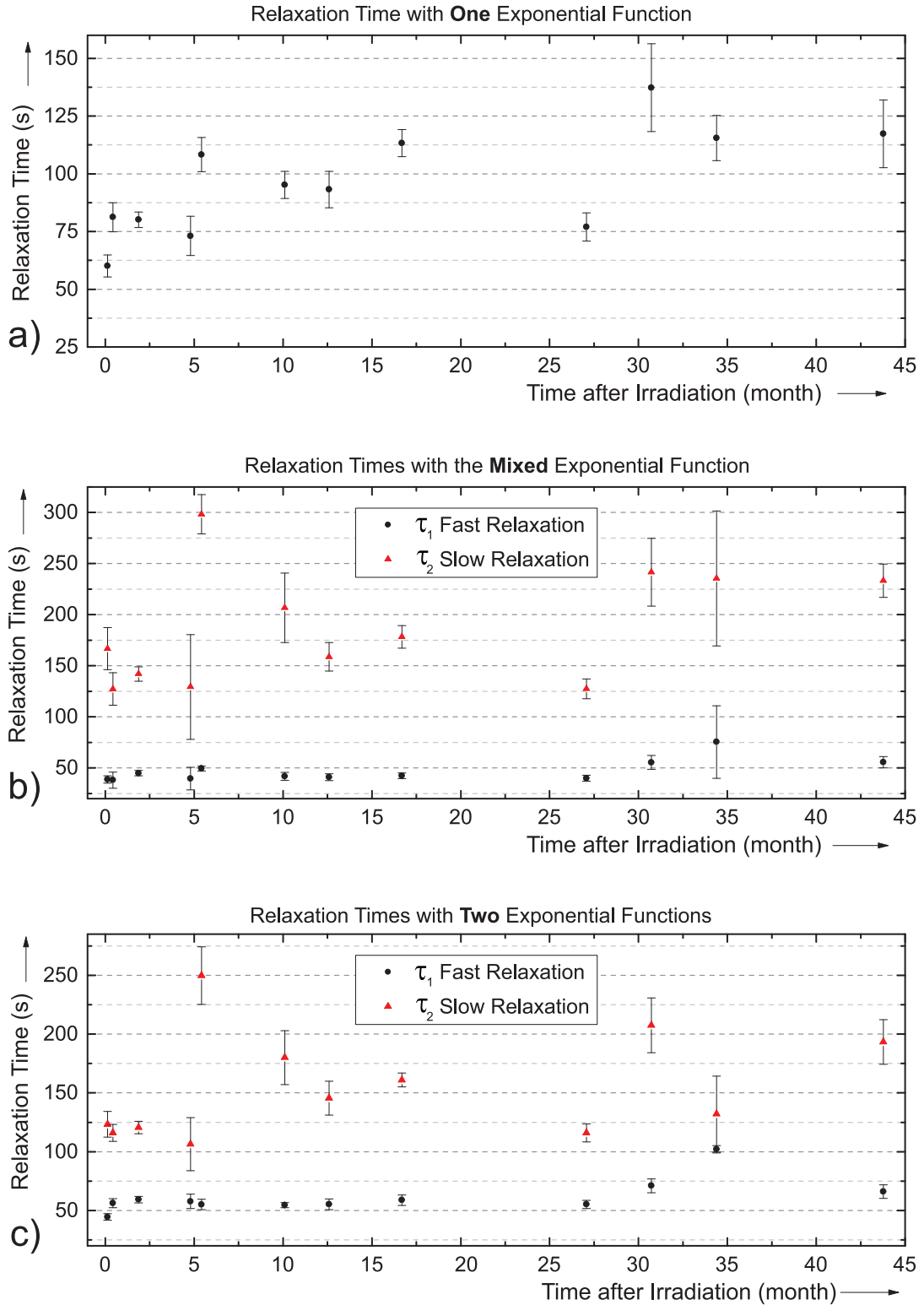


Fig. 5.11 – Long-term behavior of the build-up time of irradiated ammonia.



**Fig. 5.12** — Long-term relaxation measurement of ammonia. The same relaxation curves are fitted by three different methods. The letter numbering corresponds to Fig. 5.8, in which all three fitting methods are demonstrated.

(Fig. 5.3b), as a possible relaxation channel, should have an influence on this parameter. However, the mixing parameter  $\eta$  has of course an influence on the obtained relaxation times from the fit and for this matter, an average  $\bar{\eta}$  of 0.53 was calculated. In this picture, both relaxation channels contribute merely equally to the total relaxation and  $\bar{\eta}$  was fixed

through the further fitting process. The interpretation of the results with the mixed function is still more difficult, compared to the first method in Fig. 5.12a. While the 'fast' relaxation stays more or less around 50 s, the 'slow' relaxation varies between 100 s and 250 s, without a trend. The third way in Fig. 5.12c describes the relaxation through two separate exponential functions. The conclusion is quite the same as for the mixed function. In direct comparison to Fig. 5.12b, the estimated times slightly differ, but their behavior among each other is the same.

Finally, a small new insight was obtained on the long-term behavior of irradiated ammonia as a target material. Apparently, the purple color of ammonia is not the main reason for the DNP ability, but there is some evidence, that the F-centers may be involved in the polarization process. The evolution of the build-up and relaxation times (1st order) coincide with the fading of the purple color. Most of the changes appear in the first year after the irradiation, but from then on, the polarization properties are more or less steady. A change of the peculiar relaxation into a more like 'single-exponential' behavior, as it was predicted in the last section, was not observed. But, the sample of 1995 had shown, that the material can be polarized even after over a decade, stored in liquid nitrogen.

For a moment, a maximum polarization result of about 6 % does not point out irradiated ammonia as a 'good' target. In contrast, early measurements in the 1980s yielded polarization degrees of about 40 %, at the same external conditions (Fig. 3.10), but with a much stronger microwave source. However, even a value of 40 % is not sufficient for a scattering experiment, but by reducing the temperature into the millikelvin range, the nuclear relaxation times are increased to several thousands of hours. At these conditions, final polarizations of more than 90 % are possible, and the polarization is resting in the frozen-spin-mode. Even after a reduction of the magnetic field to a lower 'holding field' ( $\sim 0.6$  T), the high polarization still remains, like at COMPASS with a temperature of about 60 mK. In the next section, the behavior of the fresh material at the COMPASS experiment is made the subject of discussion.

### 5.3 Polarization Measurements at COMPASS

Chapter 4 reports on the history of COMPASS, along with its predecessors EMC and SMC, and ammonia was always a part of it. It can be seen from Tab. 4.1, that in the year 2007 and 2010 ammonia was used as a target material, which was produced in 1995. In Fig. 5.14, build-up curves of 2007 and 2010 are shown. The relevant information of this charts are the maximum polarization and the build-up time, which corresponds to the time, which is lost for the data acquisition of the experiment. Since the relaxation times

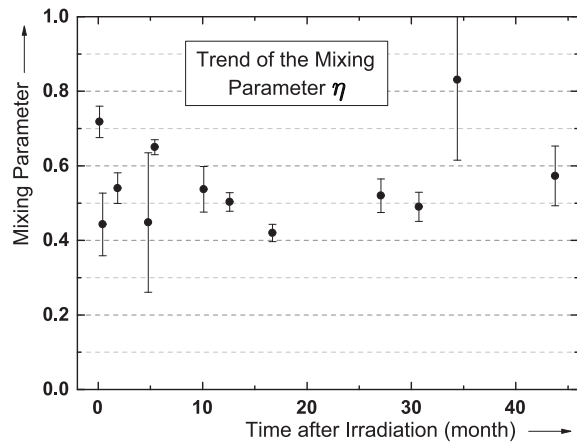


**Fig. 5.13** – Trend of the mixing parameter  $\eta$ . The average  $\bar{\eta}$  was found to be 0.53.

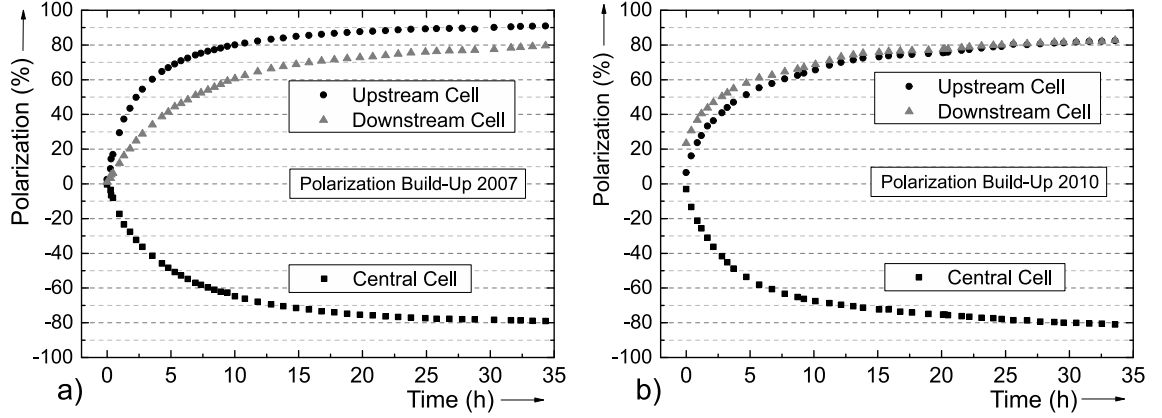


**Fig. 5.14** – Build-up curves of the  $\text{NH}_3$  polarization at COMPASS for 2007 and 2010 [59].

lie in the order of thousand hours, the polarization decays only slow. In the appendix A.3, overviews of the complete polarization runs of 2007, 2010 and 2011 are given.

In 2007, an average polarization of 84% were maintained in the longitudinal and transversal operating mode<sup>5</sup>. Experience has shown, that the down-cell generally reaches a lower polarization, in which a temperature gradient along the entire target is held responsible for. Since only 70 GHz diodes are available at COMPASS, the target must be polarized at 2.5 T in the longitudinal mode. For the transverse mode the field is rotated (section 4.2), after the temperature is low enough to lock the polarization into the frozen-spin-mode. Build-up times of around 20 h were needed to reach a polarization of 80%, which costs more than a day to raise the polarization to its maximum value. In this case, a characteristic time cannot be calculated, due to a shift in the optimal microwave frequency. As a result, the build-up curves do not show a clean exponential behavior through the entire polarization process. In the next section, this relationship is explained in detail.

But once, the polarization caught up to its maximum value, a sufficient high polarization degree lasted for several days. For the run in 2007, a rough estimation of the relaxation times leads to  $\sim 9000$  h for the longitudinal mode and  $\sim 4000$  h for the transverse mode. In 2010, the target was operated only in the transverse mode and the average polarization was lower and moved around 80%. But this was more a strategy of the COMPASS collaboration, in which less time was spared for the polarization build-up, in combination with frequent repolarizations, instead of spending more time on reaching the maximum polarization<sup>6</sup>. In contrast to the transverse mode in 2007, the relaxation times were a bit longer and estimated to  $\sim 5000$  h. However, the polarization build-up times were similar to those of 2007 and lay around 25 h to reach 80%. Due to the transverse mode, the polarization was held at 0.6 T and thus, the target could not be polarized continuously and had to rebuild nearly every 10 days. All important polarization results of the years 2007, 2010 and 2011 are summarized in Tab. 5.1.

A rather low average polarization of 80% and a long build-up time, which costs nearly two days, diminish the quality of the target and thus, the statistics for the

<sup>5</sup>For the longitudinal polarization the 2.5 T solenoid magnet was used, whereas the transverse polarization was realized through the dipole magnets, with a maximum field of 0.6 T.

<sup>6</sup>Private Communication with K. HORIKAWA KONDO (Yamagata University).

experiment. As already mentioned several times, this loss was the major motivation for the production of the new material and was finished in March 2011. In the last two production runs, the samples were destroyed as a consequence of explosions within the refrigerator and in the end, also the irradiation refrigerator itself was destroyed<sup>7</sup>. Nevertheless, the amount of the produced material was almost sufficient for the three target cells and only 50 mL were missing, which were then replaced with the older material of 1995. In order to minimize any possible discrepancy in the scattering experiment, the extra amount was put in the front of the upstream cell, because an interference is least expected at this position.

In order to install the target, the pre-cooled refrigerator had to be warmed-up before the target holder can be removed. The raise in temperature should reduce the amount of humidity, which may slip into the refrigerator during opening. Afterward, the entry of the refrigerator was sealed with a blank flange. During filling of the material into the cells, the ammonia beads must always be kept cooled and even when the holder is inserted into the refrigerator, the temperature must not exceed the limit at which the  $\dot{\text{N}}\text{H}_2$  radicals decay. Figure 5.15 shows the temperature variation in the mixing chamber over the entire loading procedure, including prominent positions, in which the refrigerator was opened. The temperature was logged with the sensor TTH8, which is suitable for the region above 1 K. The position of the sensor is mapped in Fig. 4.1 and is described in detail in chapter 7, together with the other sensors. Based on the graph, it can be seen, that the temperature in the mixing chamber was never higher than 95 K. After loading, the temperature was lowered again and the TE-calibration could be started<sup>8</sup>. For the TE-calibration, the resonance signal along the target cell is measured at three different temperatures around 1.5 K, 1.3 K and 1.0 K and the polarization at TE is calculated for these parameters, using (2.19). As already mentioned at the end of section 2.3.1, calibration factors are generated, which are used to determine the polarization of the dynamically enhanced signal. But there exists

**Tab. 5.1** — Polarization results of ammonia at COMPASS for 2007, 2010 and 2011. The data and values are taken from different sources [57, 70, 59]. The average polarization of each year is estimated from the complete data set of an experimental period (Fig. A.2 – Fig. A.4).

<b>2007</b> (material of 1995)	
avg. Polarization	( $84.2 \pm 4.6$ ) % ( $-84.5 \pm 4.6$ ) %
max. Polarization	~95 %
Build-Up Time*	22.8 h
Relaxation Rate**	0.4 – 0.6 % /day
◦ Long.	~9000 h
◦ Trans.	~4000 h
<b>2010</b> (material of 1995)	
avg. Polarization	( $80.9 \pm 2.4$ ) % ( $-79.5 \pm 3.5$ ) %
max. Polarization	~86 %
Build-Up Time*	25.6 h
Relaxation Rate**	0.3 – 0.4 % /day
◦ Trans.	~5000 h
<b>2011</b> (material of 2011)	
avg. Polarization	( $85.0 \pm 2.4$ ) % ( $-84.2 \pm 3.1$ ) %
max. Polarization	~91 %
Build-Up Time*	13.7 h
Relaxation Rate**	~0.12 % /day
◦ Long.	~8000 h (+) ~4000 h (–)

\* Up to an average polarization of 80 %.

\*\* The relaxation times are only rough estimations.

+ positive, – negative

<sup>7</sup>An explosion was triggered by nitrogen, which entered the argon circuit through a cryo-leak in the heat exchanger. This hazard was already mentioned in section 3.3.2.

<sup>8</sup>It is also possible to measure the TE-polarization after the experiment is over.



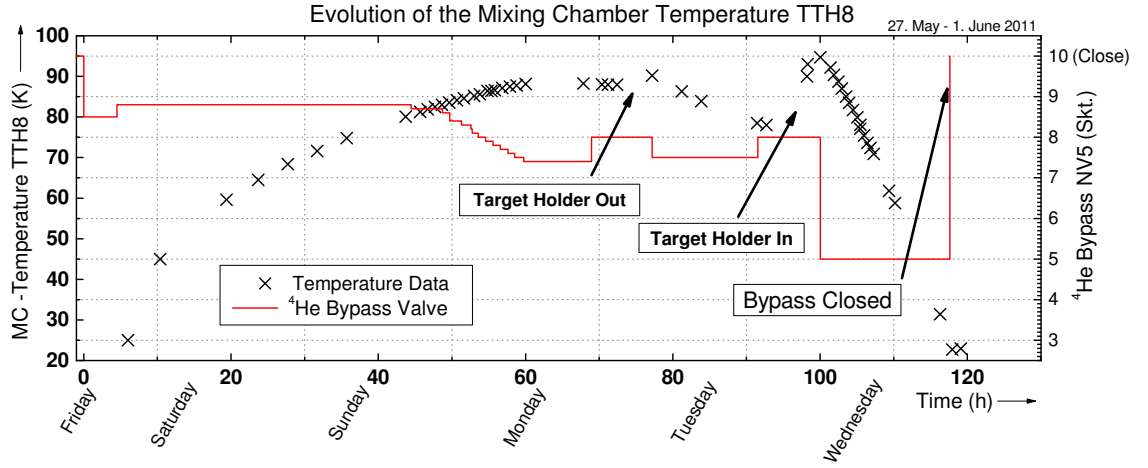


**Fig. 5.15** — Evolution of the temperature in the mixing chamber during the target loading. The red line indicates the  $^4\text{He}$  Bypass valve, which was used to continue the cooling of the mixing chamber, while the target holder was removed.

a systematic error in terms of a background signal, due to the resting hydrogen within the material of the target cells. These hydrogen atoms cannot be polarized dynamically and therefore, the calibration factor is overestimated. To solve this issue, a background signal of the empty target cells must be taken, which is then subtracted from the measured signals. In chapter 6, a new design of the target cells for the DY-period is presented, which should make these background measurements unnecessary.

Figure 5.16 shows the polarization build-up of the fresh target material at COMPASS. Noticeable is a faster build-up in comparison to 2007 and 2010. This behavior was expected, since a relative fast polarization build-up was also observed in Bochum. Even a maximum polarization of more than 90 % could be achieved, while the average polarization was around 85 % over the whole experimental run, see Fig. A.4. By comparing these results with those of 2010, a higher polarization and especially a shorter build-up time of about 14 h to reach a polarization of 80 % are standing out. The FOM-factor (3.2) could be improved by approximately 18 % and considerable more time is spared during the polarization build-up.

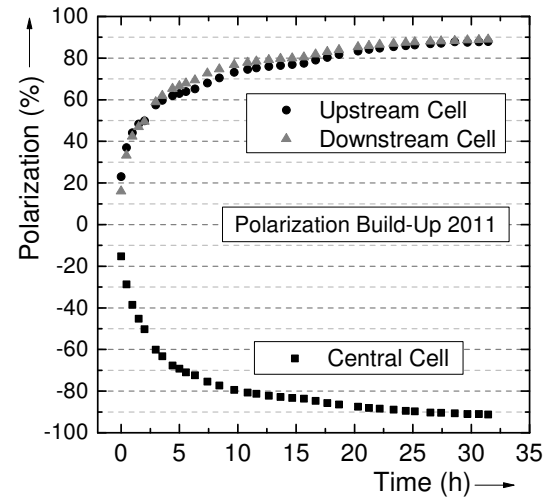


**Fig. 5.16** — Build-up curve of the  $\text{NH}_3$  polarization at COMPASS for 2011.

### 5.3.1 Shift of the Optimal Microwave Frequencies

A target is no constant and rigid tool, but variable through external and internal processes. Thus, the polarization properties of the same target material can change dramatically, when the magnetic field varies, as mentioned in section 3.2. Other external factors are

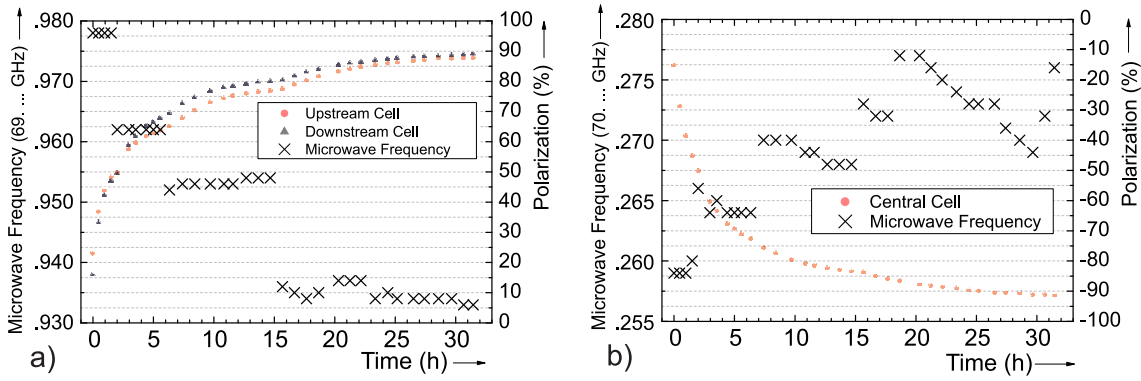


**Fig. 5.17** — Frequency shift of the optimal microwave frequency with increasing polarization at COMPASS in 2011. The microwave frequency must be corrected manually.

difficult to study, such as the consequences of radiation damage, for which an accelerator is needed, like at ELSA or SLAC. But also intrinsic properties are able to modify the behavior and this includes the polarization degree.

As the title suggests, the optimal microwave frequencies for the DNP are shifted at a very high nuclear polarization. According to (2.24), a high polarization means also a high magnetization of the sample. The individual magnetic moments create local fields, which are less compensated, at a higher degree of polarization. Therefore, the paramagnetic electrons are exposed to a small field, in addition to the external magnetic field. For this reason, the Larmor-frequencies of the electrons  $\nu_e$  and thus, the polarization frequencies change a little bit, as it can be seen from Fig. 2.6. As a consequence, the microwave frequencies have to be readjusted during the polarization build-up, in order to obtain the maximum polarization. Figure 5.17 shows such an adjustment of the frequencies during a build-up.

This interaction among the particle species works also in the opposite direction and can be used to study the relaxation times of the electrons  $T_{1,e}$ , by following the shift of the nuclear Larmor-frequency, while the electron polarization is destroyed and rebuilt, like it is well demonstrated in the doctoral thesis of C. HESS [14].

Since at COMPASS II, more radiation damage is expected for the target material due to the pion beam, this may also lead to a shift of the optimal polarization frequencies, as it is proposed in [48]. The production of more radicals and defects, may alter the EPR-line, which could change the position of the best polarization frequencies.

## Summary

In this chapter, the relaxation and polarization behavior of the fresh material is studied as well as compared to the previous used material, which was produced in 1995. Besides a distinct fast relaxation, the peculiar relaxation behavior could be reproduced, which demands more than a single exponential function to describe the polarization decay properly. By taking a look 'into' the target and its ingredients, there are some plausible explanations for this behavior. Due to doping by irradiation, more than just only one kind

of paramagnetic center is produced, in contrast to chemical doping. Two of these centers, namely the  $\dot{\text{N}}\text{H}_2$  and  $\dot{\text{H}}$  radical, are both active in the relaxation process, but only the  $\dot{\text{N}}\text{H}_2$  radical is used in the DNP process. Thankfully, the  $\dot{\text{N}}\text{H}_2$  radical is quite stable during storage at 77 K, as the material of 1995 impressively demonstrated. Nevertheless, a change in the polarization behavior, the relaxation and in the radical concentration was observed, but only in the first time after the irradiation. The color of ammonia faded away quite fast and after almost a year the color was completely gone. This loss of color corresponds to the changes in the target properties, which are shown in the figs. 5.3 and 5.12. But the data points, which are taken after a year, do not allow any clear conclusion about a trend in the characteristics of the target material.

While in the Bochum measurements, only a small polarization of 4-6 % could be achieved, at COMPASS the same material reaches a maximum polarization of 91 % at 2.5 T and 60 mK, which improves the FOM-factor by approximately 18 %, compared to 2010. During locked in the frozen-spin-mode, an average polarization of about 85 % could be maintained, with a polarization loss of about 0.12 % per day. The build-up time could almost be halved, which leads to a longer experimental time and higher statistics, together with the improved FOM.

Due to the hydrogen contaminated target cell at COMPASS, it is essential to know the background signal of hydrogen quite well, to avoid a miss calculation of the calibration factor. In the next section, a new cell design for the DY-measurement is presented, that is completely free of hydrogen and therefore, should reduce the errors in the calibration. Moreover, a time-consuming blank measurement of the target cell will be unnecessary from then on.



## PCTFE Target Cells for Drell-Yan

In this chapter, the new design of the COMPASS target cells, made of *polychlorotrifluoroethene* (PCTFE) is presented, which should be used during the DY measurements. Since the lepton beam ( $\mu^+$ ) is replaced by a hadron beam ( $\pi^-$ ), a higher radiation exposure is to be expected, even at a relative low beam intensity ( $10^8 \pi^-/\text{s}$ ). More radiation is caused, due to a higher interaction probability in contrast to the muon-beam, and the activated environment through the hadron showers, mostly in the hadron absorber. The higher radiation exposure is already discussed in the previous chapters as well as the consequences for the experiment and the target cells.

Due to the fact, that the cells should contain the target material, they are also directly exposed to the particle beam and become highly stressed, as the target material itself. In section 4.4, simulations of the group of A. MAGGIORA [65] are presented, in which the maximum radiation exposure is estimated to 40 kGy per year in the center of the cells, see Fig. 4.7. So far, the cells were made of a polyamid-net, which is covered with Stycast, a glue to reinforce the stability of the net, see Fig. B.9. The advantage of such a net is of course the small amount of matter, which may less interfere with the scattering, but the drawbacks are, in addition to the uncertainty in the radiation resistance, a contamination with hydrogen. Both, the net and the Stycast-glue contain hydrogen and contribute to the hydrogen resonance signal of ammonia, since the NMR coils are mounted onto the cells.

The next paragraphs should point out, that PCTFE offers many improvements compared to the previous used cells of polyamid.

### 6.1 Material Studies

Three substitutes were in the closest selection, namely FEP<sup>1</sup>, PCTFE and Torlon. The latter material was already used at the Jefferson Laboratories, whereat PCTFE become the standard material for the sample container in Bochum, in the last years. These materials were chosen, because of their good radiation resistance and their stability at ultra-low temperatures. In contrast to the net, the three materials exist as solid body plastics, which is a challenge for the production of the cells and is recalled in section 6.2. Furthermore, the hydrogen content is verified, even though a statement can already be

---

<sup>1</sup>FEP stands for Fluorinated Ethylene Propylene.

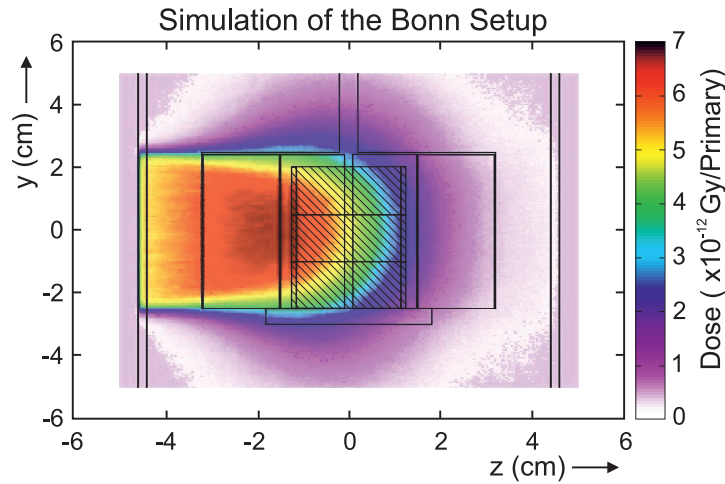


**Fig. 6.1** — Visual result of the Bonn radiation simulation. The hatched areas indicate the three plastics, Torlon, PCTFE and FEP, from top to bottom [65]. In the appendix , Fig. B.1 shows a more detailed view of the simulation results for each sample.

made on the basis of their structural formula. In addition, it is important to know about the thermal properties, when the target cells are cooled down to low temperatures.

### 6.1.1 Test Irradiations

To verify the integrity at high radiation, the materials were exposed to ionizing radiation. All three materials were irradiated at ELSA with an electron beam, and at the proton cyclotron in Jülich, only the PCTFE and all other different materials of the previous used target cells were tested with a proton beam.

#### At ELSA

At the ELSA facility, the same irradiation refrigerator was used, as for the ammonia (Fig. 3.5) , also with 20 MeV electrons and a flux of  $\sim 6 \times 10^{13} \text{ e}^-/\text{s}$ . The materials were fabricated into rings, so that they fit into the cage, in which the ammonia was irradiated before. In order to reduce the measurement effort, all three materials were irradiated at the same time, being stacked on each other, as it is sketched in Fig. 6.1.

The external conditions differ significantly from that at COMPASS II. Both, the beam and the temperatures are different – not to mention the duration of the irradiation. In Bonn, the beam consists of leptons instead of hadrons and the temperature in the refrigerator is not in the milli-kelvin range, like at COMPASS. Since the dose has to be simulated for a one-year experiment, higher radiation dose rates must be used in Bonn. It might be a difference, if the dose is being applied in a short time, or distributed over a long period. Without any considerations, the three plastics were irradiated with the electron beam for about 30 min and they have not taken any severe damage. In order to classify these tests, the group around A. MAGGIORA performed FLUKA-simulations with the Bonn setup [65]. In order to compete with the requirements at COMPASS II, the following question must be answered – *How long must the materials be irradiated in Bonn, to get an effective radiation dose of one year data-taking at COMPASS II?* To do this, the exact

dimensions of the setup and all used materials between the beam and the samples (aluminium, titanium, liquid argon) have to be included. Figure 6.1 shows the visual result of the FLUKA simulation in the unit of 'gray per primary', which represents the deposited energy per kilogram of a single particle, in this case a 20 MeV electron.

**Tab. 6.1** — Results of the absorbed doses of the three samples, according to Fig. 6.1. The number of primaries for 16 kGy, 40 kGy and the irradiation time are scaled with a flux of  $6 \times 10^{13} \text{ e}^-/\text{s}$  [65].

	Torlon	PCTFE	FEP
Dose (Gy/primary)	$2.7 \times 10^{-11}$	$2.8 \times 10^{-11}$	$2.1 \times 10^{-11}$
<b>16 kGy</b>			
– Number of Primaries	$5.9 \times 10^{14}$	$5.7 \times 10^{14}$	$7.6 \times 10^{14}$
– Irradiation Time (s)	9.8	9.5	12.7
<b>40 kGy</b>			
– Number of Primaries	$14.8 \times 10^{14}$	$14.3 \times 10^{14}$	$19.1 \times 10^{14}$
– Irradiation Time (s)	24.7	23.8	31.8

With the known particle flux of  $\sim 6 \times 10^{13} \text{ e}^-/\text{s}$ , the time can be estimated until the target dose of 16 kGy (or 40 kGy) is reached, see section 4.4. According to the simulation, 16 kGy is the maximum at a radius of 2 cm from the beam axis, whereas approximately 40 kGy is expected in the center, at the very end of the downstream cell (Fig. 4.7).

The result is surprising, since only about 10 s should be necessary to achieve the corresponding radiation dose of 16 kGy ( $\sim 25$  s for 40 kGy). In Tab. 6.1, the results for the different materials are summarized. The most conspicuous difference between the irradiation is the flux of the particle beam at ELSA, which is five orders of magnitude larger than at COMPASS II. Furthermore, the assumption is made in the calculation, that every electron of the flux interacts with the samples. However, the plastics were irradiated significantly longer in Bonn, as this short time.

In the meantime, FEP and Torlon were excluded as materials for the target cells, because FEP has a smaller tensile strength compared to PCTFE and Torlon contains hydrogen, which is demonstrated in the next section.

### In Jülich

In addition to the radiation test at ELSA, the PCTFE material was also tested during the irradiation of the temperature sensors in Jülich, which is discussed in chapter 7. Together with the materials, which were used so far for the target cells, PCTFE was exposed to a 45 MeV proton beam up to a dose of approximately 20 kGy, see Fig. 6.2. None of the materials had shown any visible damage, not even the polyamid net. Only a slight discoloration of the net/Stycast compound and the dental floss (polyamid cord) was observed. The latter was used to stitch the net together. Again, the external conditions of the

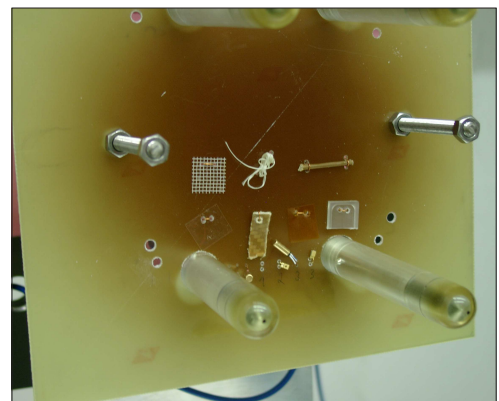


**Fig. 6.2** — Picture of the radiation exposed materials and sensors at 20,000 Gy. The round discoloration is a result of the irradiation with the proton beam.

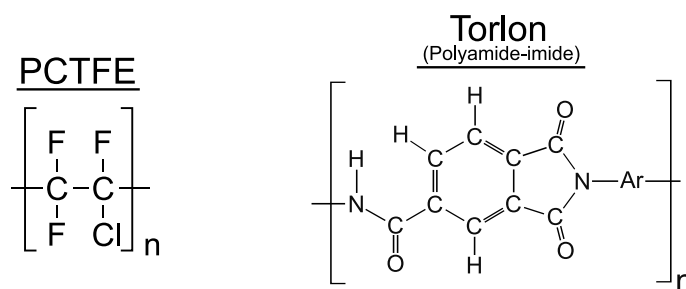


**Fig. 6.3** — Skeletal chemical structure of PCTFE and Torlon. Both materials are polymers and only the repeating unit is displayed. The acronym 'Ar' stands for an aromatic substituent [72].

COMPASS II experiment could not be reproduced. In Bonn, the samples were kept under liquid argon (87 K/-186 °C) during the irradiation, whereas in Jülich, the materials were at room temperature and irradiated at atmospheric conditions<sup>2</sup>. The dose rates went up to 2.5 Gy/s and the total dose of 20 kGy was applied within 5 hours, instead of a complete experimental year at COMPASS. Therefore, these tests can only be used as reference points for the characteristics in the later experiment.

### 6.1.2 Hydrogen Content

Another important factor is the hydrogen content of the materials, even if this was not the initial reason for the new design of the target cells. In section 5.3, the consequences of such a contamination is described, as well as the need of a blank measurement without the target material, in order to minimize systematic errors. The blank measurement has to be performed either before the target is loaded or after the experiment has ended and the target material is already removed. This task is a time consuming procedure and the risk of contaminating the refrigerator with water rises. In Fig. 6.4, the background signal is presented, together with the TE-signal of the fully loaded target at 1 K, which was taken in 2011 with the net cell. Therefore, a target cell, which is hydrogen-free, would be a great advantage compared to the previous cells.

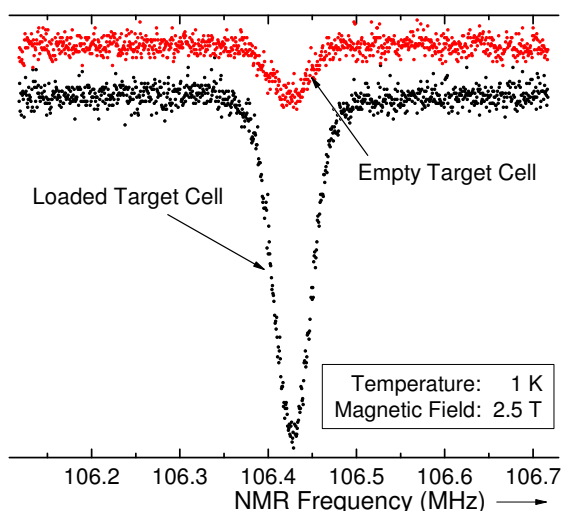


**Fig. 6.4** — Comparison of the TE-signals of hydrogen between an empty and a fully loaded target cell. These signals were taken in the COMPASS run of 2011.

Torlon was already used at the Jefferson Laboratories, in which the radiation doses at the experiments are usually high and thus, the radiation hardness of Torlon is beyond question. However, Torlon contains hydrogen, which can already be seen in the structural formula, see

<sup>2</sup>Oxygen may have a negative reinforcing effect in the interaction between radiation and matter and can cause oxidative degeneration[71].



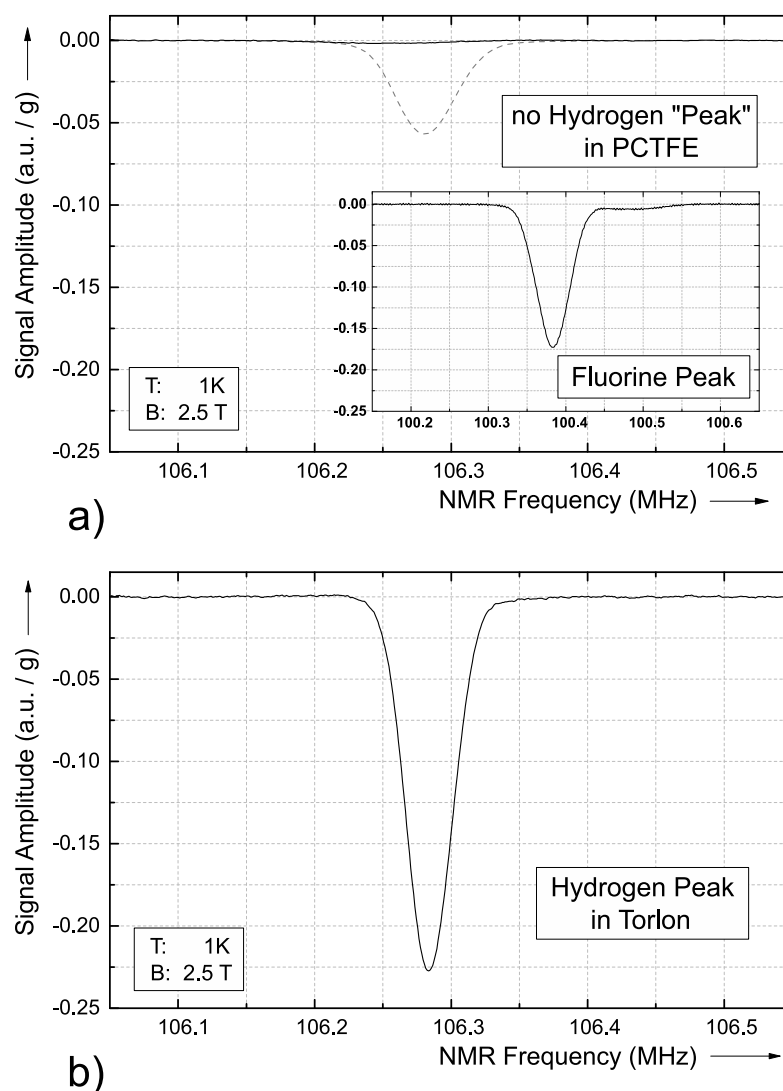


**Fig. 6.5** — Measurement of the hydrogen content of PCTFE and Torlon. All graphs have the same scale and the resonances are normalized for a sample weight of 1 g. Each signal is measured at TE.  
**a) PCTFE:** No hydrogen is visible. The dashed line shows the expected resonance intensity, if the repeating unit of PCTFE would contain only one hydrogen atom. The smaller graph shows the fluorine peak of the same sample.  
**b) Torlon:** A clear resonance of hydrogen is visible, which would cause systematic errors in the TE-calibration at COMPASS.

Fig. 6.3. In contrast, the structural formula of PCTFE shows no hydrogen. Both materials<sup>3</sup> were prepared in the form of a solid target container, which is often used in Bochum ( $h = 18 \text{ mm}$ ,  $\varnothing = 8 \text{ mm}$ ). Since the samples do not contain any paramagnetic centers, only the TE-polarization can be measured. Figure 6.5 shows the results, normalized to a weight of 1 g. In the graph of PCTFE, the fluorine peak is displayed and the prospect of the contamination of one hydrogen atom per repeating unit (dashed line), but instead, no hydrogen is measured in PCTFE. In Torlon, the TE-signal of hydrogen is clearly visible, which confirms the expectations of the structural formulas. Besides the hydrogen contamination in Torlon, the group at the Jefferson Laboratories has revealed, that the hydrogen can be polarized dynamically, after the material was exposed to radiation

<sup>3</sup>Torlon was provided by the company 'Arthur Krüger' and the PCTFE was acquired from the company 'KELUX Kunststoffe GmbH'.

[30]. This behavior would cause further uncertainty in the polarization measurement at COMPASS. With this results, PCTFE was chosen to be the next material, from which the target cells are to be produced. But there is still another characteristic, which should be tested and this is the thermal expansion, or in this case thermal shrinkage.

### 6.1.3 Thermal Shrinkage of PCTFE

Usually, matter shrinks as soon as it is cooled down, with the exception of a handful substances, including water. Since PCTFE will be exposed to ultra-low temperatures, it is important to have an idea of how much the material will change during the cool-down. In literature, the coefficient of linear thermal expansion varies for different temperature ranges and decreases toward lower temperatures, see Tab. 6.2.

In order to verify the degree of shrinkage, a short and a large section were jointed together and frequently cooled-down. However, in this test, only the contraction from room temperature to the temperature of liquid nitrogen (77 K/-196 °C) could be measured, and only at these very points. For this purpose, the size of the pieces were measured several times at various positions (length, (inner) diameter) and at a known temperature. For this reason, the pieces were immersed into a bath of liquid nitrogen, until they were completely cooled down. Afterward, they were placed on a thermal insulating surface, which was also covered with liquid nitrogen and then again, the size of the pieces were measured. Every time after a measurement, the pieces were laid back into the nitrogen bath.

Based on the measurements at two temperature points, the thermal expansion coefficients can be calculated, but with the restriction, that two data points are not quite enough information for an accurate determination, since the expansion coefficient is not constant along the temperature. A better value is the percentage reduction of the material, between room temperature and the temperature of liquid nitrogen. The measured shrinkage of the target cells is  $\sim 0.91\%$  in all directions. Nevertheless, both quantities are listed in Tab. 6.2. In contrast to that, the guiding value for the net-target cells were approximately 2 %. With this, an improvement has been reached already.

In addition to the shrinkage checkup, a stress test with several cooling-down and warming-up cycles were performed, in order to check the mechanical stability. In total, 15 complete cycles were done and no loss of stability could be noticed. In comparison to the net, the rigidity of PCTFE is much bigger, which is another advantage for the alternative material. The next section deals with the design of the new target cells, as well as with the improvements and the problems.

**Tab. 6.2** – Thermal linear expansion coefficient of PCTFE. Literature values were taken from [73].

Temperature Range ( °C)	Linear Expansion Coefficient (K <sup>-1</sup> )
<b>Literature</b>	
+30 to -30	$7.0 \times 10^{-5}$
-30 to -100	$5.1 \times 10^{-5}$
-100 to -190	$3.6 \times 10^{-5}$
<b>Measurement</b>	
+25 to -196	$(4.2 \pm 0.5) \times 10^{-5}$
Shrinkage	$\sim 0.91\%$

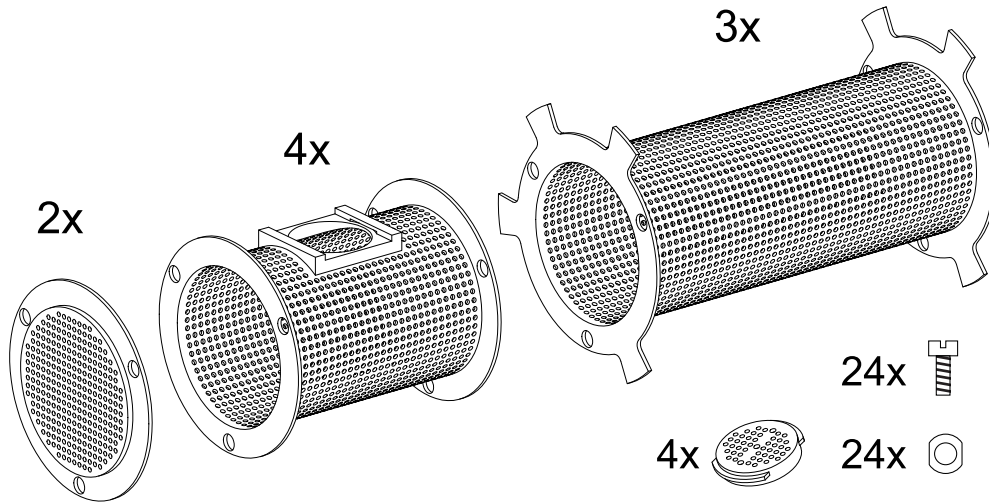


**Fig. 6.6** — Overview of the different parts of the PCTFE cell body. The numbers refer to the amount, which are necessary to assemble one cell. In total, a cell consists of 61 parts.

## 6.2 Design of the PCTFE Target Cell

Since the first experiments at EMC, the target was one of the largest in the world and this required also large target cells. The target volume and thus, the dimensions of the target cells varied over the years and experiments. The total volumes of the previous targets were between 0.848 L and 2.5 L (at the SMC). During this time, not only the dimensions have changed, but also the cells were divided from two into three sections. A three-cell configuration leads to a further reduction of the false asymmetry in the experiment [56]. Figure 6.7 shows the history of the used target cells, in which all different versions can be compared to each other. Between the cells, there is a gap of several centimeters, which is necessary for a doubtless identification of the scattering vertex to a distinct target cell. In addition, microwave stopper are placed into the gap, mostly made of copper and a meshwork, in which coal is integrated. This construction should prevent a trespass of the microwaves from one cell to another, so that the cells can be differently polarized. Nevertheless, the stopper must be permeable for the helium, in order to cool the whole target sufficiently.

### 6.2.1 Specifications

Although, the new design should be technically oriented on the previous versions, there is a lot of space for improvements. The initial specifications were taken from a previous drawing of the net cells, see Fig. B.2, which were already used in the test measurement of 2014. The given conditions are two cylindrical cells, each with a length of 550 mm and 40 mm in diameter. The surface should be perforated for a sufficient cooling of the target material. In addition, the cells should have enough lockable filling-holes, in which the target material can be filled in. The cells should also provide a construction for mounting themselves and additional wires, for NMR coils, temperature sensors and the  $^3\text{He}$  supply-line. Another essential condition is the amount of the used material, which should be minimized, in order to affect the scattering as little as possible.

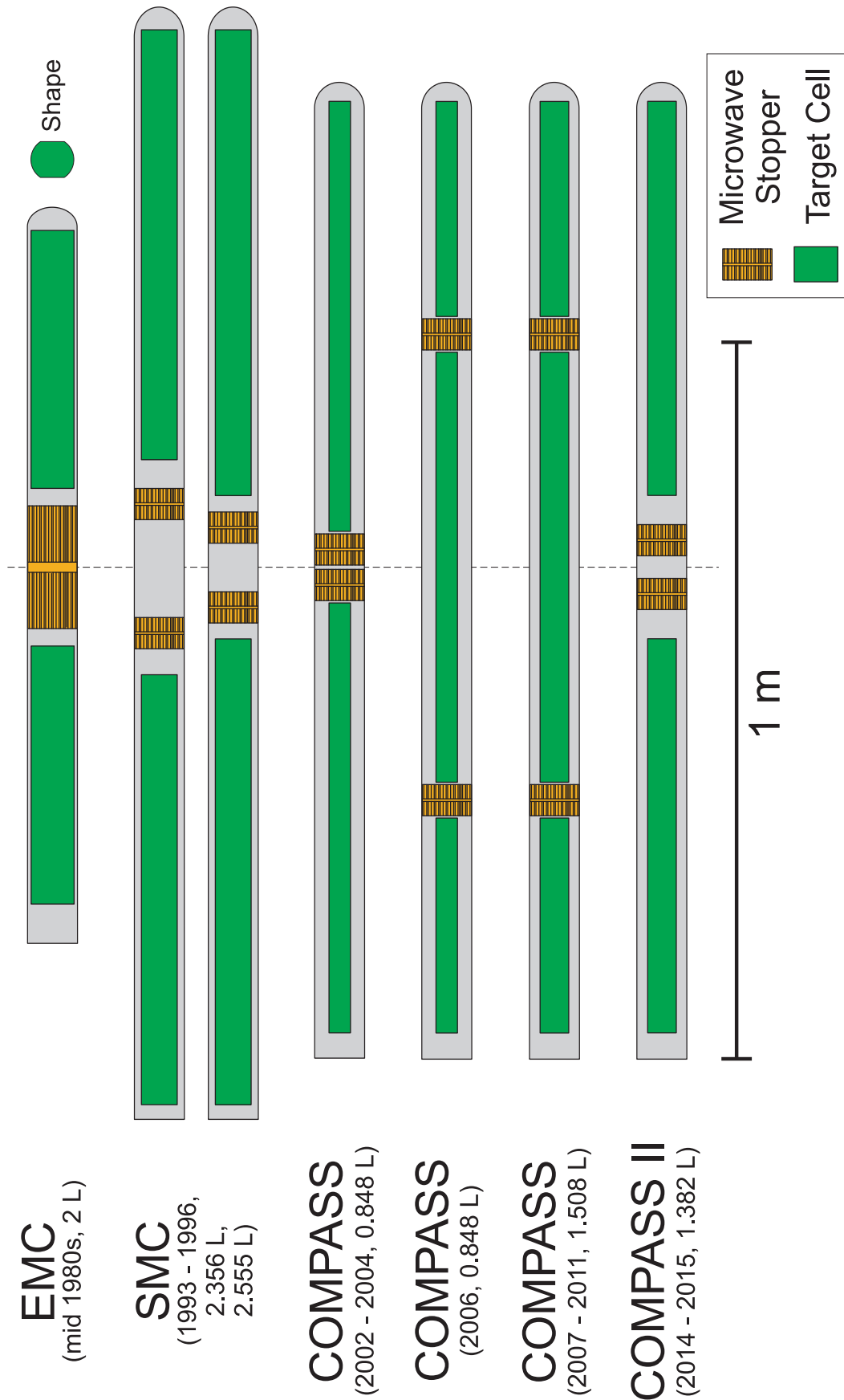


**Fig. 6.7** — History of the target cells at COMPASS and its predecessors. All cells have a round shape, except the cell at the EMC experiment. Most of the dimensions are taken from [44, 56, 74, 75, 76]. In the picture, the sizes and positions of some microwave stoppers are arbitrary and only guessed, since for the early versions, no precise information could be found. In Tab. B.1, the dimensions of these cells are summarized.

### Problems and Solutions

During the planning of the new design, both, problems and ways to improve the cell had showed up regularly. The first challenge at all, was to create the cells from this solid material. In order to minimize interfering materials, which contain hydrogen, any kind of glue or else must be omitted. The best way is, to produce the cells just by using PCTFE. The raw materials were PCTFE tubes with an outer diameter of 70 mm and an inner diameter of 30 mm – the latter reduces the cutoff and material cost. However, working with a length of half a meter was found to be very difficult, in order to keep the precision high enough. For this reason, the decision was made to build smaller sections, which can then be combined to a whole cell. Since the use of any glue must be avoided, the sections have to be attached with another technique. The first idea was to use a kind of a bayonet lock, but this idea was rejected and in the end, simply a screw in combination with a screw-nut is used to join the sections. The screws and the screw-nuts were made of PCTFE as well, which ensures that all pieces shrink in the same manner and reduces the mechanical stress during the cool-down process. Moreover, no additional hydrogen-containing materials were used in the construction of the cell bodies.

The start drawing in Fig. B.2 shows four openings for a cell, each with a diameter of 20 mm, through which the material can be filled into the cells. These openings are closed with a lid and the locking mechanism is showed in 6.8. This feature should also be adopted for the current design and was substantial for the planning of the sections. Figure B.7 shows a series of images at several stages of the cell development. The new cell design consists of seven sections and two end-caps, to cover the back and front of the cell. Attention was paid, to keep the number of different sections low enough, so that the target cells can be assembled in a modular system. The final design is a combination of small pieces with a length of 61 mm, which provide the filling-hole, and long connecting pieces of 102 mm with eight wings, whose function will be described later in the text.

In Fig. 6.6, all parts are pictured in addition with the required number for one cell. The advantage of a modular system is, the replaceability of a defect section, without reproducing a whole new cell. In an earlier design stage, separate end-sections were planned, in which one sides is already closed, but this construction was castaway after a tip with a better solution<sup>4</sup>. Instead of whole sections, only the end-caps were built, which can be screwed on one of the other sections. Consequently, the number of different sections could be simply reduced to two and an end-cap. This decision holds another benefit, which goes along with the thermal contraction. The cells were planned with a length of  $L_0 = 550$  mm, but due to the cooling, they will shrink and become smaller.

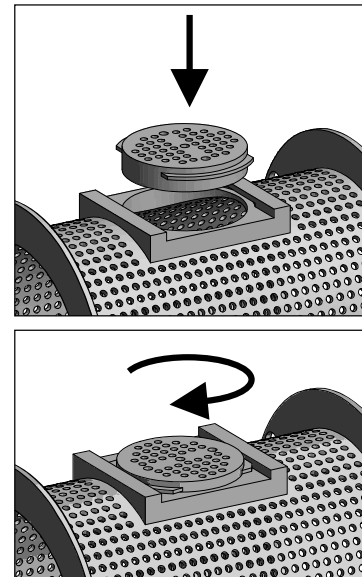


**Fig. 6.8** – Locking mechanism of the filling-holes.

<sup>4</sup>Thank you Jonas!

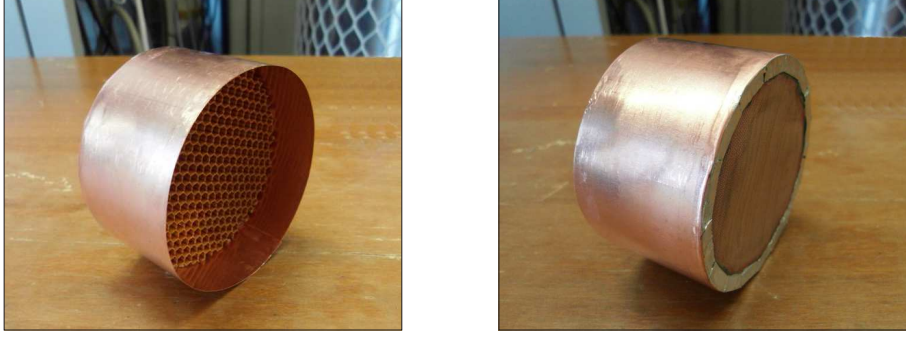


**Fig. 6.9** – Pictures of a microwave stopper. A copper sheet is wrapped around a honeycomb construction, in which coal is integrated, to absorb the microwaves. On one side, the stopper is closed with a dense copper mesh.

The end-caps have the potential to compensate the shrinkage, with an extra length of  $x$  to the initial length  $L_0$ . In the end, the cell should also be  $L_{\text{end}} = 550 \text{ mm}$  long, and with the tests in section 6.1.3, an estimation of  $x$  can be made, at least down to a temperature of 77 K. With the expansion coefficient of  $\alpha = 4.2 \times 10^{-5} \text{ K}^{-1}$  and the temperature difference  $\Delta T = -216 \text{ K}$ , the extra length  $x$  can be expressed as

$$x = \frac{L_{\text{end}}}{1 + \alpha \Delta T} - L_0 = 4.99 \text{ mm} \approx 5 \text{ mm} \quad . \quad (6.1)$$

Therefore, each end-cap should enlarge the cell by 2.5 mm, in the warm state. To verify this result, a fully assembled target cell was cooled in liquid nitrogen. The initial length at room temperature was 555.4 mm, whereas after a temperature difference of  $\Delta T = -218 \text{ K}$ , the cell was only 550.6 mm long, which corresponds to a shrinkage of 0.87 %. For a diameter of 40 mm, this means a reduction of only 0.35 mm, which is quite acceptable. Now, a feature of the long piece is discussed, which was already mentioned before – the wings. At COMPASS, the target cells are cased in a tube, made of epoxy reinforced aramid (Kevlar), with an inner diameter of 69 mm. So far, for a centered alignment of the cells, constructions of a Kevlar ribbons, covered with Stycast were made and slipped over the cells. In a picture of Fig. B.9, this distance piece can be seen, which have several additional loops. These loops were used to hold three fixation rods and the supply-line for  $^3\text{He}$ . The fixation rods contribute to the stability of the cells over their entire length and provide attachments for NMR wires and temperature sensors.

Since, only PCTFE should be used in the new design, the spacers are directly integrated into the long cell section, recognizable by the wings. If necessary, the wings can be drilled through, in order to install the fixation rods and the  $^3\text{He}$  supply line. However, the fixation rods may only be needed for the wiring attachment yet, because due to the spacers and the PCTFE itself, the cells are already stiff enough to stabilize themselves.

Other critical parameters are the wall thickness and the hole pattern. For the scattering process, the extra amount of non-target material should be minimized as much as possible, but without the risk of losing the stability of the target cells. However, in this case the bottleneck was the production process, in which the wall thickness was successively reduced with the result, that there is a limit at 800  $\mu\text{m}$  for the drilling process.

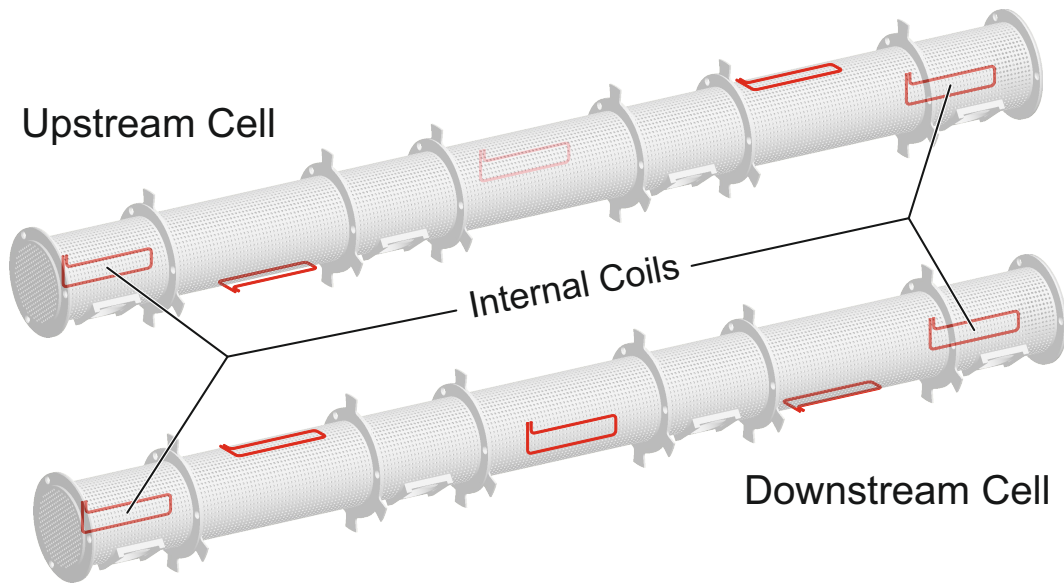


**Fig. 6.10** — Configuration of the NMR coils for the new target cell. Each cell is equipped with five coils. Three of them are mounted on the surface, while two are located within the cell. It should be noted, that the coils on top and bottom of the cells cannot be used during the transverse mode, since the external field is parallel to the oscillating field of the NMR coils.

The numerous holes in the surface are intended for a proper cooling of the target material, but they also reduce the mass of the cells. Here, the holes must not be larger than the ammonia beads, which have a size of 2–3 mm. Therefore, a diameter of 1.2 mm was chosen, with a center hole distance of 2 mm for the holes in a row along the axis, and an angular distance of  $6^\circ$  for the holes that go around the cell.

However, the net target has a clear advantage in the wall thickness and the holes, but the benefits of PCTFE, such as stability, avoidance of hydrogen and a better radiation hardness, outplay the net.

### 6.2.2 Final Assembly

The final cells consist of more than just the PCTFE body, which is partly mentioned in the previous paragraphs, such as the microwave stopper, the fixation rods and the NMR coils. Like already mentioned, the microwave stopper has the function to prevent a coupling of microwaves from one cell to another. In Fig. 6.9, pictures of a microwave stopper is shown, which is coated with a copper sheet and closed on one side with a dense copper mesh. Within the stopper, there is a composition of cellulose and coal in a honeycomb structure, which absorbs the microwaves very well. This effect is also used in the Speer-resistors, in order to estimate the absorbed microwave power of the target material. Two stoppers are placed between the cells and a third stopper separates the upstream cell from the rest of the target holder, which can be seen in Fig. 4.1. In the new design, the fixation rods are also made of Kevlar, overcast with Stycast, but not all of the rods need to be installed, only those, which hold the wiring for the sensors and the NMR coils. As long as the coils are not mounted in the immediate vicinity of the rods, their hydrogen content should not cause any problems.



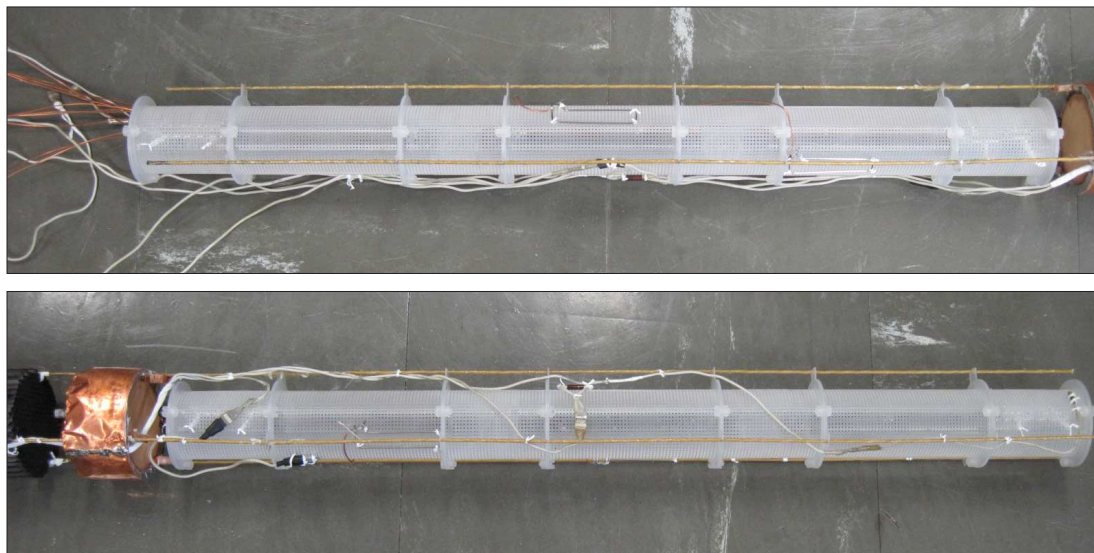


**Fig. 6.11** — Pictures of the fully equipped PCTFE cells, with fixation rods, NMR coils and temperature sensors.

In total, 10 NMR systems are available and in the three-cell version, the coils were distributed in the pattern 3–4–3 (up/central/down). For the current design, each cell has three coils mounted on its surface and two coils within, as illustrated in Fig. 6.10. Each coil has a size of 50 x 10 mm and is made of a stainless steel tube. To avoid a direct contact between the target material and the internal coils, they are surrounded with PCTFE. For the test measurements in 2014, special cases were prepared, in which the coils could be put inside, whereas for the new design, an alternative with a very thin PCTFE foil is available, which can be wrapped around a coil. As a conclusion, Fig. 6.11 shows pictures of the fully equipped and new PCTFE target cells.

## Summery

In this chapter it could be seen, that PCTFE holds many benefits compared to the previous used net target cells. The initial motivation was a cell, which might tolerate a higher radiation level as the polyamid net, but this issue could not be clarified in the radiation tests in Jülich. All materials, including the net, have withstood the test unharmed. Nevertheless, PCTFE is known for its very good radiation resistance from many different other industrial fields. Additionally, PCTFE offers design flexibility, excellent mechanical and thermal properties and an easy processibility. One of the best advantages for the target business is well founded in the structure of PCTFE, because it contains no hydrogen and thus, it is perfect for measurements concerning the nuclear properties of the proton.

The new target cell was designed in a modular system, which allows an easy replacement of defective sections, or even a rearrangement of the cell itself. All features of the cells, which had to be added to the net-cell version, are integrated a priori into the new design, without any glue. Therefore, the cells consist only of hydrogen free PCTFE, which should make a time consuming background measurement unnecessary. Only the fixation rods and the tube, in which the target cell is pushed into, is made of reinforced Kevlar and might produce a small background signal in the NMR coils.



## Radiation Hardness of the Temperature Sensors

The polarization measurement depends on a precise knowledge of both, temperature and magnetic field. Like mentioned in section 2.2.2, the temperature has a significant influence on the TE-calibration, in which the polarization at TE is estimated, by using the measured temperature at a known magnetic field, see (2.19). At COMPASS, the sensors are in the close vicinity of the beam and exposed to a non-negligible high radiation. Therefore, it is mandatory to know, if the temperature sensors return the correct value, after a exposition to a certain radiation dose. For the calibration, the main information of the temperature within the mixing chamber comes from the vapor pressure measurement of helium, and this might be supported with the resistors, in particular. So the question must be, whether the radiation hardness of the sensors is good enough for this experiment, to ensure a reliable measurement of the temperature during the whole experimental period.

This question will be answered in collaboration with the group at the Jülich proton cyclotron. Several sensors were irradiated, with different radiation doses and their behavior at low temperatures was measured, afterward.

### 7.1 Temperature Sensors

Two different types of temperature sensors were tested, but these types are not the only possibilities to estimate the temperature at the COMPASS target system. There exist the way, to measure the temperature also over the vapor pressure of helium<sup>1</sup>. The checked sensors are  *ruthenium-oxide resistors*  (RuO) of the type RX-102A and silicon diodes with the name DT-670. The RuO-resistors work best below 1 K and the diodes are more suitable for the range above 1 K. These types correspond to the sensors TTH4,5,6 and 8 in the experiment and are located in the vicinity of the beam axis, see Fig. 4.1.

For the investigation of the radiation hardness, three sensors of each type were bought, which were not calibrated. In addition to these six sensors, only one calibrated RuO-resistor was ordered as a reference for all following measurements<sup>2</sup>. The calibrated sensor is the only one, that was excluded from the irradiation. Due to different operation modes, the

<sup>1</sup>Performed with a capacitance manometers (Baratron) of the company MKS ([www.mksinst.com](http://www.mksinst.com)).

<sup>2</sup>Both sensor types are bought from Lake Shore Cryotronics Inc., Ohio, USA.

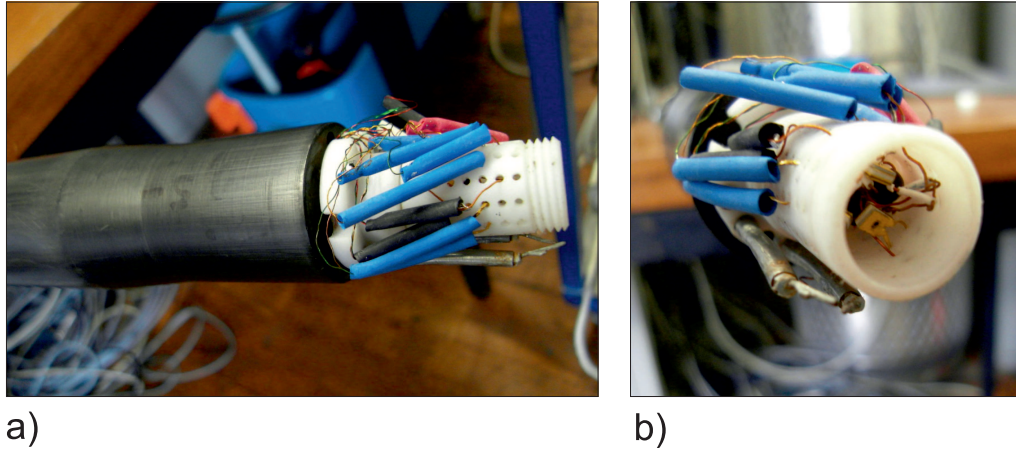


**Fig. 7.1** — Pictures of the temperature sensor setup. Side view **a)** of the bottom of the refrigerator inlet and a close-up **b)** of the sensors within the a target container.

sensors require also different readout techniques. As for the resistors, the existing resistance bridge could be used, whereas for the diodes, a suitable readout electronic had to be found.

### 7.1.1 Setup

In order to simplify the measurements, all seven sensors were read-out at the same time. The refrigerator inlet has a limit of two connector sockets with 11 pins, and the diodes and resistors are each assigned to a socket. With these limitations it was not possible to measure all sensors via the four-terminal method and consequently the wire resistance could not be excluded. Only the calibrated sensor was connected with four wires, in order to allow an accurate temperature measurement.

However, in this study, only the relative change to its initial behavior is important. All sensors are placed in a container<sup>3</sup> at the end of the refrigerator inlet, in which usually the target material is located, see Fig. 7.1. This ensures that all sensors are exposed to the same temperature at the same time. The next section is dealing with the read-out system of the resistors and diodes.

### 7.1.2 Read-Out System

#### Ruthenium-Oxide Resistor

The RuO-resistors are read-out with the existing AVS-system<sup>4</sup>. The three uncalibrated resistors are connected only with two wires, until they reach the AVS-box and this leads to an offset of roughly  $20\ \Omega$ , due to the wire resistance. The resistors are connected via cryogenic-appropriate wires<sup>5</sup> to a 11-pin plug at the top of the removable refrigerator inlet. This plug is connected to a box, where each pin can be separately linked to a AVS-port. The AVS is then read by a GPIB-interface<sup>6</sup> and the values are fed to a data acquisition

<sup>3</sup>A standard target cylinder with 10 mm in diameter and a height of 15 mm.

<sup>4</sup>Low temperature resistance bridge (Picowatt AVS, see [www.picowatt.fi](http://www.picowatt.fi)).

<sup>5</sup>Quad-Twist™ cryogenic wire of the company Lake Shore Cryotronics.

<sup>6</sup>GPIB stands for General Purpose Interface Bus.

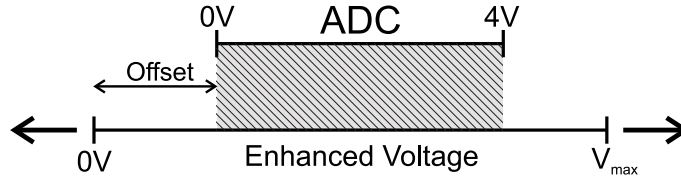


**Fig. 7.2** — An illustration for the need of an offset in the THMP, in order to measure the top end of the enhanced diode voltage, which corresponds to low temperatures.

software written in LabView, which is able to log the resistance in addition to several other parameters, such as pressure or the helium level. In fact, every parameter based on a voltage measurement can be recorded with this program.

### Silicon Diode

The diodes cannot be read with the AVS and therefore, a different readout system had to be found. The diodes must be supplied by a constant current source, which should be able to provide 10  $\mu\text{A}$ . An elegant solution came from the group of Prof. U. WIEDNER at the Ruhr-University of Bochum. Their efforts in building a monitor-system for several kinds of temperature and humidity sensors lead to a compact unit, which could be easily altered to fit our needs. This box is called *Temperature and Humidity Monitoring Board for PANDA* (THMP) and combines a constant current source, plus the readout electronics based on a FPGA-chip<sup>7</sup> with a CAN-BUS interface [77]. The THMP is able to digitize the measured voltage, which can then be processed with a suitable software.

First, the hardware had to be modified to supply the 10  $\mu\text{A}$ , as well as the right gain and offset. For this purpose, the way has to be known, in which the voltage is represented through the channels. The build-in ADC<sup>8</sup> has 14 bits and provides 16384 channels, which covers a range of 4 V. Therefore, the width of one channel corresponds to  $2.441 \times 10^{-4}$  V. To use the full bandwidth of the ADC, the intrinsic voltage of the diodes of maximal 1.6 V has to be enhanced. The lowest possible gain in this THMP version is a factor of 5. Therefore, the measured voltage can get up to 8 V, which is far to high for the ADC. Without any modification the THMP would always return the highest channel number at low temperatures. Thus, to be able to measure at low temperatures, an offset must be installed to shift the relevant voltage into the range, which is covered by the ADC, see Fig. 7.2. For this task an offset of -4.47 V was chosen, so the highest possible voltage of the diode does not exceed the upper edge of the ADC. With this information, the conversion between voltage  $V$  and output-channel can be calculated with

$$V = \frac{\text{channel} \cdot \frac{4\text{V}}{16384} - \text{offset}}{\text{gain}} . \quad (7.1)$$

Due to the offset, only temperatures below 90 K are measurable with the diodes in combination with the THMP. The channels are transmitted via a CAN-BUS system and

<sup>7</sup>FPGA stands for Field Programmable Gate Array.

<sup>8</sup>ADC stands for Analog-to-Digital Converter.

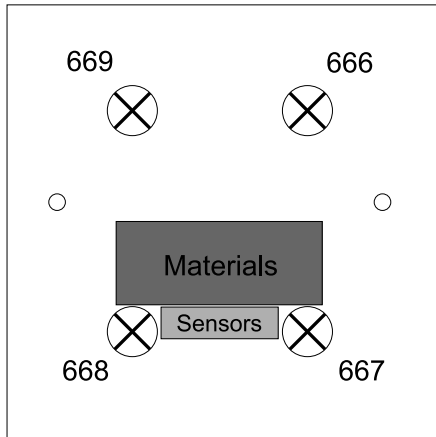


**Fig. 7.3** – Front-view draft of the irradiation board. The sensors are surrounded by the dose detectors (666,667,668,669).

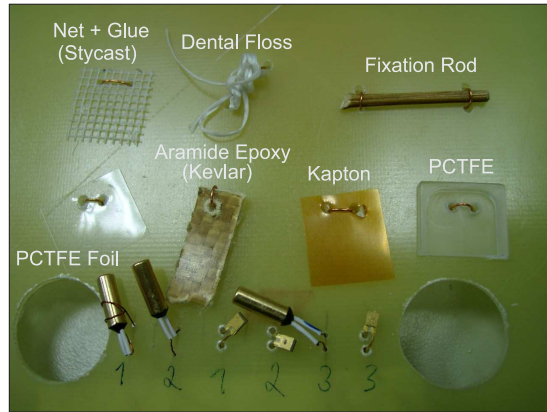


**Fig. 7.4** – Close-up photography of the irradiation board. Next to the target-cell material, the resistors (long cylinders) and diodes (small squares) are visible.

all 64 sensors of the THMP are returned at the same time<sup>9</sup>. As a converter between THMP and the computer, the Tiny-CAN II-XL of the company MHS electronics is used, which is compatible with the most common programming languages. A program was written in LabView, which can read all potential 64 sensors with the option to show the selected sensors in a graph and save them to a file, see appendix C.1. In fact, all 64 sensor values are returned, if the read-out command is sent, even if they are not connected. In addition, the gain and offset can be set separately for each module, to convert the channel online into a voltage value, according to (7.1). The next step is the preparation of the measured values, so they are comparable to each other.

## 7.2 Irradiation of the Sensors

The irradiations were done at the proton cyclotron in Jülich, with a beam energy of 45 MeV – a hadron beam, which is closer to the situation at COMPASS II ( $\pi^-$ ) instead of the lepton beam ( $\mu^+$ ) before. But, the exact same conditions cannot be reproduced, as mentioned before in section 6.1.1. The sensors were irradiated on a day-scale and not over months, as in COMPASS II. In addition, the irradiation was performed at room temperature and atmospheric conditions. This may affect the kinds and life-time of produced defects, as set out in section 3.3.2. Nevertheless, these measurements should reveal, if the sensors are sensitive for a high radiation or not.

All in all, two irradiation runs were performed. For the first run, the sensors were mounted on a board together with NMR electronics [7] and placed right into the beam. Four irradiation detectors, so-called Farmer-chambers<sup>10</sup>, were placed on the board to measure the accumulated radiation dose, Fig. 7.3. The aim of 100 Gy for the first irradiation was accomplished with a dose rate of 0.5 Gy/s. After a convenient ring-down time, the sensors were measured in the  $^3\text{He}/^4\text{He}$ -dilution refrigerator in Bochum. For the

<sup>9</sup>The THMP board can carry a maximum of eight modules with eight sensors each. The data is measured in a 8 s cycle – one second per module – and stored in a buffer for the read-out command.

<sup>10</sup>PTW Farmer® Ionization Chambers, see [www.ptw.de](http://www.ptw.de).

second run, only the sensors and several different materials were placed in the beam, of which the previous target containers were made of, see Fig. 7.4. In this run, multiple end doses were defined for each resistor/diode pair. So the sensors R1/D1, R2/D2 and R3/D3 got a total dose of 1 kGy, 10 kGy and 20 kGy, respectively.

This decision was made, due to the lack of time with the duration of the radiation ring-down time of about a month between irradiation and measurement. The dose rate varied between 1 Gy/s and 2.5 Gy/s, but the measured accumulated dose was not as accurate as it seems, because the position and orientation of the dosimeters have a great influence on the dose measurement. However, from the described simulations in section 4.4, a dose of 16 kGy will be

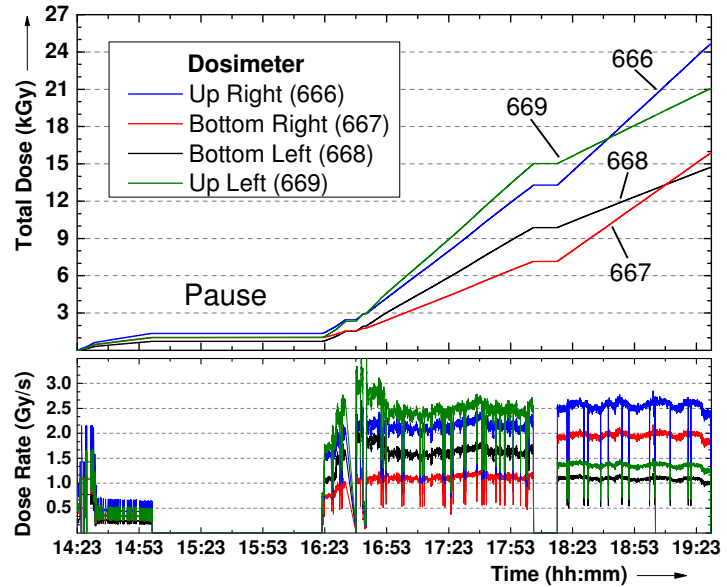


**Fig. 7.5** – Overview of the second irradiation run in Jülich. The dosimeter numbers correspond to Fig. 7.3.

expected at the location of the sensors for a COMPASS year, so the radiation dose applied in Jülich was in the same order of magnitude. In the next section, the characteristic curves of the sensors are compared for different doses.

### 7.3 Comparison of the Sensors

The true temperature is given by the calibrated RuO-resistor, using (C.1). Each resistor has in total three curves – zero dose, 100 Gy and the respective target dose. Due to a technical problem in the beginning with the current source of the diodes, only two curves could be measured – 100 Gy and the target dose.

It was not possible to record the temperature curve in one pass and do it always in the same way. All sensors were merely measured together, but the cool-down procedure was neither reproducible, nor straight forward between the irradiations. Due to safety regulations, there was also a time of several weeks between irradiation and measurement and thus, each temperature sensor is first compared to the calibrated sensor, which was not irradiated. The aim is a construction of calibration curves for each sensor and dose, in which the true temperature is assigned to the resistance or voltage value of the sensor. These curves are then compared between the doses for every sensor and should reveal any deviations, caused by the radiation. A LabView program was written to automatize the construction routine and include the following steps.

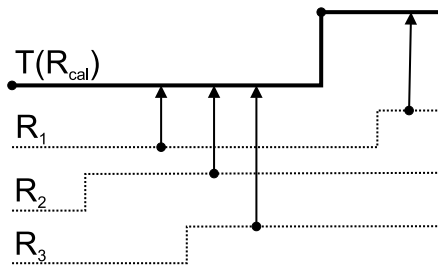


**Fig. 7.6** – Matching procedure for the temperature sensors, in relation to the calibrated RuO-resistor.

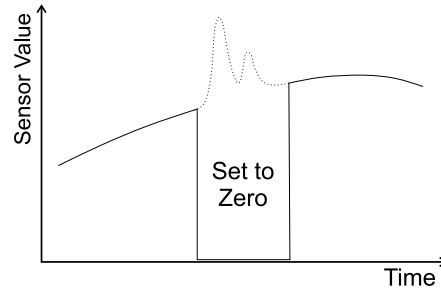


**Fig. 7.7** – Excluding fast changes in temperature, in order to minimize wrong temperature matching.

### 7.3.1 Construction of the Temperature Curves

Due to the serial measurement of the AVS, the resistors cannot be read simultaneously. Therefore, the values of the sensors have to be assigned to the temperature, which indicates the calibrated sensor up to its next measurement, see Fig. 7.6. To avoid major errors, the change in temperature per time must be kept small, otherwise each sensor sees a different temperature and the values are mismatched. However, fast changes in temperature are not preventable during the refrigerator cool-down. But these parts can be 'cut' out in the program and set to zero, like demonstrated in Fig. 7.7. Such a modified curve works as a calibration, which is the basis for the temperature mapping of the other sensors.

For the next step, the sensors are compared to the calibration data over the time-stamp information. All values are set to the true temperature, which are measured in the same time between two measuring points of the calibrated sensor. In a cut-out area of the calibration data, the sensors are also assigned to zero. These zero values are filtered out in the program, afterward. It may happen, that for the same temperature more than just one value is stored in the corresponding array. These values may also be different from each other and in this case, an average value is calculated for each entry with the same temperature. The result is a detailed characteristic curve of the sensor, depending on the temperature.

### 7.3.2 Behavior of the Resistors

The RX-102A sensor has a base resistance of about  $1\text{k}\Omega$  at room temperature and a negative temperature coefficient. This means, while the temperature is dropping down, the resistance rises. This behavior is steady, but accelerating at lower temperatures. Therefore, the most sensitive range is below 1 K, but above 40 K, the sensor is more or less useless due to its small change in temperature. This characteristic is well shown in Fig. 7.8, but only the interesting ranges of the sensors are plotted – below 2 K, and a close-up view below 500 mK, where the major changes take place. The black points represent the measurement without irradiation, the red points after 100 Gy and the blue points at the final dose for each sensor. Notable is, that no significant changes in the resistances between the irradiations are visible and even at 20 kGy, sensor R3 seems to behave in the same way as before. These measurements have shown, that the high radiation dose up to 20 kGy does

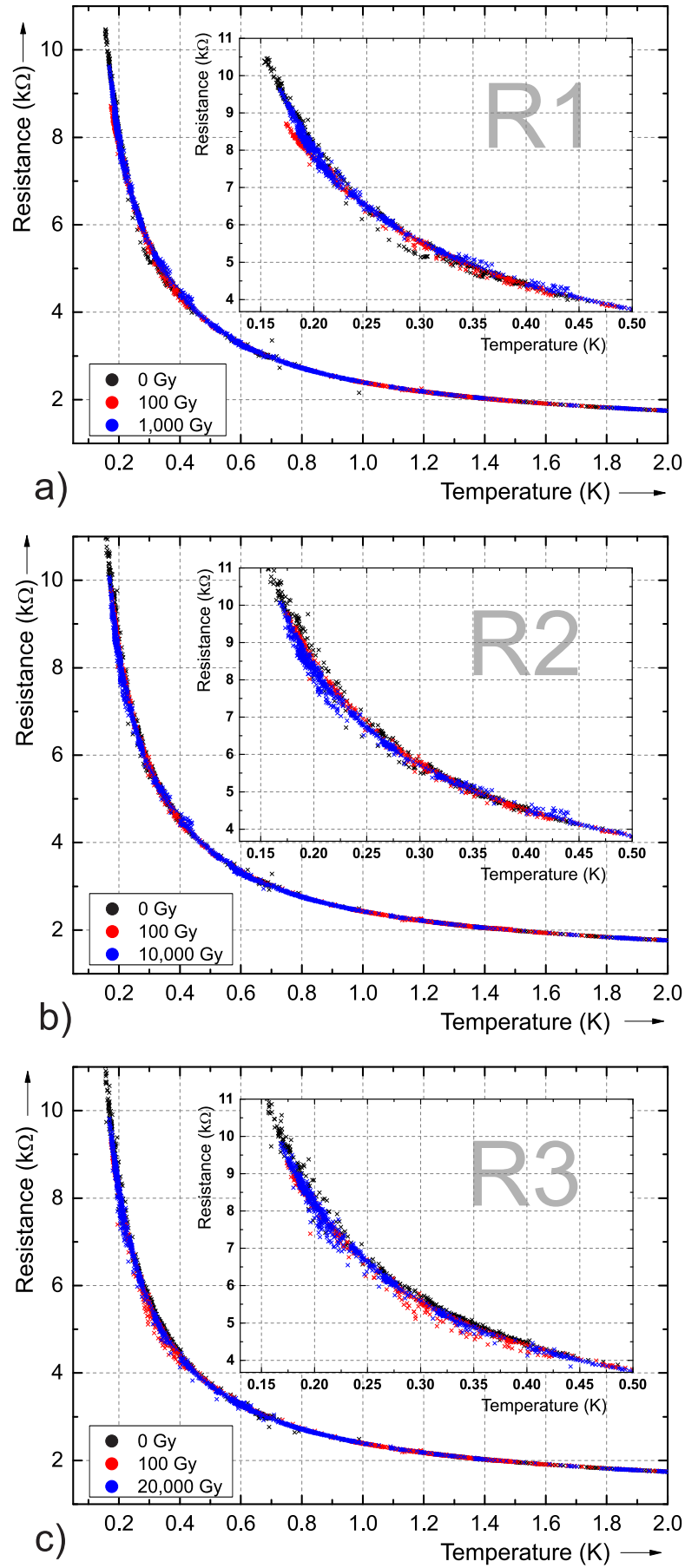


**Fig. 7.8** — Behavior of the RuO-resistors, up to a radiation dose of 20,000 Gy.



not cause any permanent problems for the RuO-resistors, and they can still be used for a reliable temperature measurements and as a support for the Baratron gauge, during the TE-calibration. For the estimation of the uncertainty, all three curves are combined for each resistor. For every step of  $100\ \Omega$ , a  $20\ \Omega$  bin is set, in which the corresponding temperatures are averaged and the mean value, as well as the standard deviation are calculated. As an example, the relative statistical deviation of sensor R3 is shown in Fig. 7.9 and in the usual range for the TE-calibration (1 K to 1.5 K), the relative error does not pass over 1 %. At lower temperatures, the error becomes bigger and gathers around 2-3 %. These values are in full accordance with the measured errors at COMPASS, for this sensor type [78].

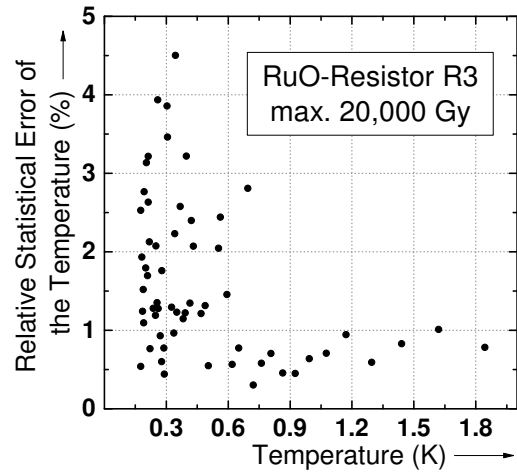


**Fig. 7.9** – Estimation of the statistical error of the RuO-resistor, depending on the measured temperature.

In addition to the statistical error, a deviation caused by the magnetic field has to be included. These sensors are influenced by the magnetic field in a way, that the resistors measure a higher resistance, when the field is on. This elevation is proportional to the magnetic field strength and at 2.5 T/1 K, a deviation of about 1 % were detected from the initial value<sup>11</sup>. This variation corresponds to an uncertainty of approximately 3 % in the temperature, due to the conversion process of  $\Omega \Leftrightarrow K$ . For the used RuO-resistors at COMPASS, an uncertainty in temperature of 1.5 % is specified at a field of 2 T. At 50 mK, the error is only about 1 mK, caused by the magnetic field [78].

### 7.3.3 Behavior of the Diodes

For the diodes DT-670, the company specified a temperature range from 1.4 K to 500 K, which covers a voltage up to approximately 1.65 V. However, the modification of the THMP allows only a measurement up to 90 K. Since the calibration of the RuO-resistors is only verified up to 40 K, the characteristic curves of the diodes can also be given only up to 40 K. Contrary to the information provided by the company, the diodes show a sufficient dependancy for the temperature determination below 1.4 K. This is of course strongly linked to the possible resolution of the measured voltage. According to the modifications in section 7.1.2, the THMP has a resolution of  $2.441 \times 10^{-4}$  V. Nevertheless, the diodes are not a good choice for a measurement in the region below 1 K, see Fig. 7.11. In this region, the slope falls rapidly and is practically zero at 300 mK.

The purpose of these diodes is monitoring the cool-down process within the COMPASS refrigerator. For example, Fig. 5.15 shows the diode sensor TTH8, which logs the temperature of the mixing chamber during the target loading. The characteristic of the

<sup>11</sup>These measurements were done with RuO-resistors, but not with those, which were exposed to ionizing radiation.



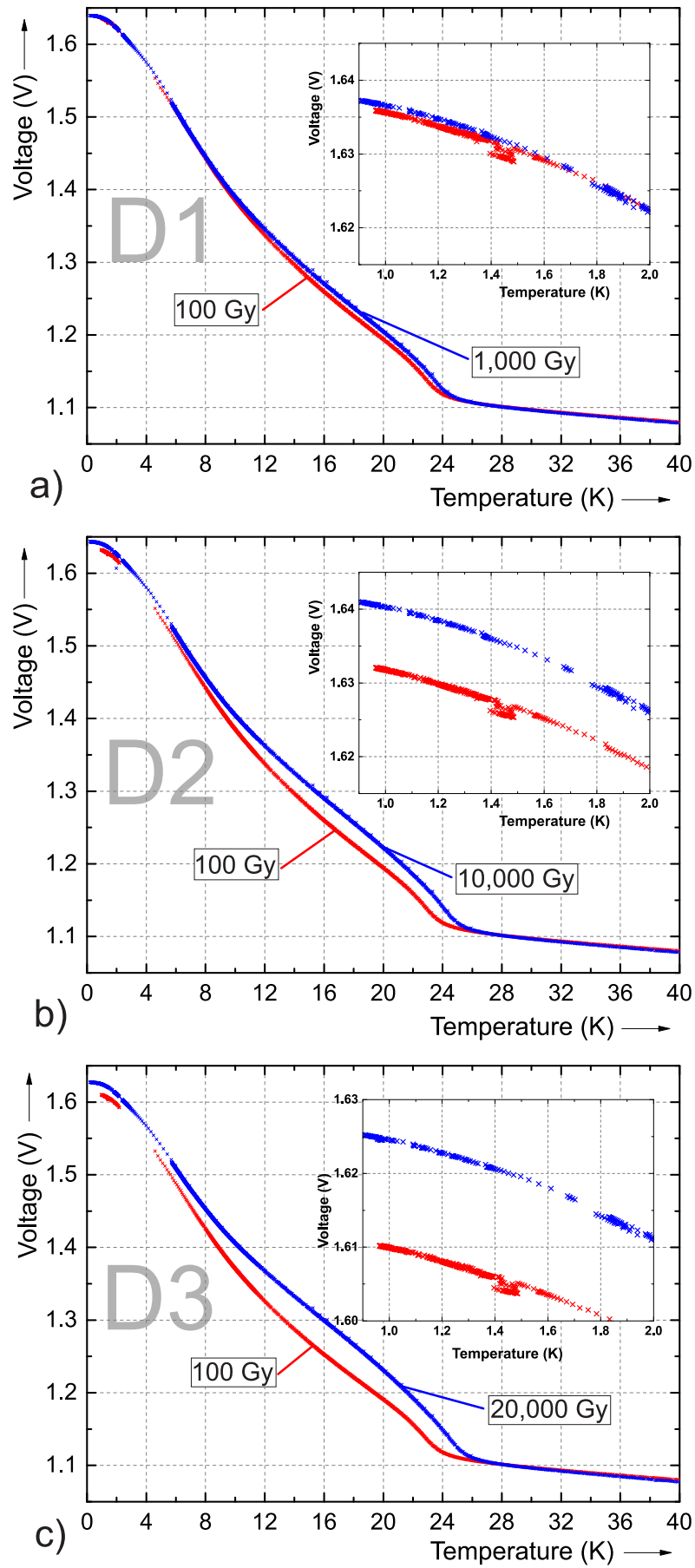


**Fig. 7.10** — Behavior of the silicon diodes, up to a radiation dose of 20,000 Gy.

diodes differs significantly from that of the resistors. Down to 26 K, the diodes show a more or less a linear behavior. At lower temperatures, the slope rises from approximately 2 mV/K up to 35 mV/K until 5 K, at which the slope drops down and goes to zero. Therefore, the most sensitive region of the diodes lies between 2 K and 24 K. A first look on the figures reveals, that the diodes are strongly affected by the radiation. This effect is cumulative, which is well shown in Fig. 7.10. The strongest deviations are also in the most sensitive region, but not only a shift of the curves can be seen, also the shape has slightly changed. In general, the curves move toward higher temperatures, while at 1 kGy the change looks even small, it already reaches up to 5 % in the sensitive region and up to 20 % in the range of 1 K. The shifts for 10 kGy and 20 kGy are much more serious and lead to deviations of up to 20 % in the sensitive region. Around 1 K the deviation reaches even 100 %, which would be crucial, if the diodes were used in the TE-calibration. Like mentioned before, the vapor pressure of helium is used for this purpose and the RuO<sub>3</sub>-resistors, if necessary. For temperatures above 26 K, almost no change is visible. Therefore, the diodes can be still used to measure higher temperatures, as in the coll-down process of the refrigerator.

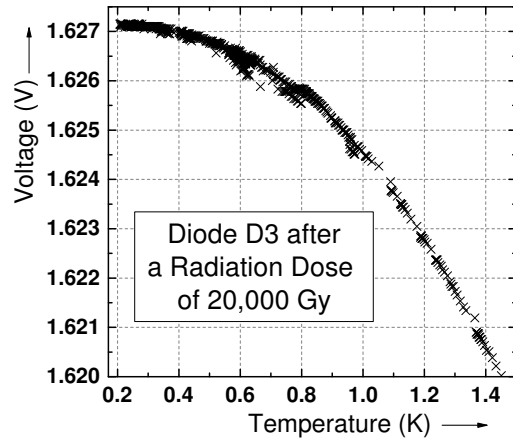


**Fig. 7.11** — A close-up of the temperature dependence of D3 below 1.4 K.

## Summary

These measurements have shown, that the radiation may have a great impact on the temperature measurement. Positively should be noted, that the resistors have shown no change up to 20 kGy – the order of the expected radiation dose in a year at COMPASS II. The reaction of the diodes instead is more critical. Large variations in the temperature measurement should be expected, especially in the lower temperature region. But since the diodes are only used in the cooling process and the measured values taking no part in any calculations, they still can be used as guiding values during the cool-down process.

## Conclusion

In the target business, ammonia is a very good probe for studying the properties of the proton spin. Since the first experiments in the 1970s and the discovery of the best way to dope ammonia with paramagnetic centers through irradiation a decade later, ammonia has evolved to a standard material for polarized targets. Besides a high dilution factor, ammonia is characterized through a very good radiation hardness, which was researched extensively in the 1980s.

After the COMPASS experiment has started in 2002, ammonia was not used anymore as a target until 2007 and then, the material was taken from the predecessor experiment SMC, which was produced in 1995. In 2010, the target material was already 15 years old and showed signs of aging, such as a long build-up time and a lower average maximum polarization. For this reason, the decision was made to produce fresh target material, which was realized in a collaboration between the polarized target groups of Bonn and Bochum, in 2011. As a consequence of the irradiation, the ammonia beads became strongly purple colored, which is caused through the produced of F-centers. This color disappears over time and is an indication for a recent irradiation. The difference to chemical doped targets is the absence of a control over the produced paramagnetic centers (defects), and mostly not restricted to just one kind of radicals, see Fig. 3.4. Thus, all of these paramagnetic centers may be somehow involved in the polarization behavior, as it is demonstrated in section 3.4. Radicals are produced, which are stable only at ultra-low temperatures and reduce the maximum polarization at a certain dose of radiation.

The first polarization measurements with the new material has shown a surprisingly short relaxation time of about one minute, and also short build-up times. These times even undercut the times, that were measured shortly after irradiation in the 1980s. In addition to that, the relaxation shows a behavior, which cannot be described properly with a single exponential function. For a sufficient characterization, at least two exponential functions are necessary, with a fast and slow time constant. This behavior could already be observed in early measurements and this suggests, that at least two relaxation channels are dominating the decay process of the polarization. The EPR-spectrum of irradiated ammonia shows the resonances of two radicals in the first place, the  $\dot{\text{H}}$  and the  $\dot{\text{N}}\text{H}_2$  radical. The latter is used for the polarization build-up of the nuclei during the DNP, whereas the  $\dot{\text{H}}$  radical takes no part in the build-up process. Nevertheless, both centers

contribute to the relaxation, which is moderated by the spin-diffusion and could be an explanation for the unusual behavior of the relaxation curve. In Fig. 5.3a, a drop of the associated concentration can be seen in a short period of 100 days after the irradiation and afterward, the concentration remains almost constant. Since the  $\dot{\text{N}}\text{H}_2$  radicals are quite stable at the temperature of liquid nitrogen and the decrease is consistent with the color loss of ammonia, the drop might indicate the loss of the F-centers. These centers have also a paramagnetic character and should be at the same position as the  $\dot{\text{N}}\text{H}_2$  resonance. In contrast to that, the concentration of the  $\dot{\text{H}}$  radicals decrease slowly but steady, as Fig. 5.3b shows. These changes may have an impact on the long-term behavior of the target material, such as the build-up and relaxation times as well as the maximum polarization. And indeed, the build-up time rises with the duration of storage, see Fig. 5.11. However, after one year, the variance of the values is so big, that no proper conclusion can be given for the future course, but this behavior coincides with the color loss of ammonia and thus, the F-centers. One argument for this could be the location of the F-center resonance, which is superimposed with the  $\dot{\text{N}}\text{H}_2$  resonance, and therefore should also support the DNP process.

The interpretation of the relaxation curves is more difficult, due to their peculiar relaxation behavior. With a single exponential fit, a trend towards larger relaxation times can be seen, but by using more exponential functions, no clear tendency is visible anymore, even though the polarization decay is described in a better way. A change of the maximum polarization could also not be observed.

In 2011 at COMPASS, the new material showed an improvement of the average maximum polarization to  $\sim 85\%$  as well as a faster build-up time, in contrast to the older material (15 years after the irradiation), see Tab. 5.1. For the DY-measurement, the material of 2011 is still used, but several changes had to be applied to the detector setup and the target system. The number of cells had to be reduced to two and a different base material should be used, since the particle beam is changed to a hadron beam, with the expectation of a higher radiation level. The decision was made in favor for PCTFE, which has in addition to the good radiation hardness, more mechanical and thermal advantages compared to the previously used net cell. Moreover, PCTFE is free of hydrogen, which is optimal for proton targets (the proton of hydrogen), in order to minimize systematic errors through a background signal.

Not only the target material and the cells are directly exposed to the beam, also the temperature sensors are affected, which are mounted at various positions of the target cells. Two different sensor types are used to measure the temperature, RuO-resistors for the sub-kelvin range and silicon diodes for temperatures above 1 K. Both sensor types were exposed to different radiation doses, up to 20 kGy and measured in a dilution refrigerator in Bochum. The conclusion is, that the RuO-resistors are quite radiation hard, at least up to a dose of 20 kGy and they show no sign of a change from their initial behavior, see Fig. 7.8. Therefore, the resistors can still be used to measure the temperature.

This is different for the silicon diodes, which show a cumulative effect, resulting into a larger deviation at higher radiation doses, see Fig. 7.10. Especially the range below

26 K is strongly affected by the radiation, with deviations up to 20 % at a dose of 20 kGy. It is not recommended to use these sensors for a reliable temperature measurement, for example during the TE-calibration. However, the diodes can still be used for the higher temperature range, since no change can be seen in this region.

In this work, the way of how ammonia became a polarizable target is reviewed, from the production process to the application in an experiment. Here, the long-term behavior of the nuclear polarization and the paramagnetic centers was observed, which was done for the most common variation of ammonia,  $^{14}\text{NH}_3$ . Other derivatives of ammonia could not be investigated, due to shipping problems and other technical issues with the linear accelerator at ELSA. However, these derivatives are already treated in several publications like [29, 35, 48].

Another interesting subject is the production of ultra-low temperature radicals, which are evading at later measurements in an EPR spectrometer. For this matter, an EPR-measurement must be performed right after a low temperature irradiation, best within the very same refrigerator, without the risk of losing the produced radicals. J. HECKMANN has already taken a step in this direction, with the development of an EPR-measurement at polarization conditions [17].

Nevertheless, the new produced ammonia material has shown several improvements in the polarization at COMPASS and with that, it has helped to increase the statistics of the experiment. The new target cell should simplify the handling of the target and reduce systematic errors, due to its hydrogen-free structure.



# Appendices







## Ammonia Behavior Studies

### A.1 Irradiation of Ammonia

The duration of the irradiation sessions were in the range of 9 h to 14 h, usually performed during the night. In total, 11 irradiation sessions were organized between January and March 2011, whereas the last two irradiation sessions failed and the samples were accidentally destroyed.

**Tab. A.1** — Overview of the irradiation sessions at ELSA. Radical concentrations were taken from [43].

Session Number of Irradiation	Irradiation Date (2011)	Radical Concentration ( $\times 10^{19}$ Spins/g)
1	19./20. Jan.	$4.16 \pm 0.07$
2	25./26. Jan.	$4.08 \pm 0.06$
3	31. Jan / 1. Feb.	$4.10 \pm 0.06$
4	8./9. Feb.	$4.16 \pm 0.07$
5	15./16. Feb.	$4.43 \pm 0.07$
6	17. Feb.	$4.16 \pm 0.18$
7	22./23. Feb.	$4.17 \pm 0.06$
8	28. Feb. / 1. Mar.	$4.48 \pm 0.06$
9	9./10. Mar.	$4.51 \pm 0.07$
10	16./17. Mar.	Material destroyed
11	28./29. Mar.	Material destroyed

### A.2 Addendum to the Long-term Behavior of the Ammonia

#### A.2.1 Paramagnetic Centers

First, the DPPH resonances were measured and used to form calibration factors, in order to cancel out the influence of the different sample-Dewar. Table A.2 shows the data for the long-term trend of the paramagnetic centers in fresh ammonia.

**Tab. A.2** – EPR data of the long-term behavior of the paramagnetic centers in fresh irradiated ammonia, according to Fig. 5.3.

Days after Irradiation	Area of $\dot{\text{N}}\text{H}_2$ Resonance	Area of $\dot{\text{H}}$ Resonance	Calibration Factor from DPPH	Area of $\dot{\text{N}}\text{H}_2$ Resonance Corr.	Area of $\dot{\text{H}}$ Resonance Corr.	Ratio of $\dot{\text{H}}/\dot{\text{N}}\text{H}_2$ ( $\times 10^{-3}$ )
7	82.52 $\pm$ 3.88	0.577 $\pm$ 0.050	1.00 $\pm$ 0.02	82.52 $\pm$ 4.22	0.577 $\pm$ 0.052	6.99 $\pm$ 0.69
13	60.96 $\pm$ 2.26	0.488 $\pm$ 0.038	0.98 $\pm$ 0.02	59.54 $\pm$ 2.52	0.477 $\pm$ 0.038	8.00 $\pm$ 0.68
23	24.24 $\pm$ 1.14	0.261 $\pm$ 0.023	2.11 $\pm$ 0.04	51.07 $\pm$ 2.59	0.550 $\pm$ 0.049	10.77 $\pm$ 1.06
36	51.18 $\pm$ 1.89	0.170 $\pm$ 0.013	1.51 $\pm$ 0.02	77.52 $\pm$ 3.05	0.257 $\pm$ 0.020	3.31 $\pm$ 0.28
43	48.81 $\pm$ 1.81	0.483 $\pm$ 0.037	1.11 $\pm$ 0.02	54.35 $\pm$ 2.24	0.538 $\pm$ 0.043	9.90 $\pm$ 0.85
197	51.93 $\pm$ 1.92	0.411 $\pm$ 0.032	1.06 $\pm$ 0.02	55.16 $\pm$ 2.29	0.437 $\pm$ 0.035	7.91 $\pm$ 0.68
226	43.09 $\pm$ 2.03	0.305 $\pm$ 0.027	1.12 $\pm$ 0.03	48.19 $\pm$ 2.57	0.341 $\pm$ 0.031	7.08 $\pm$ 0.70
254	45.83 $\pm$ 1.70	0.338 $\pm$ 0.026	1.07 $\pm$ 0.02	49.17 $\pm$ 2.04	0.363 $\pm$ 0.029	7.37 $\pm$ 0.63
372	37.43 $\pm$ 2.13	0.288 $\pm$ 0.028	1.46 $\pm$ 0.02	54.76 $\pm$ 3.25	0.421 $\pm$ 0.041	7.69 $\pm$ 0.87
380	37.15 $\pm$ 1.75	0.245 $\pm$ 0.021	1.41 $\pm$ 0.02	52.29 $\pm$ 2.53	0.345 $\pm$ 0.030	6.60 $\pm$ 0.65
386	45.93 $\pm$ 1.70	0.257 $\pm$ 0.020	1.18 $\pm$ 0.01	54.21 $\pm$ 2.08	0.303 $\pm$ 0.024	5.60 $\pm$ 0.48
393	49.10 $\pm$ 2.31	0.258 $\pm$ 0.022	1.21 $\pm$ 0.01	59.55 $\pm$ 2.86	0.313 $\pm$ 0.027	5.25 $\pm$ 0.52
395	48.78 $\pm$ 1.81	0.285 $\pm$ 0.022	1.17 $\pm$ 0.02	57.04 $\pm$ 2.25	0.333 $\pm$ 0.026	5.84 $\pm$ 0.50
405	46.44 $\pm$ 1.72	0.253 $\pm$ 0.019	1.17 $\pm$ 0.02	54.20 $\pm$ 2.21	0.295 $\pm$ 0.023	5.45 $\pm$ 0.47
412	45.58 $\pm$ 2.14	0.247 $\pm$ 0.021	1.39 $\pm$ 0.02	63.13 $\pm$ 3.01	0.342 $\pm$ 0.030	5.42 $\pm$ 0.54
420	42.16 $\pm$ 1.56	0.222 $\pm$ 0.017	1.28 $\pm$ 0.02	53.86 $\pm$ 2.16	0.284 $\pm$ 0.022	5.27 $\pm$ 0.45
422	47.57 $\pm$ 1.76	0.209 $\pm$ 0.016	1.31 $\pm$ 0.02	62.15 $\pm$ 2.42	0.273 $\pm$ 0.021	4.39 $\pm$ 0.38
433	44.74 $\pm$ 2.10	0.225 $\pm$ 0.020	1.29 $\pm$ 0.02	57.82 $\pm$ 2.92	0.291 $\pm$ 0.026	5.03 $\pm$ 0.50
435	36.44 $\pm$ 1.35	0.229 $\pm$ 0.018	1.58 $\pm$ 0.03	57.48 $\pm$ 2.36	0.361 $\pm$ 0.029	6.28 $\pm$ 0.54
594	32.72 $\pm$ 1.21	0.158 $\pm$ 0.012	1.29 $\pm$ 0.02	42.23 $\pm$ 1.69	0.204 $\pm$ 0.016	4.83 $\pm$ 0.41
603	40.64 $\pm$ 2.32	0.171 $\pm$ 0.017	1.35 $\pm$ 0.02	54.68 $\pm$ 3.22	0.230 $\pm$ 0.023	4.21 $\pm$ 0.47

### A.2.2 Radical Concentration

The radical concentration were estimated, using a calibration sample of a known radical concentration – a mixture of butanol with TEMPO. By measuring the area of the integrated resonance signal and the weight of both samples (butanol-mix and ammonia), the radical concentration of the irradiated ammonia can be easily determined, using (2.46).

**Tab. A.3** – Long-term trend of the radical concentration of irradiated ammonia, according to Fig. 5.4.

Month after Irradiation	Radical Concentration ( $\times 10^{19}$ Spins/g)	
	Session 1	Session 2
0.23	4.16 $\pm$ 0.06	–
0.46	–	4.08 $\pm$ 0.06
5.93	3.57 $\pm$ 0.20	–
13.70	2.33 $\pm$ 0.24	2.45 $\pm$ 0.24
50.20	2.08 $\pm$ 0.38	–

### A.2.3 Relaxation Behavior

Several polarization and relaxation passages were performed and the integrated areas of the hydrogen resonances were stored in a file. Figure A.1 shows a screenshot of the programmed LabView routine, in which each relaxation curve can be extracted from the whole measurement file and is analyzed with the three fitting methods, which are described in section 5.2.1.

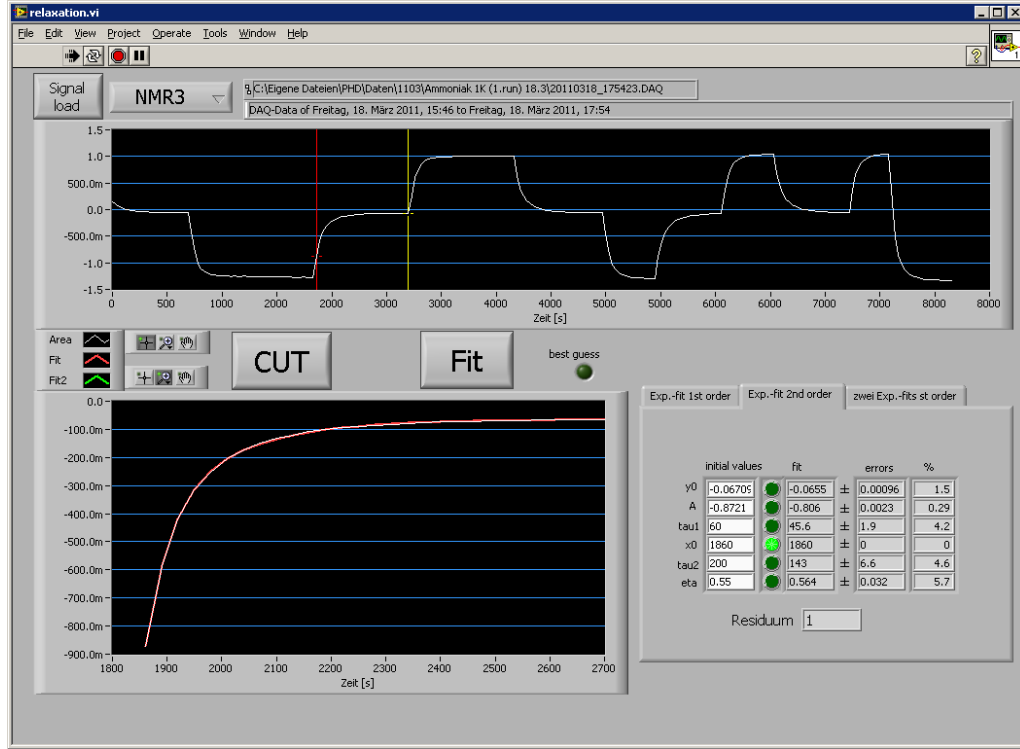


Fig. A.1 — Frontpanel of the relaxation fitting-program.

### Build-Up and Relaxation Times of Ammonia

Tab. A.4 — Summary of the build-up and relaxation results for the long-term measurement. This table corresponds to Fig. 5.12.

Month after Irradiation	Build-up Time (s)	Relaxation				
		One Exp. Function $\tau$ (s)	Mixed Exp. Function		Two Exp. Function	
			fast $\tau_1$ (s)	slow $\tau_2$ (s)	fast $\tau_1$ (s)	slow $\tau_2$ (s)
0.13	35.6 ± 5.6	60.1 ± 4.8	38.8 ± 3.5	166.8 ± 20.5	44.6 ± 2.7	123.3 ± 10.9
0.43	49.8 ± 11.6	81.2 ± 6.3	38.1 ± 7.9	127.3 ± 15.8	56.2 ± 3.9	116.0 ± 7.1
1.87	60.5 ± 3.7	80.1 ± 3.4	45.0 ± 2.5	142.0 ± 7.0	59.3 ± 2.8	120.5 ± 5.3
4.79	58.6 ± 13.0	73.1 ± 8.5	39.7 ± 11.0	129.3 ± 51.3	57.8 ± 6.2	106.4 ± 22.6
5.41	68.7 ± 5.8	108.3 ± 7.4	49.5 ± 2.4	298.3 ± 19.2	55.1 ± 4.4	249.7 ± 24.5
10.10	68.3 ± 2.0	95.2 ± 5.9	41.8 ± 3.9	206.7 ± 34.0	54.6 ± 2.1	180.0 ± 23.0
12.59	60.3 ± 2.2	93.2 ± 7.9	41.0 ± 3.2	158.8 ± 14.0	55.3 ± 4.6	145.5 ± 14.4
16.69	87.2 ± 5.0	113.3 ± 5.9	42.3 ± 2.8	178.3 ± 11.0	58.8 ± 4.4	161.0 ± 5.8
27.08	59.3 ± 5.9	77.0 ± 6.1	40.0 ± 2.9	127.5 ± 9.6	55.2 ± 3.5	116.0 ± 7.7
30.72	93.1 ± 15.3	137.3 ± 19.0	55.5 ± 6.9	241.5 ± 33.1	71.1 ± 5.9	207.5 ± 23.2
34.39	—	115.5 ± 9.8	75.5 ± 35.5	235.5 ± 66.1	102.0 ± 3.1	132.0 ± 32.2
43.77	79.4 ± 3.7	117.3 ± 14.7	55.7 ± 5.6	233.3 ± 16.2	66.1 ± 5.7	193.3 ± 18.9

### A.3 Overview of Polarization at COMPASS

The polarization of the COMPASS target was measured with 10 NMR coils in the pattern 3–4–3 (up/central/down). The polarization of a cell is estimated by averaging the measured value of the respective coils. The following figures show the average polarization over the entire experiment run at COMPASS for 2007, 2010 and 2011. These data were taken from the SVN repository of the COMPASS polarized target at CERN (<https://svnweb.cern.ch/cern/wsvn/ptpolaris>). The cells were differently polarized and the polarization direction was frequently reversed in each cell.

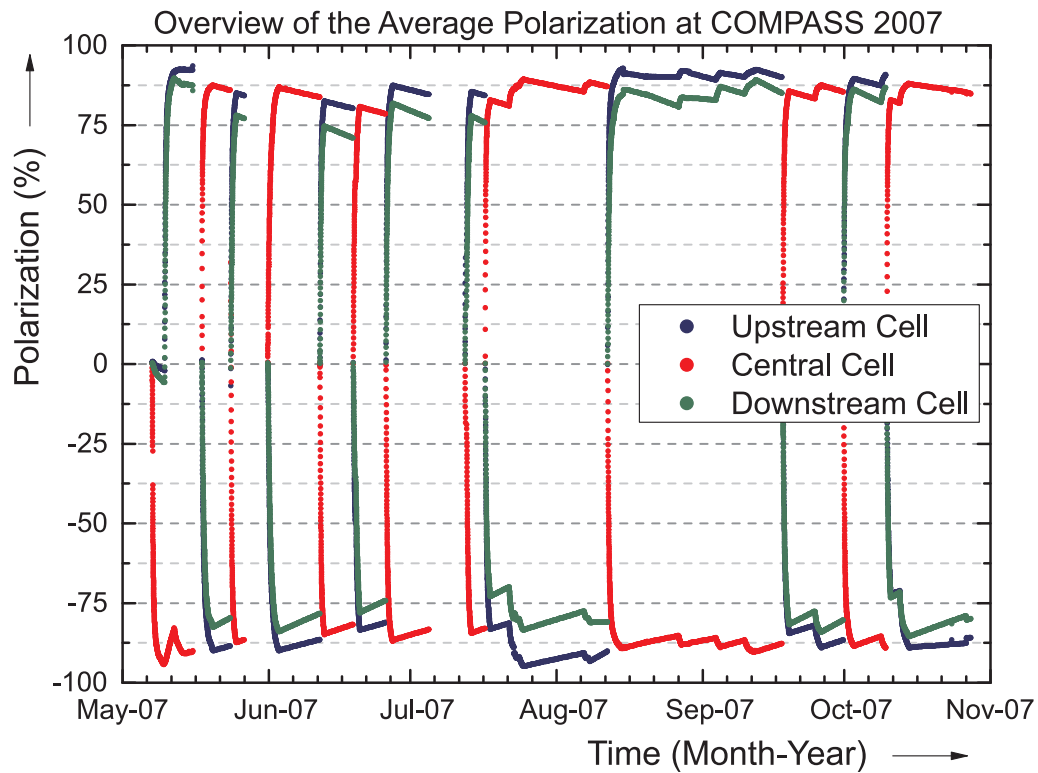


**Fig. A.2** — Overview of the average polarization at COMPASS for 2007.

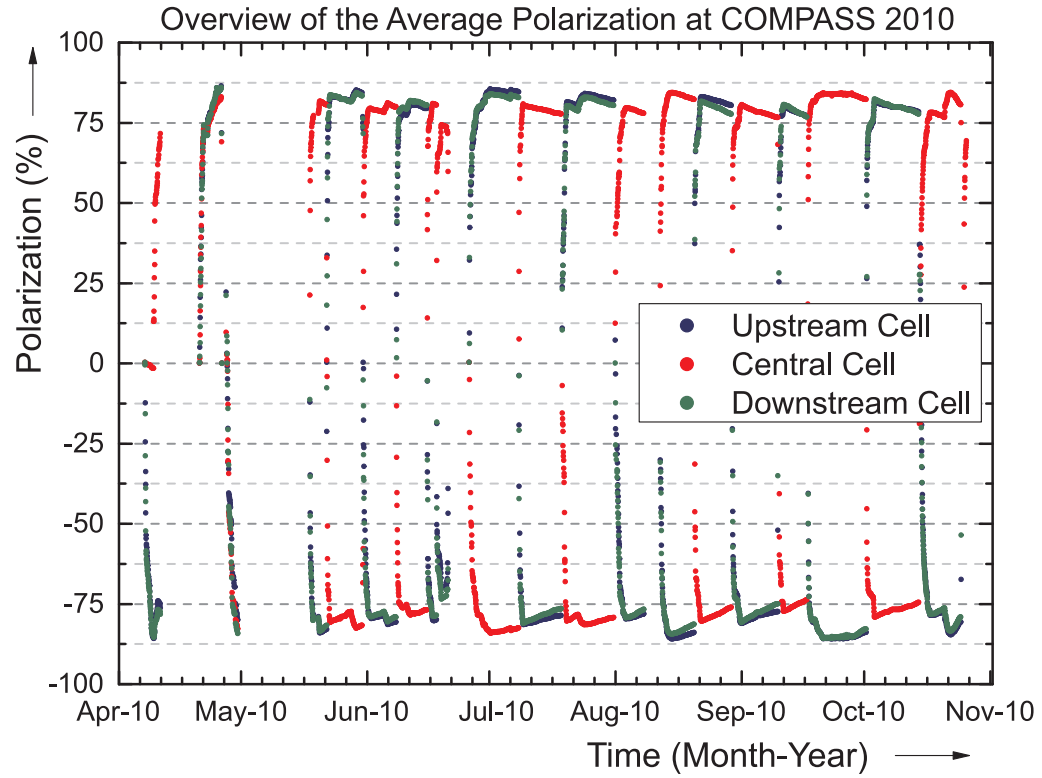


**Fig. A.3** — Overview of the average polarization at COMPASS for 2010.

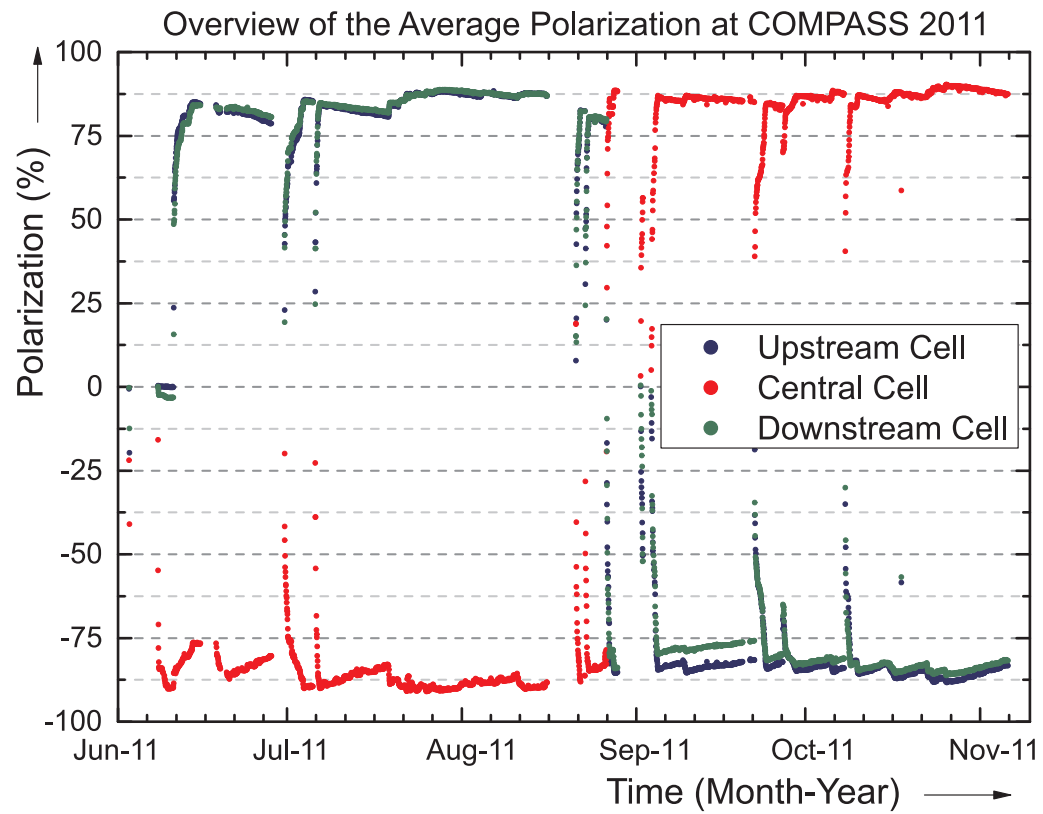


**Fig. A.4** — Overview of the average polarization at COMPASS for 2011.



## Target Cell

Several target cell designs were used during the last 30 years, and an overview is given in Fig. 6.7, as well as in the associated Tab. B.1, in which the dimensions of these cells are written down.

**Tab. B.1** — Specifications of the past target cells at the COMPASS experiment and its predecessors.

Experiment / year [ref]	Number of Cells	Length (mm)	Diameter (mm)	Total Volume (L)	Gap (mm)
<b>EMC</b> / mid 1980s [74]	2	360 / 360	60*	2	220
<b>SMC</b> / 1993 – 1996 [75]	2	600 / 600	50	2.556	300
		650 / 650		2.356	200
<b>COMPASS</b> / 2002 – 2004 [56]	2	600 / 600	30	0.848	100
<b>COMPASS</b> / 2006 [56]	3	300 / 600 / 300	30	0.848	50
<b>COMPASS</b> / 2007 – 2011 [44]	3	300 / 600 / 300	40	1.508	50
<b>COMPASS II</b> / 2014 – 2015 [76]	2	550 / 550	40	1.382	200

\* The cells had no round profile, see Fig. 6.7.

For the new design, a different material was required, which can definitely withstand the radiation exposure in the COMPASS II run 2015. Three materials were tested and irradiated at the Bonn LINAC – FEP, PCTFE and Torlon, see Fig. B.1.

In the end, PCTFE was chosen to be the new material for the target cells and the start specifications of the new design were taken from the drawing in Fig. B.2. From then on, the new design was planned on paper and converted into a CAD-drawing<sup>1</sup>, afterward. The first design steps are pictured in Fig. B.7, in which an attempt is made to include all features into a only-PCTFE construction. It was decided, to realize the target cells in a modular system, which works best for the production process and for possible damages in the future. Figures B.3ff show the technical drawings of the final design version. In addition, a picture of the previous net target is shown in Fig. B.9. In section B.2 the data of the cell shrinkage test is presented.

<sup>1</sup>CAD stands for Computer-Aided Design.

## B.1 Bonn Radiation Test

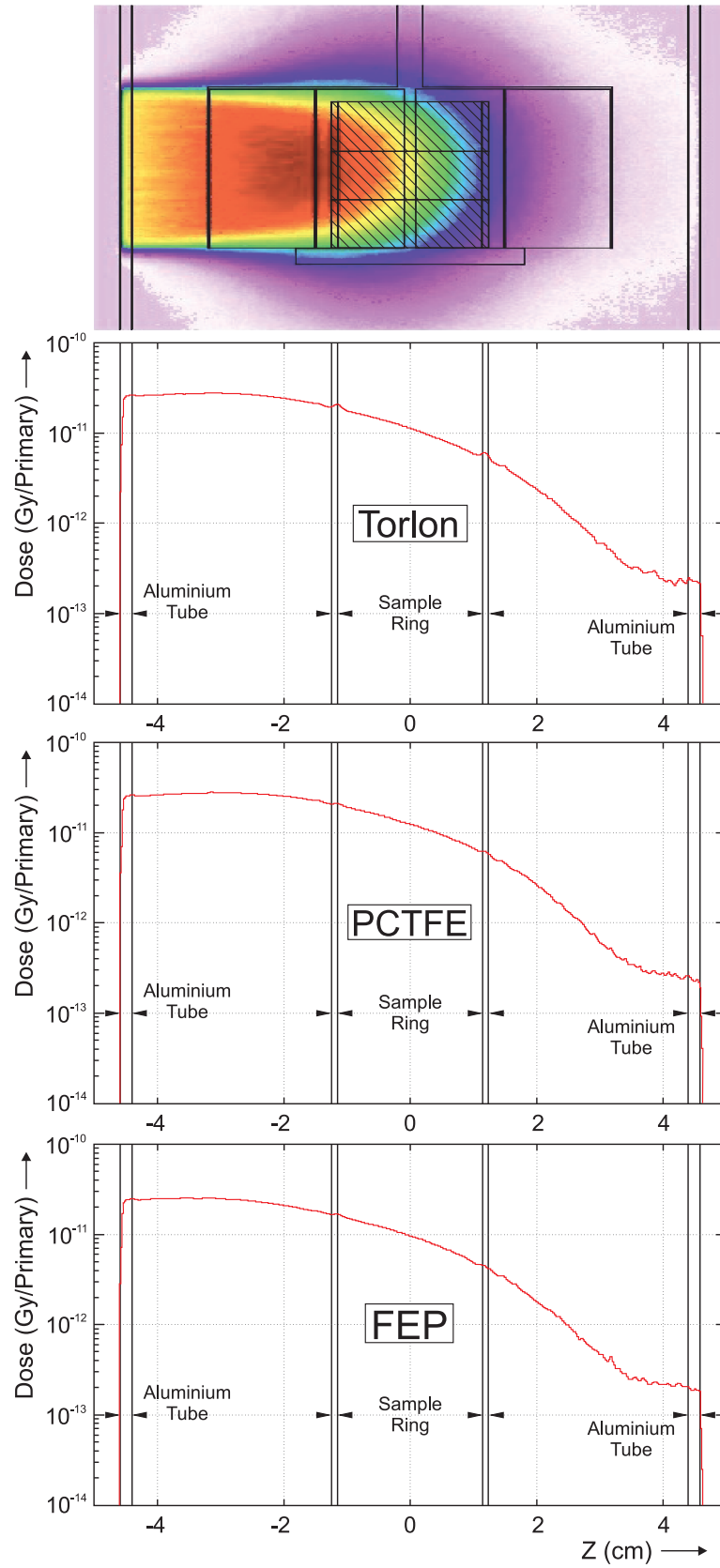
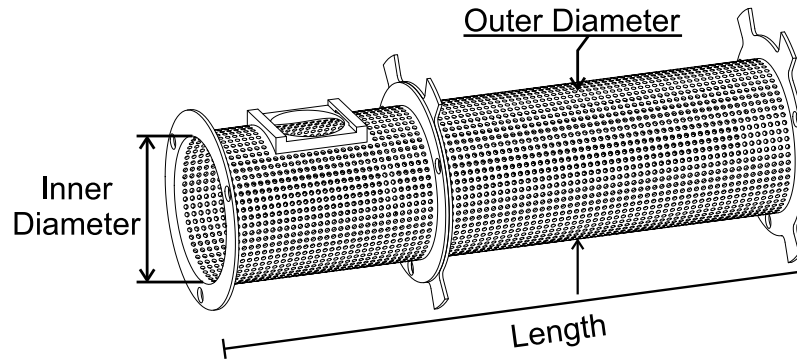


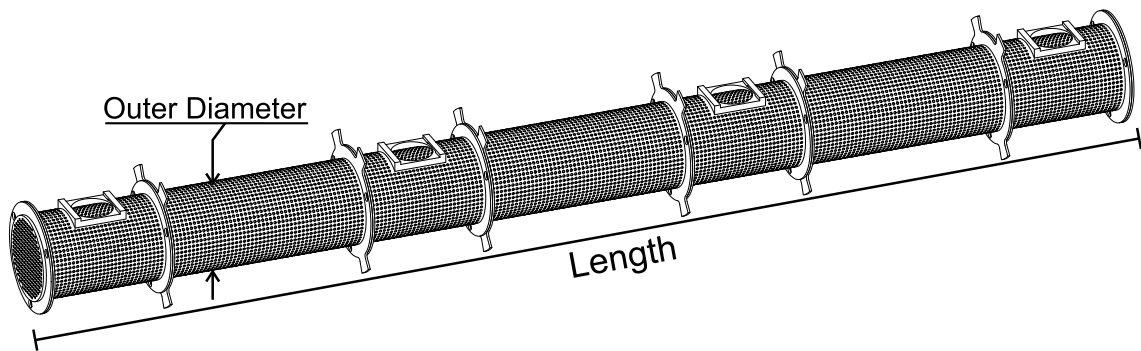
**Fig. B.1** — Detailed results of the Bonn radiation simulation, generated by the group of A. MAGGIORA [65]. Addendum to Fig. 6.1.



## B.2 Target Cell Shrinkage



Dimension (mm)	Warm (25 °C)	Cold (−196 °C)
Length	163.23 / 163.16 / 163.38 / 163.09 / 163.17	161.62 / 161.76 / 161.54 / 161.57 / 161.56
Inner Diameter	39.89 / 39.74 / 39.87 / 40.01 / 40.04	39.63 / 39.43 / 39.50 / 39.66 / 39.46
Outer Diameter	41.36 / 41.11 / 41.32 / 41.19 / 41.32	41.05 / 41.15 / 41.02 / 41.08 / 41.05
<b>Coefficient of Thermal Expansion</b> (weighted average)		
Length	$(4.42 \pm 0.40) \times 10^{-5} \text{ K}^{-1}$	} $(4.21 \pm 0.46) \times 10^{-5} \text{ K}^{-1}$
Inner Diameter	$(2.08 \pm 1.27) \times 10^{-5} \text{ K}^{-1}$	
Outer Diameter	$(4.24 \pm 1.79) \times 10^{-5} \text{ K}^{-1}$	



Dimension (mm)	Warm (22 °C)	Cold (−196 °C)
Length	555.42 / 555.51 / 555.38	551.21 / 550.73 / 550.32 / 550.60 / 550.14
Outer Diameter	41.45 / 41.65 / 41.37	41.00 / 41.05 / 41.15 / 41.18 / 41.05
<b>Coefficient of Thermal Expansion</b> (weighted average)		
Length	$(4.01 \pm 0.36) \times 10^{-5} \text{ K}^{-1}$	} $(4.06 \pm 0.19) \times 10^{-5} \text{ K}^{-1}$
Outer Diameter	$(4.83 \pm 1.47) \times 10^{-5} \text{ K}^{-1}$	

B.3 Technical Drawings

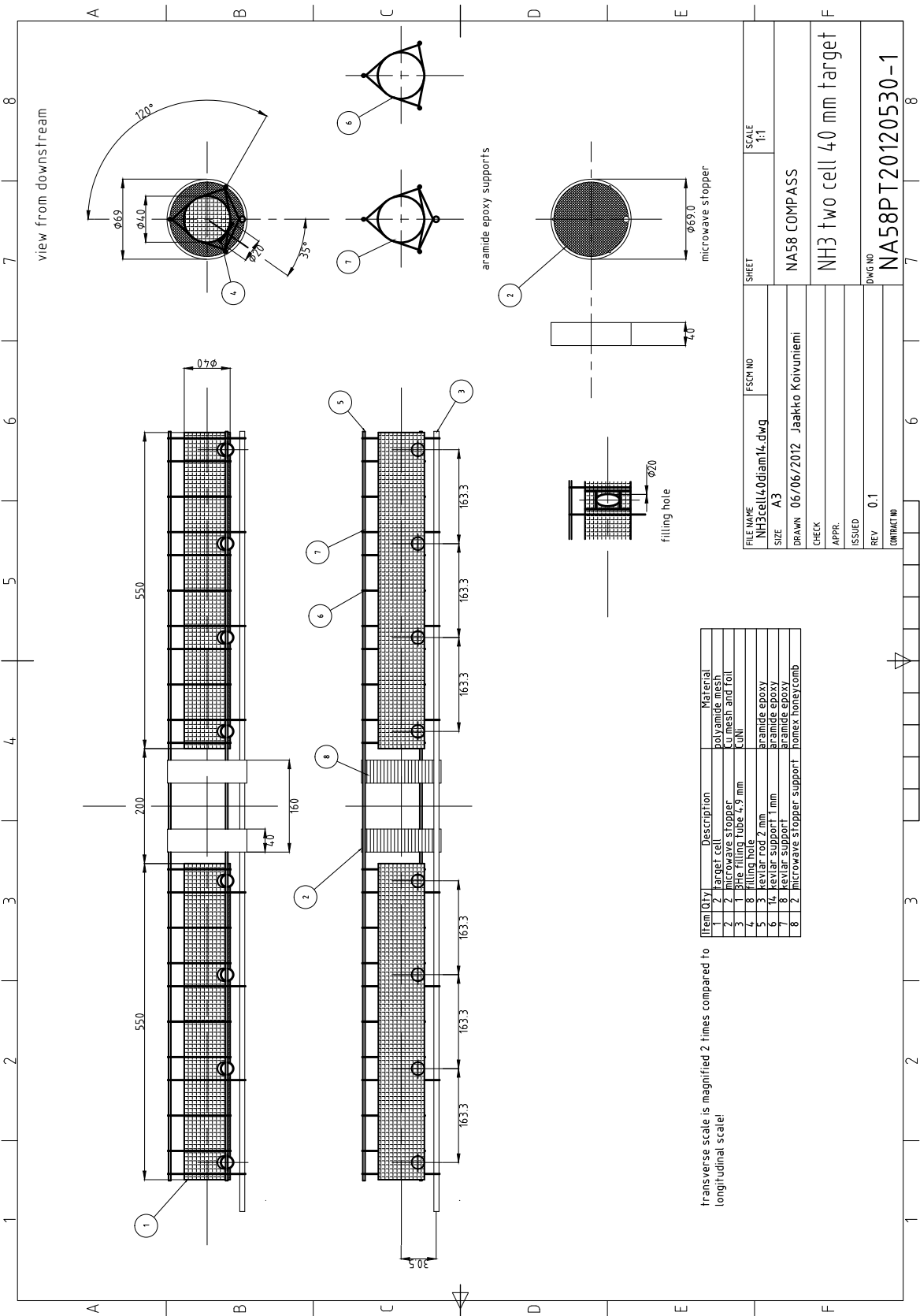


Fig. B.2 – Technical drawing of the net cell for the DY measurement, used for the test measurement in 2014. The starting specifications for the new cell design were taken from this drawing.

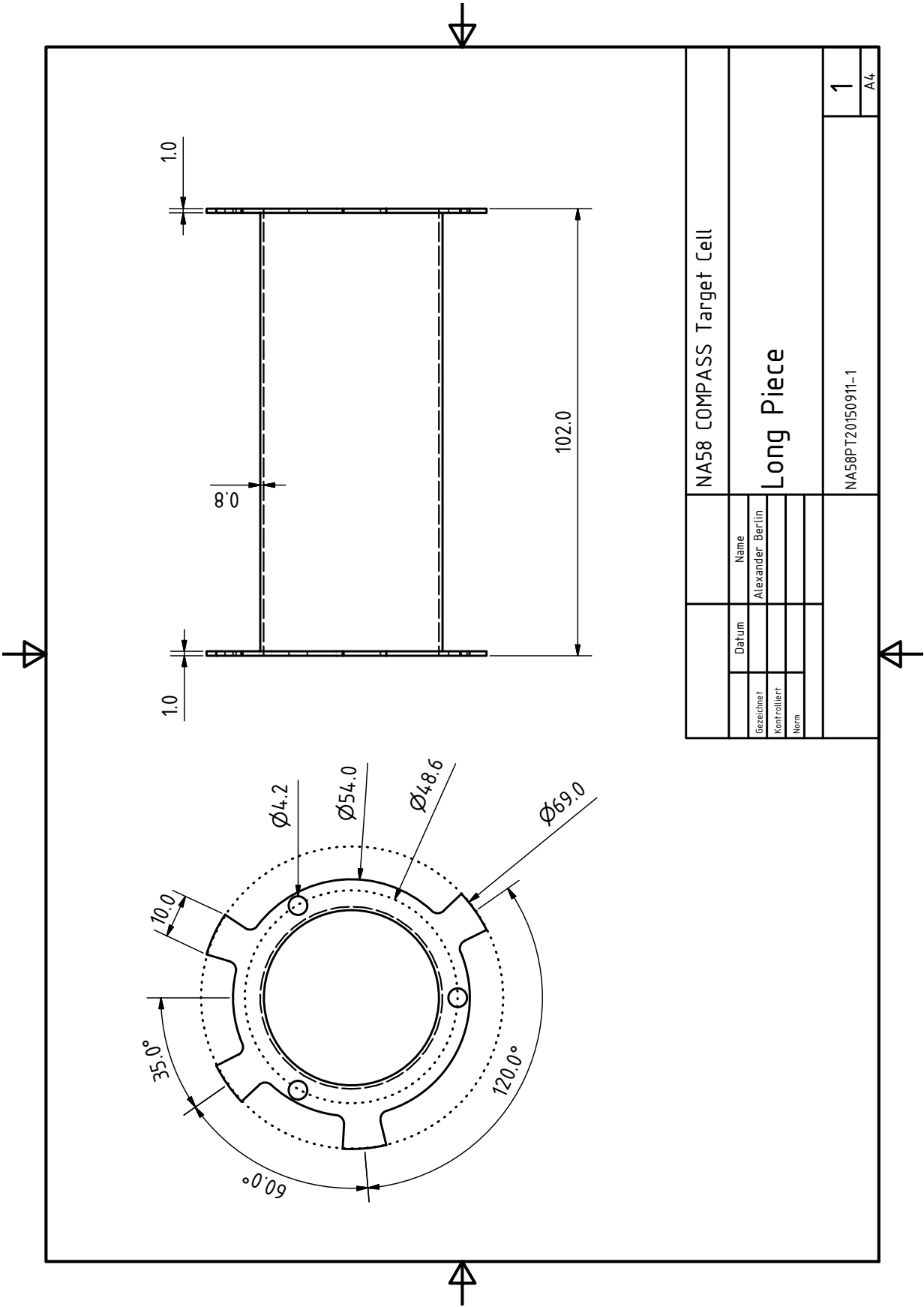


Fig. B.3 — Technical drawing of the PCTFE long piece.

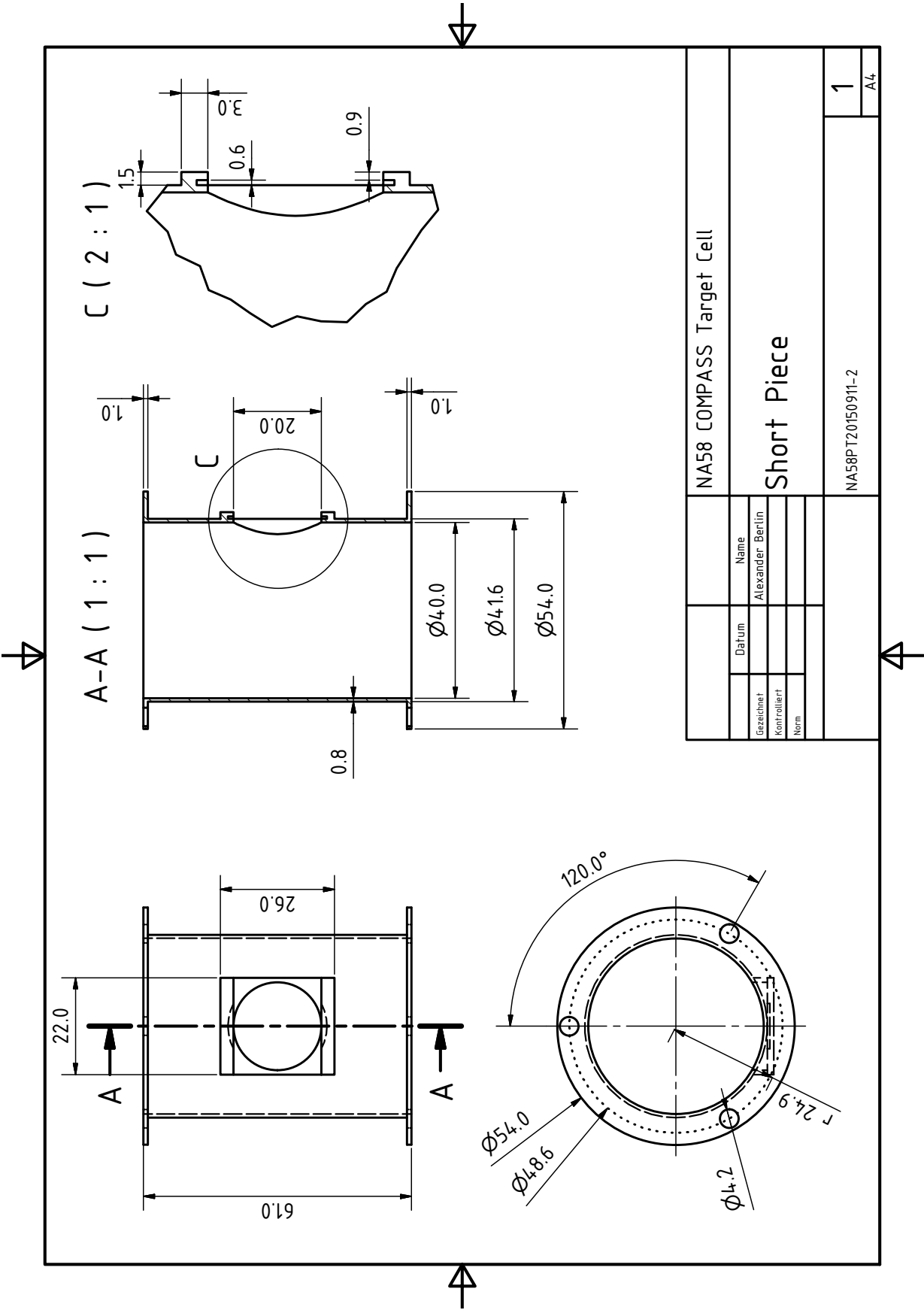


Fig. B.4 – Technical drawing of the PCTFE short piece.

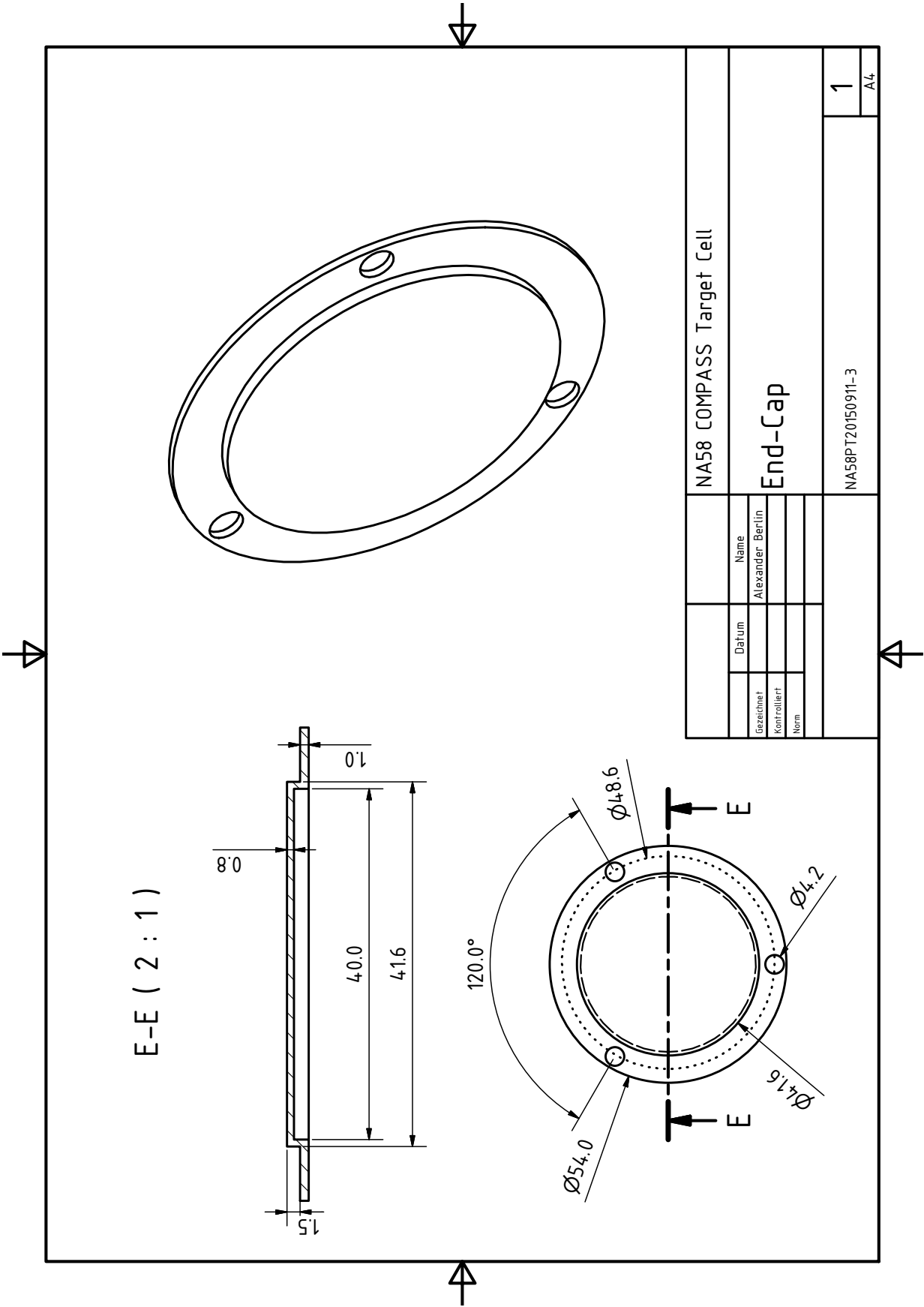


Fig. B.5 – Technical drawing of the PCTFE end-cap.

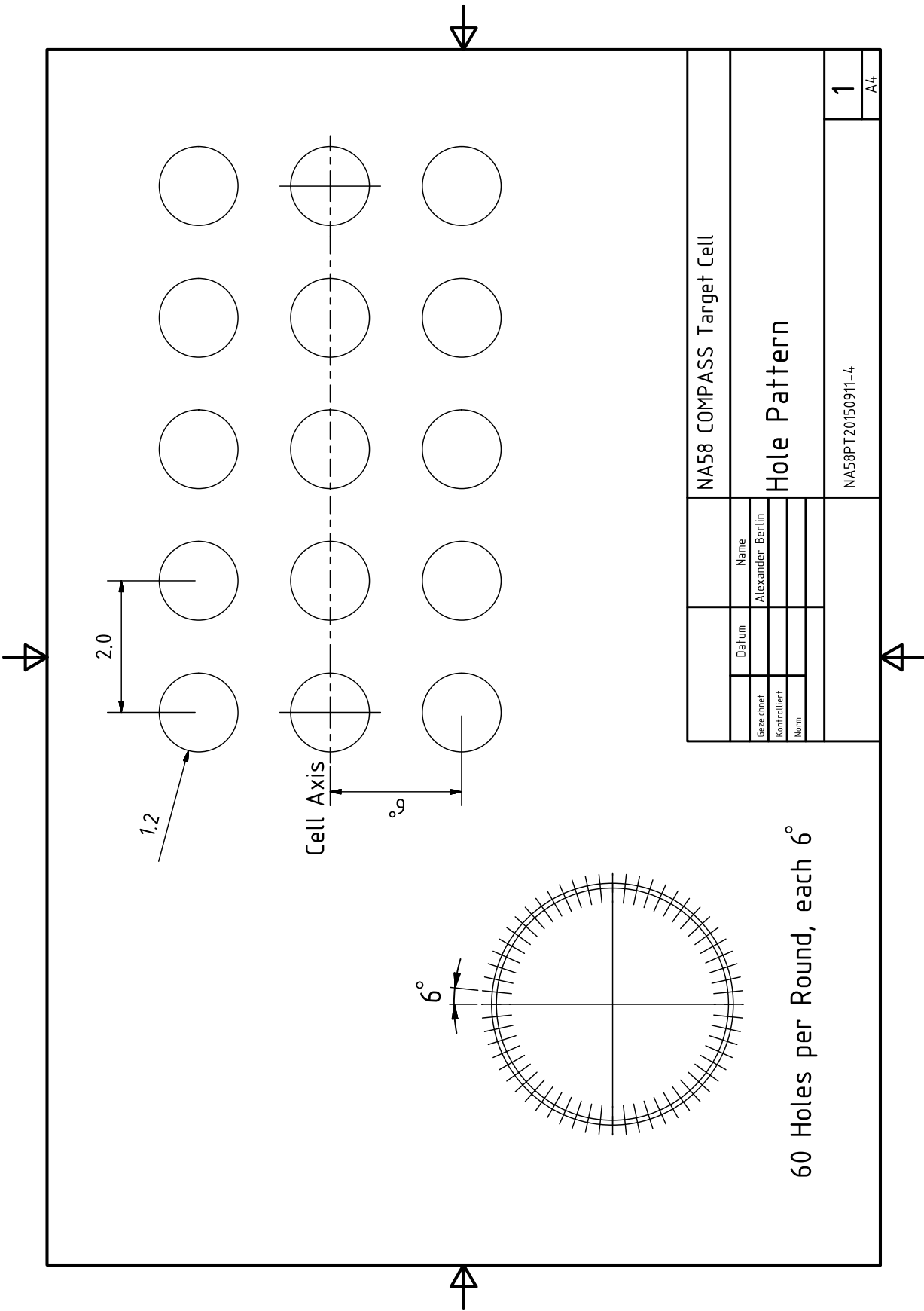
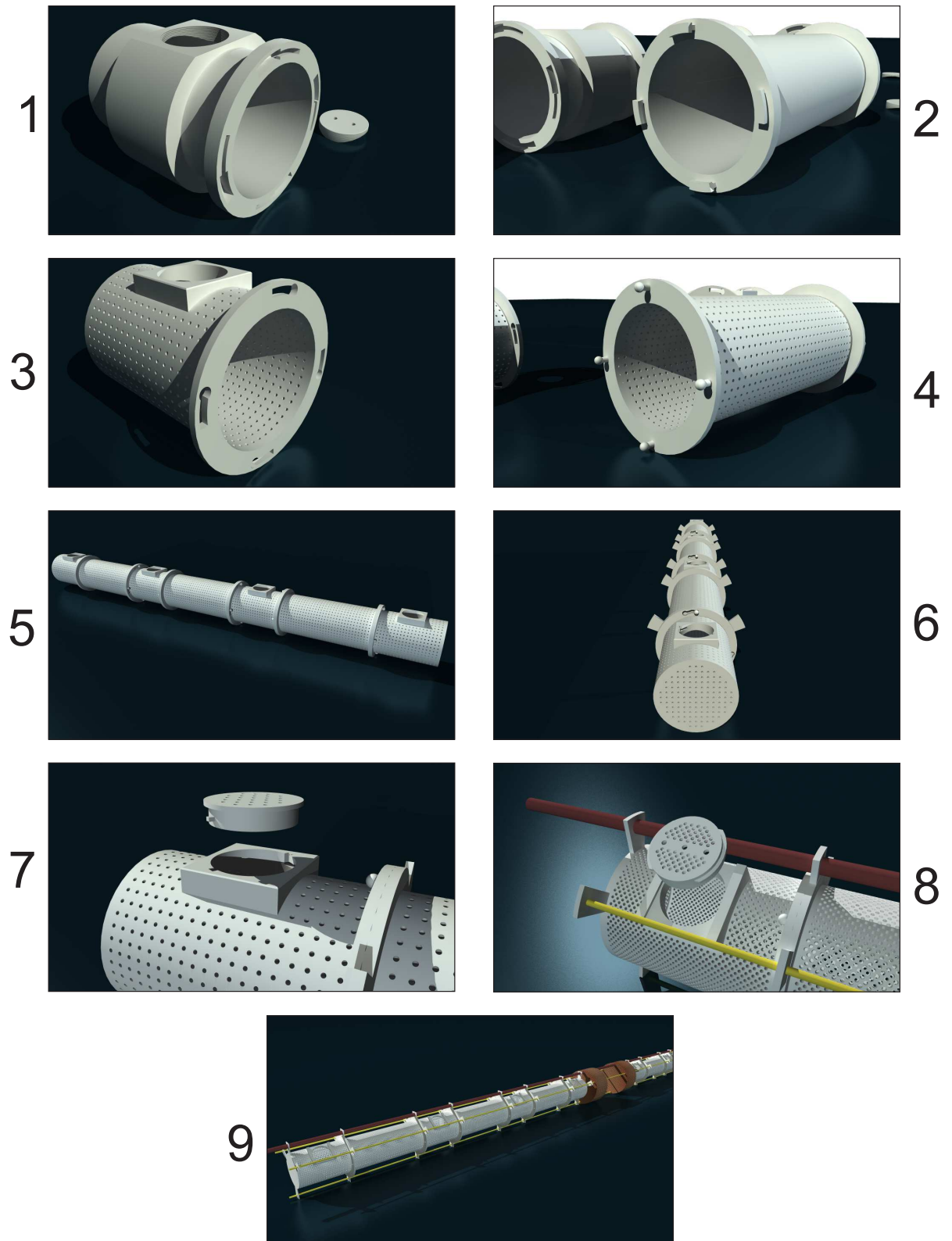


Fig. B.6 – Technical drawing of the hole pattern.

## B.4 Pictures of the Target cells



**Fig. B.7** — Design stages of the new target cell. First, a rough design of the cell was created and gradually more details were added, as well as changed.



**Fig. B.8** — Pictures of the new PCTFE cell.



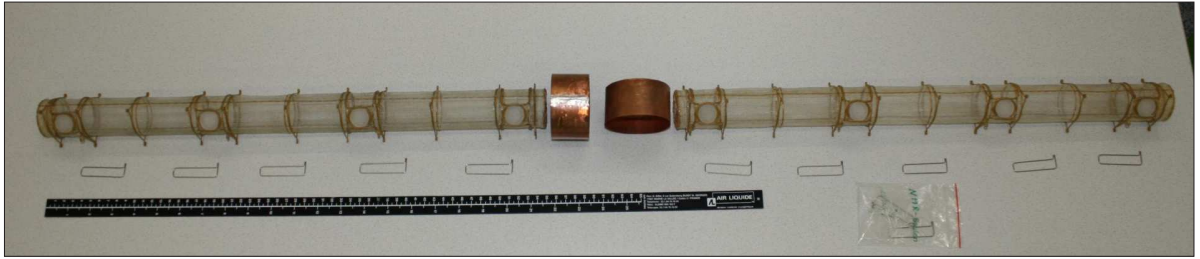


**Fig. B.9** — Pictures of the net cell, used in the test run 2014.

## B.5 Position of the Temperature Sensors and NMR Coils

The CERN is based between the Jura mountains and Mont Salève on the the Franco-Swiss border, and these prominent reference points are used to describe the position of several components of the COMPASS setup. This convention is also used for the NMR coils and the temperature sensors, within the target refrigerator.

**Tab. B.2** — Position of the temperature sensors and the NMR coils. The position are measured from the beginning of the upstream cell.

	Position (mm)	Orientation
<b>Temperature Sensors</b>		
TTH1	300	Salève side cell top part
TTH7	655	Salève side center microwave stopper
TTH5	835	Salève side cell top
TTH2	995	Jura side cell bottom part
TTH6	1300	Jura side cell top
<b>NMR Coils</b>		
1	30	center on beam axis vertical angle
2	135	cell bottom on target cell
3	280	Jura side center on target cell
4	420	top on target cell
5	525	center on beam axis vertical angle
6	785	center on beam axis vertical angle
7	980	top on target cell
8	1040	Salève side on target cell
9	1175	bottom on target cell
10	1280	center on beam axis vertical angle



## Temperature Sensors

### C.1 THMP LabView Interface

The THMP $\overline{\text{P}}$  was designed to measure the temperature of the scintillator crystals and the humidity in the end-cap calorimeter of the upcoming PANDA experiment<sup>1</sup>. These crystals have to be cooled down to  $-25^{\circ}\text{C}$ , in order to maximize their light emitting efficiency.

To make the THMP $\overline{\text{P}}$  as compatible as possible with the existing measuring equipment, the previously used CAN-BUS converter was replaced with a LabView compatible converter, because the LabView software is mainly used in our laboratory. The used converter is called Tiny-CAN II-XL from the company MHS electronics. Figures C.1ff show the LabView frontpanels of the written program for the diode sensors.



**Fig. C.1** — Trend window of the THMP $\overline{\text{P}}$  LabView program. All possible 64 sensors can be displayed, selected and/or stored. Also the graph can be switched from channels to voltages.

<sup>1</sup>PANDA stands for Anti-Proton Annihilations in Darmstadt.



**Fig. C.2** – Channel window of the THMP LabView program. This window presents an overview of all sensors, ordered for each module.

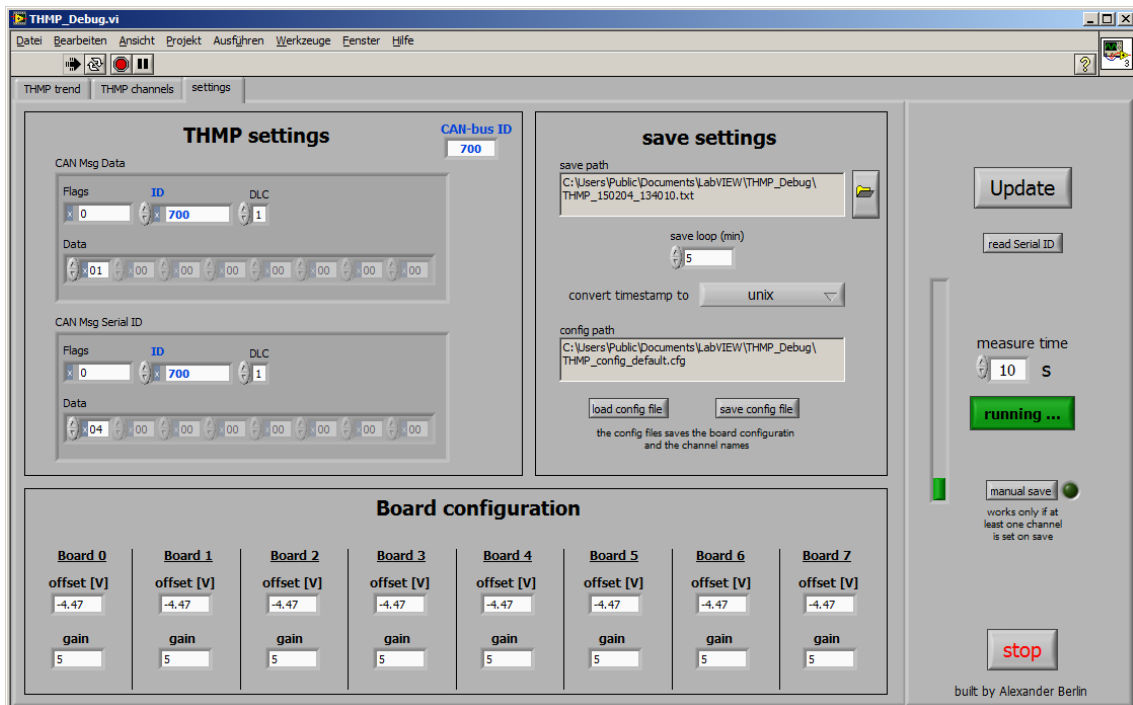


**Fig. C.3** – Settings window of the THMP LabView program, in which the CAN-BUS message can be altered as well as the save-paths for the configuration files. In addition, the offset and the gain can be set, to convert the channels online into voltage values.

## C.2 Chebychev Coefficients of the calibrated RuO resistor

The behavior of both sensor types can be described by the so-called Chebychev polynomials. For the RuO-resistor, Lake Shore recommend three separate ranges in temperature, to describe the whole curve properly. The following information are taken from the fact-sheet of the sensors.

The Chebychev equation is:

$$T(x) = \sum_{i=0}^n a_i t_i(x) \quad , \quad (C.1)$$

where  $T(x)$  is the temperature in kelvin,  $t_i$  a Chebychev polynomial and  $a_i$  the Chebychev coefficient. The parameter  $x$  is a normalized variable given by:

$$x = \frac{(Z - ZL) - (ZU - Z)}{(ZU - ZL)} \quad , \quad (C.2)$$

where  $Z$  is  $\log(\text{base}10)$  of the resistance and  $ZL$  and  $ZU$  designate the log of the lower and upper limit of the resistance over the fit range. The polynomials are given by:

$$t_i = \cos[i \cdot \arccos(x)] \quad (C.3)$$

Each fit range has its own set of Chebychev coefficients.

**Tab. C.1** — Chebychev fit coefficients of the calibrated RuO-resistor, bought from Lake Shore Cryotronics.

Fit Range: 0.050 K to 0.854 K	Fit Range: 0.855 K to 6.21 K	Fit Range: 6.21 K to 40 K
Order = 11	Order = 10	Order = 10
ZL = 3.36857136154	ZL = 3.08075347508	ZL = 3.01918082553
ZU = 4.91683280389	ZU = 3.47809298643	ZU = 3.1197498246
A(0) = 0.299654	A(0) = 2.736504	A(0) = 15.680710
A(1) = -0.394971	A(1) = -2.992778	A(1) = -15.708693
A(2) = 0.200553	A(2) = 1.347544	A(2) = 7.316767
A(3) = -0.089961	A(3) = -0.579476	A(3) = -3.428210
A(4) = 0.037813	A(4) = 0.245341	A(4) = 1.580979
A(5) = -0.015477	A(5) = -0.104455	A(5) = -0.737149
A(6) = 0.006409	A(6) = 0.044544	A(6) = 0.346324
A(7) = -0.002373	A(7) = -0.018427	A(7) = -0.147047
A(8) = 0.001118	A(8) = 0.008455	A(8) = 0.088041
A(9) = -0.000530	A(9) = -0.002829	A(9) = -0.019114
A(10) = -0.000069	A(10) = 0.001926	A(10) = 0.029287
A(11) = 0.000043		



# Bibliography

- [1] Rutherford, E., *Phil. Mag.*, **21**(125), (1911), pp. 669–688
- [2] Riordan, M., *The Discovery of Quarks*, SLAC-PUB-5724 (1992)
- [3] Abragam, A., *Principles of Nuclear Magnetism*, Oxford University Press (1961)
- [4] Abragam, A. and Goldman, M., *Rep. Prog. Phys.*, **41**(3), (1978), pp. 395–467
- [5] Hess, C., *Ein gepulstes NMR-System zur Polarisationsmessung an Festkörpertargets*, Diploma Thesis, Ruhr-Universität Bochum (2005)
- [6] Reicherz, G., *Kontroll- und NMR-System eines polarisierten Festkörpertargets*, Ph.D. thesis, Universität Bonn (1994)
- [7] Herick, J., *Ein neues cw-NMR Modul und trityl-dotierte D-Butanoltarget für Streuexperimente*, Ph.D. thesis, Ruhr-Universität Bochum, (to be published) (2015)
- [8] Vondracek, H., *Entwicklung einer HF-Messschaltung zur Polarisationsdetektion*, Master Thesis, Ruhr-Universität Bochum (2013)
- [9] Goudsmit, S. and Uhlenbeck, G.E., *Nature*, **117**, (1926), pp. 264–265
- [10] Lide, D.R. (ed.), *CRC Handbook of Chemistry and Physics*, CRC Press., pp. 9–91 (1998)
- [11] Overhauser, A.W., *Phys. Rev.*, **92**(2), (1953), pp. 411–415
- [12] Carver, T.R. and Slichter, C.P., *Phys. Rev.*, **92**, (1953), pp. 212–213
- [13] Goertz, S., *Spintemperatur und magnetische Resonanz verünnter elektronischer Systeme*, Ph.D. thesis, Ruhr-Universität Bochum, Habilitation (2002)
- [14] Hess, C., *Messung elektronischer Relaxationszeiten in dynamisch polarisierten Festkörpertargets mittels gepulster NMR*, Ph.D. thesis, Ruhr-Universität Bochum (2009)
- [15] Harmsen, J., *Chemisch dotiertes und elektronenbestrahltes 1-Butanol-d10 als polarisiertes Target für teilchenphysikalische Experimente*, Ph.D. thesis, Ruhr-Universität Bochum (2002)
- [16] Redfield, A.G., *IBM J. Res. Develop.*, **1**(1), (1957), pp. 19–31
- [17] Heckmann, J., *Elektronenspinresonanz polarisierbarer Festkörper-Targetmaterialien bei 2,5 T*, Ph.D. thesis, Ruhr-Universität Bochum (2004)
- [18] Bloembergen, N., *Physica*, **15**(3–4), (1949), pp. 386–426
- [19] Ramanathan, C., *Appl. Magn. Reson.*, **34**(3), (2008), pp. 409–421
- [20] Berlin, A., *Spindiffusionsmessungen in polarisierten Festkörpermaterialien*, Diploma Thesis, Ruhr-Universität Bochum (2010)
- [21] Buschert, D., *X-Band-ESR-Spektroskopie polarisierbarer Targetmaterialien bei tiefen Temperaturen*, Diploma Thesis, Ruhr-Universität Bochum (2005)
- [22] Apodaca, L., *Mineral Commodity Summaries 2015*, U.S. Geological Survey, URL <http://minerals.usgs.gov/minerals/pubs/mcs/> (2015)
- [23] Holleman, A., Wiberg, E. and Wiberg, N., *Lehrbuch der anorganischen Chemie*, de Gruyter, 102. ed. (2007)
- [24] Glasser, L., *J. Chem. Educ.*, **86**(12), (2009), p. 1457
- [25] Fortes, A.D., Brodholt, J., Wood, I. et al., *J. Chem. Phys.*, **118**(13), (2003), pp. 5987–5994
- [26] Haar, L. and Gallagher, J., *J. Phys. Chem. Ref. Data*, **7**(3), (1978), pp. 635–792



- [27] Gauthier, M., Pruzan, P., Chervin, J. et al., *Phys. Rev. B*, **37**(4), (1988), pp. 2102–2115
- [28] Olovsson, I. and Templeton, D., *Acta Cryst.*, **12**, (1959), pp. 832–836
- [29] Havenith, W., *NH<sub>3</sub> und ND<sub>3</sub> als Targetmaterial für Polarisationsexperimente in der Hochenergiephysik*, Staatsexsamsarbeit, Universität Bonn (1984)
- [30] Crabb, D. and D.B., D., *Nucl. Instr. and Meth. A*, **356**, (1995), pp. 9–19
- [31] Borghini, M., Choice of Substances for Polarized Proton Targets, CERN Nucl. Phys. Div., 66-3 (1966)
- [32] Crabb, D. and Meyer, W., *Annu. Rev. Nucl. Part. Sci.*, **47**, (1997), pp. 67–109
- [33] Cameron, P., Crabb, D., Lin, A. et al., *Proc. 4th Int. Workshop Pol. Targ. Mat. and Tech.*, pp. 143–148 (1984)
- [34] Adeva, B., Arik, E., Arvidson, A. et al., *Nucl. Instr. and Meth. Phys. Res. A*, **419**(1), (1998), pp. 60–82
- [35] Heyes, W., Court, G., Meyer, W. et al., *Proc. 4th Int. Workshop Pol. Targ. Mat. and Tech.*, pp. 53–59 (1984)
- [36] Dostert, R., Havenith, W., Kaul, O. et al., *Proc. 4th Int. Workshop Pol. Targ. Mat. and Tech.*, pp. 33–52 (1984)
- [37] Scheffler, K., *Nucl. Instr. and Meth.*, **82**, (1970), pp. 205–207
- [38] Niinikoski, T. and Rieubland, J., *Phys. Lett.*, **72A**(2), (1979), pp. 141–144
- [39] Meyer, W., *Nucl. Instr. and Meth. Phys. Res. A*, **526**, (2004), pp. 12–21
- [40] Cameron, P.R., Crabb, D.G., DeMuth, G.E. et al., *Phys. Rev. D*, **32**, (1985), pp. 3070–3072
- [41] Meyer, W., Althoff, K., Havenith, W. et al., *Nucl. Instr. and Meth.*, **227**, (1984), pp. 35–44
- [42] Kunkel, S., *NH<sub>3</sub>-Materialproduktion für das polarisierte COMPASS-Target am CERN*, Master Thesis, Ruhr-Universität Bochum (2012)
- [43] Runkel, S., *Herstellung und Untersuchung von Ammoniakkristallen als polarisiertes Target für das COMPASS Experiment*, Diploma Thesis, Universität Bonn (2011)
- [44] Koivuniemi, J., Doshita, N., Gautheron, F. et al., *J. Phys.: Conf. Ser.*, **150**, 012023
- [45] Gregory, C. and Nuttall, C., *Explosion Risks in Cryogenic Liquids Exposed to Ionising Radiation*, Tech. Rep. CERN AT/95-06, COMPASS collaboration, CERN (1995)
- [46] Kittel, C., *Einführung in die Festkörperphysik*, Oldenbourg Verlag, 15. ed. (2013)
- [47] Meyer, W., K.H., A., Havenith, W. et al., *Nucl. Instr. and Meth.*, **215**, (1983), pp. 65–69
- [48] Althoff, K., Burkert, V., Hartfiel, U. et al., *Proc. 4th Int. Workshop Pol. Targ. Mat. and Tech.*, pp. 23–32 (1984)
- [49] Website of the COMPASS Collaboration, URL <http://wwwcompass.cern.ch>
- [50] COMPASS Collaboration, *COMPASS-II proposal*, CERNSPSC- 2010-014 SPSC-P-340 (May 2010)
- [51] COMPASS Collaboration, *COMPASS proposal*, CERN/SPSLC 96-14 SPSC/P 297 (March 1996)
- [52] Mallot, G.K., *Spin physics at COMPASS: present and future*, Tech. rep., COMPASS collaboration, CERN, URL <https://cds.cern.ch/record/1494155> (2011)
- [53] Ashman, J., Badelek, B., Baum, G. et al., *Phys. Let. B*, **206**(2), (1988), pp. 364–370
- [54] Franco, C. et al., *Overview if the COMPASS results on the nucleon spin*, 37th International Conference on High Energy Physics, URL <http://wwwcompass.cern.ch/compass/publications/> (2014)
- [55] Rondon, O., *Phys. Rev. C*, **60**, (1999), pp. 035201 1–6



- [56] Ball, J., Baum, G., Doshita, N. et al., *Czech. J. Phys. Suppl. F*, **56**, (2006), pp. 295–305, URL <http://cds.cern.ch/record/1497225>
- [57] Doshita, N., *Polarized Target for Drell-Yan at COMPASS II*, Talk at: EU-SpinMap Workshop on Polarized Targets, Dubrovnik, URL [http://wwwa2.kph.uni-mainz.de/download/data\\_old\\_web/intern/cb16meeting/03\\_Doshita.pdf](http://wwwa2.kph.uni-mainz.de/download/data_old_web/intern/cb16meeting/03_Doshita.pdf) (2010)
- [58] Pobell, F., *Matter and Methods at Low Temperatures*, Springer-Verlag Berlin (2007)
- [59] COMPASS Polarized Target, *Electronic Logbook*, URL [http://wwwcompass.cern.ch/elog/target\\_polar/](http://wwwcompass.cern.ch/elog/target_polar/)
- [60] Sandacz, A., *Program of COMPASS-II at CERN*, Talk at: QCD Evolution Workshop, Santa Fe, New Mexico, URL <http://wwwcompass.cern.ch/compass/publications/talks/> (2014)
- [61] Martin, A., *TMDs at COMPASS*, Talk at: Workshop on Transverse Momentum Distributions, Trento, Italy, URL <http://wwwcompass.cern.ch/compass/publications/talks/> (2010)
- [62] Alexeev, M., *Nucl. Phys. B - Proc. Suppl.*, **245**, (2013), pp. 263–266
- [63] Doshita, N., Ball, J., Baum, G. et al., *Nucl. Instr. and Meth. Phys. Res. A*, **526**, (2004), pp. 138–143
- [64] Maggiora, A., *Final Hadron Absorber Simulation Status*, Talk at: Drell-Yan Hardware meeting, CERN, URL [http://wwwcompass.cern.ch/twiki/pub/Drell\\_Yan/SubgroupmeetingHDW/Angelo\\_DYmeet-5sept2012.pdf](http://wwwcompass.cern.ch/twiki/pub/Drell_Yan/SubgroupmeetingHDW/Angelo_DYmeet-5sept2012.pdf) (2012)
- [65] Maggiora, A., Gianmaria, M., Longo, R. et al., *FLUKA simulation of the irradiation dose on the Compass PT material holder*, Tech. Rep. COMPASS note 2013-10, COMPASS collaboration, CERN (2013)
- [66] Forkel-Wirth, D., Roesler, S., Silari, M. et al., *Radiation protection at CERN*, CERN Document Server, URL <http://cds.cern.ch/record/1533023> (2013)
- [67] Matoušek, J., *Studies of Drell-Yan process at Compass experiment*, Master Thesis, Charles University in Prague (2013)
- [68] Bordignon, E., *Nitroxide Spectrum Analysis Tutorial*, Talk at: 5th EF-EPR Summer School on Advanced EPR Spectroscopy, URL [http://www.epr.ethz.ch/news/Bordignon\\_tutorial\\_Nitroxide\\_spectrum\\_analysis.pdf](http://www.epr.ethz.ch/news/Bordignon_tutorial_Nitroxide_spectrum_analysis.pdf) (2011)
- [69] Riechert, H., *Ammoniak – Ein Targetmaterial für polarisierte Nukleonentargets an hochenergetischen  $\gamma$ - und Elektronenstrahlen*, Diploma Thesis, Universität Bonn (1982)
- [70] Pešek, M., *Low temperature polarized target for spin structure studies of nucleons at COMPASS*, Master Thesis, Charles University in Prague (2014)
- [71] Biederbick, K., *Kunststoffe kurz und bündig*, Vogel Verlag, 3. ed. (1974)
- [72] Solvay Advanced Polymers GmbH, *Torlon polyamide-imide technisches Handbuch*, t-50246de (2006)
- [73] Daikin Chemical Europe GmbH, *Product Information Brochure: Neoflon (PCTFE)*, URL <http://www.daikinchem.de/PCTFE.html> (2003)
- [74] Ashman, J., Badelek, B., Baum, G. et al., *Nucl. Phys. B*, **328**(1), (1989), pp. 1–35
- [75] Adams, D., Adeva, B., Arik, E. et al., *Nucl. Instr. and Meth. Phys. Res. A*, **437**(1), (1999), pp. 23–67
- [76] Matoušek, J. and Pešek, M., *COMPASS Polarized Target for Drell-Yan Experiment*, XVth Int Workshop Pol. Sour., Targ. and Pol., URL <http://wwwcompass.cern.ch/compass/publications> (2013)
- [77] Feldbauer, F., *Analyse des Zerfalls  $\chi_{cJ} \rightarrow K^+ K_s^0 \pi^- \pi^0$  bei BES-III und Entwicklung der slow control für das PANDA-Experiment*, Ph.D. thesis, Ruhr-Universität Bochum (2012)
- [78] COMPASS Polarized Target Wiki, *Dilution cryostat temperature*, URL <http://wwwcompass.cern.ch/twiki/bin/view/PolarizedTarget/PolTargTemp>



# List of Figures

1.1	Overview of quarks and leptons . . . . .	2
1.2	Artistic illustration of the nuclear spin-decomposition . . . . .	3
2.1	Classical orbital angular momentum of an electron . . . . .	5
2.2	Illustration of the quantum mechanical orbital angular momentum with $L=2$ . . .	6
2.3	Term diagram of a spin-1/2 and spin-1 nucleus . . . . .	7
2.4	Illustration of the Larmor-precession . . . . .	8
2.5	TE-polarization of electrons, protons and deuterons . . . . .	10
2.6	Simplified scheme of the solid-state DNP process . . . . .	12
2.7	Demonstration of the difference between SSE and DSSE . . . . .	13
2.8	Frequency curve of $^7\text{LiH}$ at 2.5 T . . . . .	14
2.9	Occupation-number density of electrons in the spin-temperature concept . . . . .	15
2.10	Artistic illustration of the polarization process through spin-diffusion . . . . .	16
2.11	Net magnetization of a spin system . . . . .	18
2.12	Decomposition of the oscillating field in two contrarily rotating magnetic fields . .	19
2.13	Illustration of the $T_1$ and $T_2$ relaxation time . . . . .	20
2.14	Inclination of the effective magnetic field in the rotating frame . . . . .	20
2.15	Schematic view of the cwNMR circuit . . . . .	22
2.16	Simplified scheme of an EPR spectrometer . . . . .	24
3.1	Artistic view of an ammonia molecule . . . . .	27
3.2	Phase diagram of ammonia and crystalline structure of the solid I phase . . . . .	28
3.3	Study of EST in ammonia $^{14}\text{NH}_3$ . . . . .	31
3.4	Extended X-band EPR-spectrum of irradiated Ammonia . . . . .	33
3.5	Illustration of the solidification device for ammonia . . . . .	34
3.6	Illustration of the irradiation refrigerator . . . . .	36
3.7	Close-up view of the sample container in the irradiation refrigerator . . . . .	37
3.8	The purple color of fresh irradiated ammonia . . . . .	38
3.9	Radiation damage of pre-irradiated $\text{NH}_3$ and chemical doped butanol . . . . .	41
3.10	Evolution of the maximum polarization of pre-irradiated and untreated ammonia .	42
4.1	Side view of the COMPASS refrigerator . . . . .	46
4.2	Graph of the reaction processes in SIDIS and Drell-Yan . . . . .	48
4.3	Illustrated overview of the different parton distribution functions . . . . .	49
4.4	Scheme of the hadron absorber for the DY-measurement at COMPASS II . . . . .	50
4.5	Cooling power and mixing chamber temperature of the COMPASS refrigerator . .	50
4.6	Simulation of the ambient radiation dose of the COMPASS experimental hall . . .	52
4.7	Simulation of the predicted radiation exposure for the DY-measurement . . . . .	53
5.1	Comparison of different X-band EPR-spectra . . . . .	56
5.2	Color decay of irradiated ammonia . . . . .	57
5.3	Changes of the paramagnetic properties of irradiated ammonia . . . . .	58
5.4	Absolute radical concentration versus time after irradiation . . . . .	59
5.5	Frequency curve of irradiated ammonia at 2.5 T and 1056 mK . . . . .	60
5.6	A typical cycle of a relaxation measurement . . . . .	61
5.7	Build-up and relaxation of the 'old' and 'new' ammonia . . . . .	61
5.8	Comparison between the relaxation fit functions . . . . .	62
5.9	Artistic illustration of the polarization behavior in irradiated ammonia . . . . .	63
5.10	Comparison of the EPR-spectra between 1995 and 2011 . . . . .	63
5.11	Long-term behavior of the build-up time of irradiated ammonia . . . . .	64
5.12	Long-term relaxation measurement of ammonia . . . . .	65

5.13	Trend of the mixing parameter $\eta$ . . . . .	66
5.14	Build-up curves of the $\text{NH}_3$ polarization at COMPASS for 2007 and 2010 . . . . .	67
5.15	Evolution of the temperature in the mixing chamber during the target loading . . . . .	69
5.16	Build-up curve of the $\text{NH}_3$ polarization at COMPASS for 2011 . . . . .	69
5.17	Frequency shift of the optimal microwave frequency at COMPASS . . . . .	70
6.1	Visual result of the Bonn radiation simulation . . . . .	74
6.2	Picture of the radiation exposed materials and sensors at 20,000 Gy . . . . .	75
6.3	Skeletal chemical structure of PCTFE and Torlon . . . . .	76
6.4	TE-signals of hydrogen at COMPASS in 2011 . . . . .	76
6.5	Measurement of the hydrogen content of PCTFE and Torlon . . . . .	77
6.6	Overview of the different parts of the PCTFE cell body . . . . .	79
6.7	History of the target cells at COMPASS and its predecessors . . . . .	80
6.8	Locking mechanism of the filling-holes . . . . .	81
6.9	Pictures of a microwave stopper . . . . .	82
6.10	Configuration of the NMR coils for the new target cell . . . . .	83
6.11	Pictures of the fully equipped PCTFE cells . . . . .	84
7.1	Pictures of the temperature sensor setup . . . . .	86
7.2	Function of the ADC-offset in the THMP . . . . .	87
7.3	Draft of the irradiation board . . . . .	88
7.4	Photography of the irradiation board . . . . .	88
7.5	Overview of the second irradiation run in Jülich . . . . .	89
7.6	Matching procedure for the temperature sensors . . . . .	90
7.7	Cutting method to minimize wrong temperature matching . . . . .	90
7.8	Behavior of the RuO-resistors, up to a radiation dose of 20,000 Gy . . . . .	91
7.9	Estimation of the statistical error of the RuO-resistor . . . . .	92
7.10	Behavior of the silicon diodes, up to a radiation dose of 20,000 Gy . . . . .	93
7.11	A close-up of the temperature dependance of D3 below 1.4 K . . . . .	94
A.1	Frontpanel of the relaxation fitting-program . . . . .	103
A.2	Overview of the average polarization at COMPASS for 2007 . . . . .	104
A.3	Overview of the average polarization at COMPASS for 2010 . . . . .	105
A.4	Overview of the average polarization at COMPASS for 2011 . . . . .	105
B.1	Detailed results of the Bonn radiation simulation . . . . .	108
B.2	Technical drawing of the net cell 2014 . . . . .	110
B.3	Technical drawing of the PCTFE long piece . . . . .	111
B.4	Technical drawing of the PCTFE short piece . . . . .	112
B.5	Technical drawing of the PCTFE end-cap . . . . .	113
B.6	Technical drawing of the hole pattern . . . . .	114
B.7	Design stages of the new target cell . . . . .	115
B.8	Pictures of the PCTFE cell . . . . .	116
B.9	Pictures of the net cell of 2014 . . . . .	117
C.1	Trend window of the THMP LabView program . . . . .	119
C.2	Channel window of the THMP LabView program . . . . .	120
C.3	Settings window of the THMP LabView program . . . . .	120



# Curriculum Vitae

## Personal Information

Name: Alexander Berlin  
Date of Birth: May 4, 1984  
Place of Birth: Lünen, Germany  
Nationality: German  
eMail: alexander.berlin@ruhr-uni-bochum.de

## Ph. D. Studies

- 05/2010 **Beginning of Ph. D. Studies** at the  
Institute of Experimental Physics I / Physics of Hadrons and Nuclei  
Faculty of Physics and Astronomy  
Ruhr-University of Bochum, Germany  
Under Supervision of Prof. Dr. Werner Meyer

## Higher Education

- 03/2010 **Graduation Diplom degree**
- 04/2009 – 03/2010 Diplom degree, Physics  
Title of Thesis: "*Spindiffusionsmessungen in polarisierten Festkörpermateriellen*"  
Institute of Experimental Physics I / Physics of Hadrons and Nuclei  
Faculty of Physics and Astronomy  
Ruhr-University of Bochum, Germany
- 10/2004 – 04/2010 Studies of Physics at the Ruhr-University of Bochum

## Education

- 06/2003 **Higher Education Entrance Qualification**
- 08/1994 – 06/2003 Johann-Conrad Schlaun Comprehensive School, Nordkirchen, Germany
- 08/1990 – 06/1994 Lutherschule Primary School, Selm, Germany

## Professional Occupation

- 05/2010 – 07/2015 **Research Assistant** at the  
Institute of Experimental Physics I / Physics of Hadrons and Nuclei  
Faculty of Physics and Astronomy  
Ruhr-University of Bochum, Germany
- 09/2008 – 04/2010 **Student Assistant** at the  
Institute of Experimental Physics I / Physics of Hadrons and Nuclei  
Faculty of Physics and Astronomy  
Ruhr-University of Bochum, Germany

Bochum, September 20, 2015

Alexander Berlin



